STRUCTURE, COMPOSITION AND PERFORMANCE OF SURFACE FILMS ON AZ ALLOYS AS A FUNCTION OF pH AND ALLOYED ALUMINUM CONCENTRATION

By

RYAN PHILLIPS, B.Eng.Mgt.

A Thesis

Submitted to the School of Graduate Studies

In Partial Fulfillment of the Requirements

For the Degree

Master of Applied Science

McMaster University

McMaster University MASTER OF APPLIED SCIENCE (2011)

Hamilton Ontario, (Materials Engineering)

TITLE: Structure, Composition and Performance of Surface Films on AZ Alloys as a Function of pH and Alloyed Aluminum Concentration

AUTHOR: Ryan Phillips B.Eng.Mgt (McMaster University)

SUPERVISOR: Professor Joseph Kish

NUMBER OF PAGES: xii, 114

Abstract

This thesis presents an investigation into the structure, composition and performance of naturally formed surface films on AZ alloys as a function of pH and alloyed Al concentration. STEM verified the film structure was bi-layer, consisting of an inner barrier layer, which was visibly deteriorated, and an outer porous layer. EDS SmartMaps™ coupled with the Inca™ software package determined the inner barrier layer was predominantly composed of MgO, whereas the outer layer was primarily $Mg(OH)_2$. However, both layers appeared to posses mixed oxide/hydroxide components according to ToF-SIMS analysis.

Environmental pH had the largest effect on the structure and composition of the surface film. The near-neutral sample showed significant breakdown within the inner layer, which was attributed to natural hydration of MgO to $Mg(OH)_2$. This favourable hydration reaction is slower in alkaline environments and as such, the stability of the inner barrier layers of the pH 14 samples were noticeably improved. The effect of alloyed Al concentration was less significant however; increased enrichment of Al into the surface film structure appeared to cause a reduction in the thickness of the corrosion film itself.

Drastic differences in corrosion performance were observed between the near-neutral and alkaline environments. Significantly better corrosion resistance to anodic dissolution was present in the alkaline environment coupled with a noticeably lower corrosion rate. The absence of breakdown potentials along with the presence of mass transport controlled anodic kinetics signified that the improved stability of the inner barrier layer was responsible for improved corrosion performance. In contrast, severe pitting and a narrow range of anodic stability were present for the near-neutral samples where the inner barrier layer was significantly compromised. This deterioration was deemed responsible for accelerated cathodic kinetics as well as minimal impedance to aggressive Cl^- ions from initiating wide scale electrochemical breakdown of the surface film.

Acknowledgements

I would like to dedicate this thesis to my new wife Mariana who continually supported me throughout the writing process. During writing, she calmed me down when I was aggravated and pushed me on when I was unmotivated. She is my whole world and completing this work allows me to concentrate on helping her build our new lives together.

I would like to thank my supervisor, Joey Kish, for taking me under his wing for the past two years and providing me with the flexibility to pursue my own research goals. Although Joey carried many years of corrosion engineering experience, his knowledge of magnesium corrosion at the start of this project was limited, and as a result, many of the research highlights and lowlights we shared together. However, in the times when I was struggling mightily, I always knew I could count on him to steer me in the right direction.

I would also like to extend my gratitude to those that assisted me with difficult experiments throughout my thesis. Specifically, CCEM employees Julia Huang and Carmen Andrei as well as Rana Sodhi of Surface Interface Ontario assisted me greatly with exceedingly difficult measurements and analysis. In addition, Doug Culley generously offered his support whenever I required assistance in the MSE Labs.

The Walter W. Smeltzer corrosion group also provided me with plenty of helpful insight and constructive criticism along the way. Many fruitful discussions, specifically with Mehdi Taheri, helped shaped this project into what it is today.

I would like to thank NSERC and OGS for their financial support as well as GMC, CANMET-MTL, NRC and UBC for their generosity in providing sample materials.

Finally, I would like to thank my family for their ongoing support throughout my university education. My parents Jo and Dave as well as my brother Matt, who has been my climbing partner and best friend throughout university, were always available to chat with when the times were tough and I needed them most.

Table of Contents

List of Figures

List of Tables

1 Introduction

1.1 Overview of Problem

Magnesium (Mg) is the lightest structural engineering metal with a density of just 1.74 g/cm^3. Furthermore, Mg and its alloys possess high specific strength and excellent castability. Consequently, Mg alloys can provide significant weight savings when replacing heavier steel or aluminum components in transportation applications. 'Magnesium Vision 2020' demonstrates the weight savings Mg components can produce and additionally, the reduction in greenhouse gas emissions to the environment [1].

Unfortunately, Mg also exhibits poor resistance to aqueous corrosion in mildly aggressive neutral environments. The corrosion resistance of Mg is primarily related to the amount and distribution of impurity particles, as well as the quasi-passive nature of the $MgO/Mg(OH)_2$ corrosion film [2-7]. To improve the corrosion resistance of Mg, aluminum (Al) is commonly alloyed up to 9 wt %. The most common series of Mg-Al alloy is the AZ series, primarily consisting of Mg with Al and zinc (Zn) as major alloying elements. The reason for alloying Al into Mg for corrosion resistance is related to the enrichment of the $MgO/Mg(OH)_2$ corrosion film with the highly resistant Al_2O_3 corrosion product [5]. The Al_2O_3 is stable in neutral environments and its incorporation into the AZ alloy corrosion film has been found to improve the corrosion resistance compared with pure Mg [5, 8-10]. Alloying Al into Mg also results in the precipitation of the nobler $Mg_{17}Al_{12}$ (β) phase along grain boundaries, given the alloyed Al concentration is approximately 3 wt % or higher [11]. If the distribution of the β phase is controlled, the corrosion resistance of the alloy improves by forming a corrosion barrier. This barrier

forms when grains of the matrix phase corrode and leave behind a grain boundary network of the β phase, which prevents the corrosion front from propagating into the metal [6, 10, 12-17]. However, an unfavourable, discontinuous distribution of the β phase results in micro-galvanic coupling and the corrosion resistance deteriorates [6, 10, 12-17].

Sadly, even studies that have shown improvements to the corrosion resistance of Mg through Al alloying, conceive that the corrosion resistance of AZ alloys in near-neutral, moderately aggressive salt environments is still too low for the automotive industry [14, 18-21]. These environments are abundant in automotive applications, and as a result, Mg alloys are restricted to interior components [2, 4-7, 9, 10, 12-16, 18-46]. Further research aimed at improving the corrosion resistance of Mg alloys needs to be conducted before they find widespread use in exterior automotive applications

Anodizing of Mg alloys is a common surface treatment used as a corrosion control strategy. Anodization of Mg alloys consists of two separate stages: primary passivation (< 3V) and secondary passivation (> 30V) [24]. Secondary passivation is typically exploited to produce a protective, thick anodic MgO film on the surface [24]. Primary passivation has rarely been investigated even though it has been shown numerous times the current density is quite low in this region. Primary passivation is more indicative of natural self-passivation of Mg alloys due to the smaller anodic overpotential applied to form the surface film.

The self-passivation of AZ alloys in both neutral and alkaline environments will be investigated throughout this study. It has been shown that the current density of AZ31

at E_{corr} in alkaline environments has been estimated to be approximately $1x10^{-8}$ A/cm^2; three orders of magnitude smaller than the current density reported in near-neutral environments [31, 43]. Both films are similar in structure and composition, however the fundamental basis for the marked difference in corrosion behaviour remains unclear [31, 33, 39, 45]. It is also uncertain if alloyed Al concentration significantly affects the corrosion behaviour between the two environments. This study will attempt to clarify the effect of pH on the structure and composition of the surface film formed on AZ alloys, as well as the role of alloyed Al concentration on the overall corrosion behaviour.

2 Literature Review

2.1 Ternary Mg-Al-Zn (AZ) Alloys

AZ alloys are the most widely used Mg alloys, containing 2-10 wt % Al along with minor alloying additions of Zn and Mn. These alloys are commonly found in automotive and aerospace applications due to their affordability and capacity to provide significant weight savings over steel and aluminum [7, 11, 16, 20, 27, 46]. In addition, AZ alloys possess high specific strength, excellent castability, high damping capacity and good electromagnetic interference resistance [7, 25, 33, 34]. These properties make AZ alloys specifically attractive to the transportation industry as structural components. Unfortunately, their aqueous corrosion resistance in mildly aggressive environments is quite poor. The electronegativity of the alloy, microstructure, as well as structure and composition of the passive film govern the corrosion resistance of AZ alloys. Due to this poor corrosion resistance, AZ alloys are currently restricted to interior components unexposed to the natural environment [2, 4-7, 9, 10, 12-16, 18-46].

The major alloying element in AZ alloys is Al. Alloying Al into Mg produces an alloy with enhanced castability properties, as well as improved fatigue, tensile and compressive strength [30]. Strength and stiffness enhancements are sizably increased when the Al concentration is high enough to precipitate the hard β phase into the microstructure [30]. However, despite the strength improvements, an uncontrolled distribution of the brittle β phase can cause drastic reductions in the overall ductility of AZ alloys. Furthermore, Al has been shown to cause deterioration to the creep resistance and impact strength [47]. Perhaps the most important role of Al in AZ alloys is its ability

to improve the corrosion resistance. Since corrosion of AZ alloys is of primary importance, alloying Al is extremely important to the alloy series and the possible widespread implementation into transportation applications.

Zn and Mn are alloyed into AZ alloys for added strength and to increase the tolerance limits of Mg to impurity elements such as Fe, Ni and Cu [4, 30]. Alloying Zn over 1 wt % has been shown to increase the tendency of the AZ alloy to exhibit hot cracking during processing [30].

2.2 Microstructure of AZ Alloys

2.2.1 Wrought Microstructure (AZ31/AZ61/AZ80)

Wrought alloys generally have higher strength than cast alloys making them better candidates for structural transportation components [48]. AZ alloys typically found in the wrought condition are AZ31, AZ61 and AZ80. AZ31 is commonly fabricated in the rolled or extruded condition, whereas AZ61 and AZ80 are by in large extruded or forged, due to the high cracking susceptibility when rolling AZ alloys with high Al content [49]. Letzig et al. has shown that as Al content increases, the grain size of wrought AZ alloys decreases [50]. In addition, the grain structure appeared to become more uniform as Al content increased from 3 to 8 wt %.

AZ31 is a single-phase (α) alloy that contains various AlMn intermetallic particles [51]. AZ61 possesses a similar microstructure to AZ31, however small amounts of the β phase are commonly observed [52]. Merino et al. has analyzed the AlMn intermetallic particles in three different AZ alloys using TEM and they found all particles exhibited similarities in both structure and size [51]. AZ80 is a two-phase alloy and contains a

significant fraction of the β phase in the microstructure. In the wrought condition, the β phase precipitates along grain boundaries in a semi-continuous fashion [52]. Occasionally, the β phase also forms a lamellar network with the α phase within individual grains while generally maintaining the semi-continuous distribution along the grain boundaries [53].

2.2.2 Cast Microstructure (AZ80/AZ91D)

AZ alloys are commonly cast when alloyed Al concentration is high due to the difficulty in rolling or extrusion. High Al content lowers the ductility and inevitably increases the risk of cracking when performing rolling, extrusion or forging operations [30]. AZ80 is frequently extruded, however it is also fabricated by casting quite often. AZ91 is exclusively manufactured via casting. Die casting of AZ91D has proven to be a formidable manufacturing process capable of producing intricate components with a high degree of precision [54].

The microstructure of cast alloys is drastically different from wrought alloys. No grain structure is evident and dendrite morphologies shape the microstructure. Pardo et al. studied cast alloys of AZ80 and AZ91D and the corresponding microstructures were characterized using SEM and TEM [10]. They found that vastly different microstructures were apparent on the two alloys even though their nominal compositions were very similar. The AZ80 alloy exhibited large areas of lamellar α + β colonies surrounded by the α phase solid solution. The AZ91D alloy had a higher solidification rate, and therefore, a partially divorced α + β eutectic phase was contained within primary α phase dendrites. Lunder et al. witnessed a similar morphology of the AZ91-F alloy where a

partially divorced eutectic was surrounded by the matrix phase [13]. Due to the high solidification rates, a continuous distribution of the β phase was not observed on either alloy. Instead, large eutectic particles or lamellar colonies were present.

2.3 Corrosion Resistance of AZ Alloys

2.3.1 Effect of Alloy Chemistry

Amongst the major alloyed elements contained within AZ alloys, Al plays the most significant role in determining the overall corrosion resistance. It is well known that alloying Al improves the atmospheric corrosion resistance of AZ alloys with respect to pure Mg in humid environments [8]. In a study performed by Feliu Jr. et al., an increase in the corrosion resistance of AZ31 was witnessed compared with pure Mg when exposed to 98% RH at 50°C [6]. Stabilization of the corrosion film by Al enrichment near the alloy surface was deemed responsible for the increase in corrosion resistance of AZ31. Splinter and McIntyre showed alloyed Al enriched the surface film of Mg-Al surfaces exposed to D_2O water vapour causing a reduction in the amount of concentration defects within the initial air-formed MgO surface film [8]. This removal of concentration defects caused a reduction in the bulk thickening rate of the oxide and improved the corrosion resistance. In another study, Lindstrom et al. found that corrosion resistance of AM20, AM60 and AZ91 exposed to a 95% RH environment increased as Al concentration increased [55].

In aqueous environments, alloyed Al also typically improves the overall corrosion resistance of AZ alloys similar to humid environments. The benefits of Al alloying on the aqueous corrosion resistance of ternary MgAl alloys are observed as the Al content

increases up to 10%, and thereafter, only minor improvements are noticeable [56]. Eliezer et al. reported that corrosion resistance increased in the order AZ31 < AZ61 < AZ91 when the alloys were exposed to an aggressive 5% NaCl solution [57]. Song et al. observed significantly higher corrosion resistance as alloyed Al concentration increased from 2 wt % in AZ21 to 9 wt % in AZ91 when exposed to 1 N NaCl solutions [19]. Wang et al. found AZ91 had higher corrosion resistance with respect to AZ31 in 0.01 M NaCl solutions by examining current density magnitudes during potentiostatic polarization [44]. In addition, Pardo et al. showed the surfaces of AZ80 and AZ91 were far less corroded than the surface of AZ31 after 28-day immersion in 3.5 wt % NaCl solution [10]. The specific mechanism causing the reduction in corrosion rate due to Al alloying is still poorly understood and possible explanations will be explored in the following sections.

The second major alloying element of the AZ alloy series is Zn. The effect on the corrosion resistance of AZ alloys has been studied and generally, no effect on the corrosion behaviour has been observed [5, 58]. Beldjoudi et al. reported that alloyed Zn reduced the overpotential for cathodic hydrogen evolution on AZ alloys, while at the same time, lowered the anodic dissolution rate of Mg [58]. Consequently, no significant changes in the corrosion behaviour of AZ alloys were observed as the anodic and cathodic effects neutralized each other. Nordlien et al. observed no noticeable effects on the corrosion performance of ternary MgAl alloys through Zn alloying and came to similar conclusions [5]. It has however been shown that Zn increases the tolerance limit of Mg to Ni, which provides some forgiveness when attempting to produce high purity

Mg alloys [30]. Few studies have since been undertaken regarding the influence of Zn on the corrosion resistance and it is generally accepted that Zn is alloyed primarily for mechanical purposes.

Trace elements inherent in AZ alloys, such as Fe, Ni, Co and Cu are termed impurity elements. Hanawalt et al. showed that corrosion rates increased rapidly as these elements were alloyed into pure Mg in small concentrations (<< 0.1 wt %) as seen in Figure 2.1 [59]. Fe, Ni, Co and Cu are extremely effective at establishing local cathodes within the solid solution microstructure and producing micro-galvanic activity [4, 56]. Impurity limits were established to limit the degree of corrosion from these trace impurity particles. Concentration of impurities above the impurity limits has been observed to increase the corrosion rate on Mg alloys by as much as 100 times [3]. As a result, high purity AZ alloys have been developed to strictly adhere to these impurity limits.

A minor alloying element, utilized in AZ alloys is Mn. Mn considerably reduces the tolerance limits of both Fe and Cu [30]. This property was demonstrated by Reichek et al. who studied the effect of Fe/Mn ratio on the corrosion rate of AZ91, shown in Figure 2.2. A critical tolerance limit was obtained where a rapid increase in the corrosion rate occurred when the ratio was surpassed. Alloyed Mn ties up impurity Fe in AlMn(Fe) intermetallic particles within the solid solution phase of AZ alloys. [4]. Lunder et al. and Merino et al. have compiled an extensive list of commonly found AlMn intermetallic particles in separate works [4, 51]. These intermetallic particles are significantly nobler in galvanic potential with respect to the α matrix phase, and thus, large driving forces for microgalvanic coupling are present.

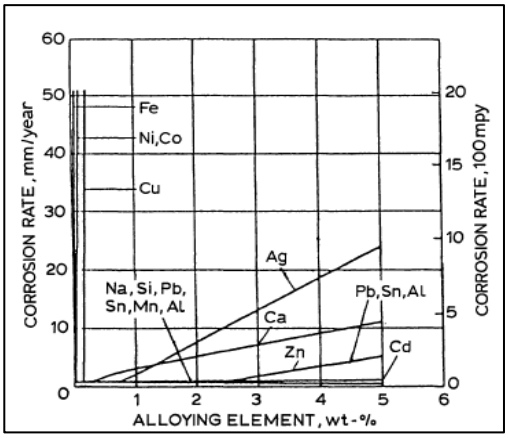

Figure 2.1: Effect of alloying elements on the corrosion rate of pure Mg. [59]

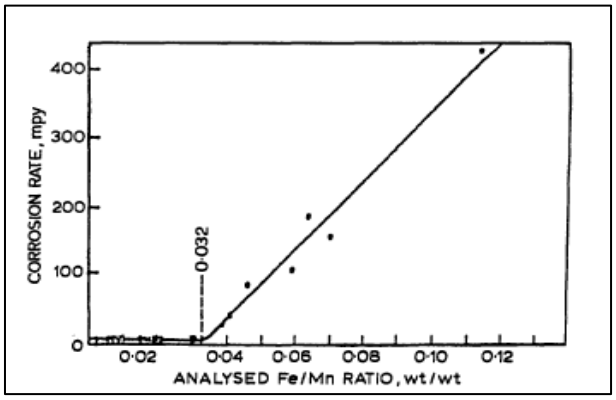

Figure 2.2: Critical Fe/Mn tolerance limit for corrosion resistance of AZ91 alloy. [60]

2.3.2 Microstructural Effects

Microstructure inherent within AZ alloys plays a large role in the overall corrosion resistance. Specifically, corrosion of AZ alloys is largely influenced by the composition of the α phase, as well as the composition and distribution of secondary phases and impurities [3]. These nobler secondary phases and impurities cause microgalvanic coupling with the more active α matrix phase [4].

All AZ alloys contain a significant amount of Mn within their chemical composition [61]. Besides the obvious strength improvements Mn adds, its primary purpose is to tie up Fe impurities into AlMn(Fe) intermetallic particles [4, 51]. These

particles are generally found within all AZ alloys, however their impact on microgalvanic activity is far greater in those alloys that do not contain the β phase. This is because without the β phase, these intermetallic particles remain as the only true cathodic sites to initiate microgalvanic activity.

Lunder et al. has compiled a list of the commonly found AlMn intermetallic particles in AZ alloys along with their corresponding galvanic potential with respect to a 4N Mg phase [4]. They reported that intermetallics, which contained Fe, produced the noblest galvanic potential, and therefore, possessed the largest driving force for initiation of microgalvanic corrosion. That being said, heavy metal impurities such as Fe and Ni possess low hydrogen overvoltages, which cause severe galvanic corrosion when present as single entities within the microstructure [46]. Therefore, a significant reduction in microgalvanic attack and corrosion rate was found when Fe concentration was maintained below the impurity limit and carefully tied up in AlMn(Fe) intermetallic particles [60]. Merino et al. identified AlMn intermetallics via TEM and mapped their corresponding surface potential using a scanning probe system, where significantly nobler potentials with respect to the α matrix were reported [51]. Intermetallic studies of this nature are common, however they only encompass the thermodynamic potential for microgalvanic corrosion. Studies regarding the kinetics of this microgalvanic reaction are much more scarce and, therefore, it is unclear whether or not the large driving force for microgalvanic corrosion implies the reaction will occur quickly or sluggishly.

Throughout corrosion research on AZ alloys, perhaps no bigger topic has been studied more thoroughly than the effect of the β phase. As such, it is no surprise that

various interpretations regarding its behaviour in the corrosion process have been reached. To date, the β phase has been generally been accepted to affect corrosion in two distinctly separate ways.

If the distribution of the β phase is controlled and essentially continuous, a corrosion barrier forms and propagation of the corrosion front is impeded [6, 10, 12-17]. Zhao et al. studied the effect of the β phase morphology on the corrosion resistance of AZ91 during GMN9319TP salt spray testing and found that a fine lamellar (α + β) structure provided an effective barrier to corrosion [17]. Pardo et al. also witnessed a similar effect on cast AZ80 where lamellar grains remained relatively unaffected during a 28-day immersion in 3.5 wt % NaCl solution [10]. An apparent barrier layer of Al_2O_3 formed at the grain boundaries, which impeded the advancing corrosion front. A high clarity SEM image of the Al_2O_3 barrier layer, shown in Figure 2.3 was presented and a three-stage mechanism for the formation of the barrier layer was proposed. Song et al. suggested that once this barrier layer was formed, corrosion rates of the AZ alloy closely followed those of the β phase itself rather than the predominant α matrix phase [15]. Corrosion rates of the β phase in 5% NaCl solution have been reported by Lunder et al. to be much slower than the matrix phase on AZ alloys [13]. The rationale behind the excellent corrosion resistance is related to the synergistic effect of having a large amount of Al and Mg inherent in the $Mg_{17}Al_{12}$ phase composition [13]. The β phase possesses the passive properties of Al in neutral solutions and of Mg in alkaline solutions allowing for good corrosion resistance over a broad range of pH.

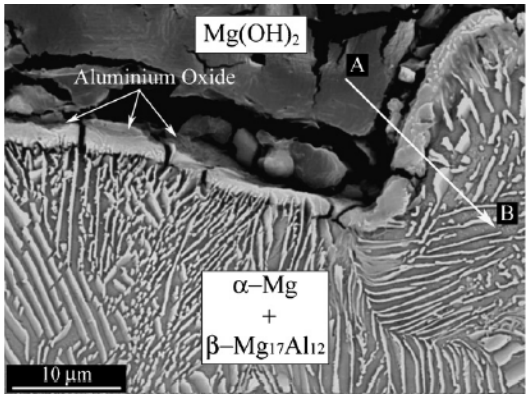

Figure 2.3: High-resolution image of the barrier layer formed around lamellar (α + β) grains on AZ80 immersed in 3.5 wt % NaCl solution for 28 days. [10]

If lamellar structures are not present, a fine grain structure with a finely precipitated and nearly continuous β phase distribution at grain boundaries likely produces the barrier layer [15]. Regardless of the inherent possibility of forming a barrier layer, it is clear that no definitive understanding of when the corrosion barrier will or will not form has been reached.

The β phase can also form microgalvanic couples with the α matrix if the distribution of this secondary phase is non-uniform and discontinuously distributed throughout the microstructure [6, 10, 12-17]. Lunder et al. reported the galvanic potential of the β phase was much higher than that of the matrix phase, and thus, a large driving force for microgalvanic corrosion was present [13]. Song et al. found that the β phase formed an efficient galvanic cathode if the grain size of the AZ alloy was large, the β phase was agglomerated and large distances between β particles were present [15]. This unfavourable distribution is unable to form a continuous barrier layer, and therefore, aggressive ions such as Cl^- are able to penetrate through gaps in the β phase network and attack the more susceptible α phase [12]. Unfortunately, similar to the studies on AlMn

intermetallic particles, no clear understanding of the influence of the β phase on the kinetics of microgalvanic corrosion within AZ alloys has been reached. Although a large thermodynamic driving force between the α and β phases is present, this parameter does not give any insight into the speed at which the galvanic reaction occurs.

2.3.3 Passive Film Structure and Composition

The properties of the passive film play an important role in determining the corrosion resistance of AZ alloys. Generally, the surface of AZ alloys is unable to form a spontaneous protective corrosion film [2]. Numerous studies have been performed in various environments to attempt to characterize and improve the properties of the surface film formed on AZ alloys [2, 5, 6, 8, 9, 14, 19, 22, 26, 31, 33, 37, 39, 43-44, 62-63].

In humid atmospheres, the rate of oxide growth is slower than in aqueous conditions, and thus, the mechanism of oxide formation can be more readily studied. Splinter and McIntyre found that the oxide film formed on Mg-Al alloy surfaces exposed to D_2O water vapour grew via a three stage process; similar to the growth of the oxide film on pure Mg [8]. The three stages included dissociative chemisorption, oxide island nucleation and coalescence, as well as logarithmic bulk thickening. In the case of AZ alloys, Al^{3+} cations are incorporated into the air-formed oxide and the bulk thickening rate is decreased as concentration defects inherent within the MgO film are removed due to charge deficiencies caused by Al^{3+} enrichment. After the oxide forms, the presence of humidity produces a thin hydroxide layer over the surface as the oxide begins to hydrate. Fournier et al. observed this thin hydroxide layer on pure Mg when exposed to H_2O vapour using XPS [63]. Feliu Jr. et al. also reported that the presence of humidity caused

the air-formed MgO to hydrate and form a poorly protective outer $Mg(OH)_2$ layer [6]. Nordlien et al. did not observe the outer hydroxide layer on AZ alloys under TEM [5]. Since all other studies reported a thin hydroxide outer layer, the hydroxide was likely present but only a few monolayers thick and very difficult to distinguish under TEM. Therefore, it is evident that even in humid exposures, the air-formed oxide reacts with water vapour and slowly transforms into a weakly protective hydroxide layer on the surface of AZ alloys.

The reason for this slow transformation is related to the hydration rate of MgO to $Mg(OH)_2$. Thermodynamically, this hydration reaction is particularly favourable in acidic and neutral environments [64]. In alkaline environments, the rate of hydration is significantly slower, and as a result, the stability of the air-formed MgO is improved [65]. Regardless of the pH of the environment, the air-formed MgO oxide film undergoes chemical breakdown, as it slowly transforms to $Mg(OH)_2$. This chemical breakdown influences the corrosion resistance of AZ alloys as a MgO layer is significantly more protective than a $Mg(OH)_2$ layer on the surface [26]. According to Mejias et al., hydration of MgO to $Mg(OH)_2$ requires defect sites within the structure of the MgO and they observed no hydration occurring on single crystal MgO surfaces after several days of aqueous exposure [66]. Therefore, it is feasible that if the surface of the air-formed MgO could be controlled, the hydration rate and breakdown of this layer would be vastly reduced. Currently, no definitive study is available that addresses this issue, and therefore, hydration will continue to play a major role in the naturally formed corrosion films on AZ alloys in aqueous environments.

The surface film formed on Mg and AZ alloys when exposed to water has been studied [5, 9, 33, 37]. Nordlien et al. found that a three-layer film structure was present on the surface of AZ alloys when exposed to distilled water for 48 hours [5]. The inner layer was significantly affected by TEM beam irradiation damage, and as a result, was unable to be identified. A dense, Al enriched air-formed MgO, similar to what Splinter and McIntyre [8] reported, constituted the inner layer and a porous platelet-like outer layer indicative of a dissolution-precipitation reaction completed the film structure. A schematic representation of the film is shown in Figure 2.4. Although Nordlien et al. witnessed the corrosion film under TEM, the results of their study regarding the presence of three distinct layers of the corrosion film on AZ alloys remains unique and not corroborated.

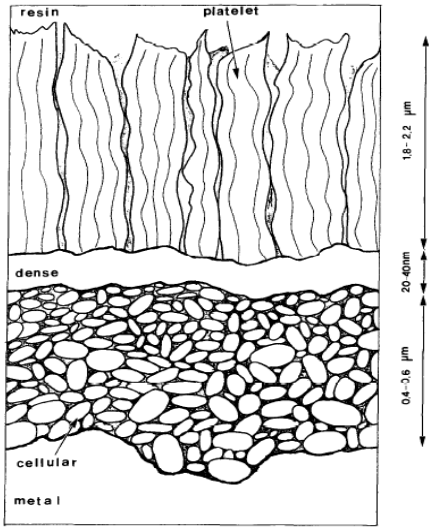

Figure 2.4: Schematic representation of the corrosion film on AZ alloys after 48 hour exposure to distilled water. [37]

Santamaria et al. reported a duplex film structure of $MgO/Mg(OH)_2$ on the surface of pure Mg when exposed to pure water for short times using XPS [39]. In

addition, Liu et al. performed a similar experiment, exposing Mg to ultrapure water and XPS analysis revealed a duplex film structure, similar to that reported in humid environments; only the hydroxide layer was much thicker [33]. As exposure time increased, they also observed the $Mg(OH)_2$ layer becoming more dominant within the surface film as expected due to hydration.

Extensive study of the corrosion film structure and composition on AZ alloys has been undertaken in mildly aggressive saline solutions [14, 19, 22, 43, 44, 62]. Song et al. found that a bi-layer film structure of $MgO/Mg(OH)_2$ on AZ21, AZ91 and AZ501 exposed to 1 N NaCl solution was present using XPS and EIS [19]. They also proposed the possibility of a thin, continuous healing layer of Al_2O_3 beneath the surface of the air-formed MgO on AZ21 and AZ91 but could not verify its existence. In addition, it was reported that as alloyed Al concentration increased, the properties of the passive film were controlled predominantly by the properties of the Al_2O_3 rather than the MgO. Due to the superiority of the Al_2O_3 with respect to the MgO as a barrier layer, the thickness of the corrosion film significantly decreased as alloyed Al content increased. A schematic representation of the Song et al. film model is shown in Figure 2.5.

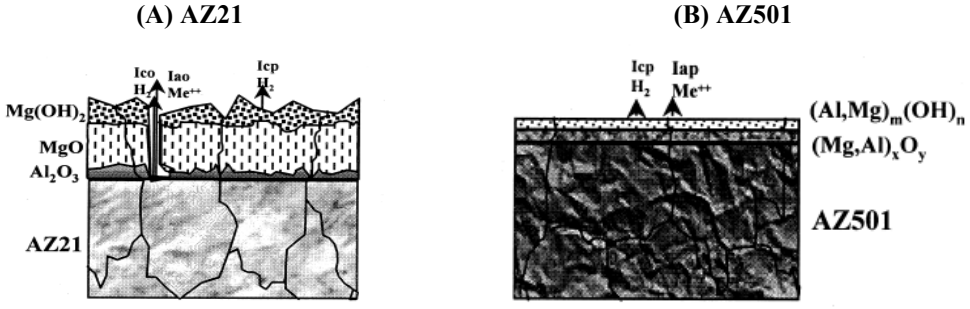

Figure 2.5: Schematic representation of the corrosion film structure on AZ alloys exposed to 1 N NaCl solution (A) AZ21 (B) AZ501. [19]

Mathieu et al. observed a completely different passive film structure on AZ91 exposed ASTM D1384 corrosive water [14]. Instead of a bi-layer $MgO/Mg(OH)_2$ film structure, they reported a layered double hydroxide film of hydrotalcite with alternating layers of mixed Mg/Al hydroxide and carbonate. The proposed film structure is presented in Figure 2.6. Baliga et al. also reported a similar hydrotalcite structure on Mg-16Al splat-quenched alloy using TEM, RBS and EDX [22]. Carbonate has been identified as playing a small role in the composition of the corrosion film by many authors and its common location is at the exterior of the hydroxide layer [6, 26, 45]. Hydrotalcite coatings have commonly been fabricated and tested on AZ alloys, but these films are not naturally occurring [2]. No images of a naturally formed layered double hydroxide hydrotalcite film are available.

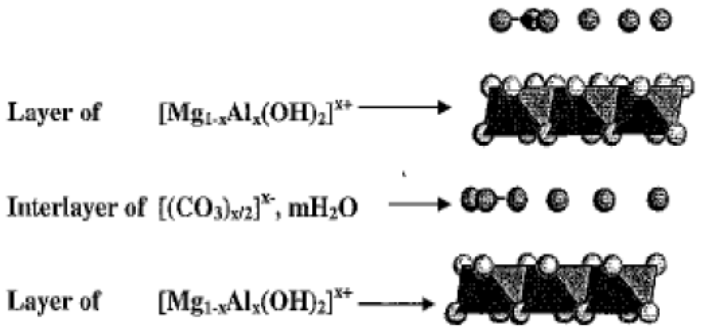

Figure 2.6: Schematic representation of the corrosion film on AZ91 exposed to ASTM D1384 water. [14]

Distinct layers of the corrosion film on AZ alloys have not always been reported in the literature [44, 62]. Yao et al. found that the corrosion film on melt-spun Mg ribbons exposed to 3% NaCl solution was a mixture of MgO and $Mg(OH)_2$ and no distinct layers were identified [62]. Wang et al. was also unable to identify distinct layers

of the corrosion film on AZ31 or AZ91 when exposed to 0.01 M NaCl solutions [44]. Mixtures of MgO and $Mg(OH)_2$ were located at the inner layer and a mixture of $Mg(OH)_2$ and $MgCO_3$ was identified via XPS at the outer layer. Al^{3+} cations were enriched into the corrosion film and assisted in stabilizing the corrosion film. It is clear from the above research findings that no definitive conclusion regarding the naturally forming corrosion film structure on AZ alloys when exposed to aqueous solutions has been determined.

2.3.4 Stability and Breakdown of Passive Film on AZ Alloys

The surface film on AZ alloys is passive until the breakdown potential is reached. Corrosion rates at E_{corr} are generally relatively low and as a result, the surface film can be deemed stable [3, 7, 14, 15, 19, 21, 31, 43]. However, depending on the aggressiveness of the solution, breakdown potentials are observed at varying anodic overpotentials. When the concentration of Cl^- ions is low, small regions of passivity are present and breakdown potentials appear only after anodic polarization has occurred [43]. In contrast, in highly aggressive 3.5 – 5 wt % NaCl solutions containing high concentrations of Cl^- ions, breakdown potentials are commonly absent even though wide scale pitting of the surface is evident [3, 15, 19, 21]. Therefore, the breakdown potential in these environments must be at E_{corr} and no surface film stability region is present on AZ alloys. Pardo et al. reported that breakdown initiated via microgalvanic activity at AlMn intermetallic particles or regions comprised of the β phase [10]. Song et al. and Lunder et al. also proposed breakdown of the surface film occurred at cathodic sites in the AZ alloy microstructure [4, 15].

However, the aforementioned results of Yao et al. and Wang et al. showed that breakdown of the inner MgO barrier layer occurred similarly despite marked differences in microstructural features [44, 62]. Therefore, microgalvanic activity may not play a significant role in the breakdown of the inner MgO barrier layer. Hydration could be responsible or environmental factors such as Cl^- concentration. Williams et al. proposed that breakdown of the corrosion film on Mg was related to the Cl^- concentration of the solution and not microstructural influences [67]. The breakdown potential would occur at different potentials depending on the concentration of Cl^- ions in the test solution. Therefore, the breakdown of the inner MgO barrier layer may not be a classical electrochemical breakdown, where specific anodic and cathodic sites cause localized breakdown of the film.

It is clear that the structure and composition of the corrosion film on AZ alloys remains largely uncertain. Generally, it appears as though the corrosion film is likely bi-layer in structure consisting of an easily compromised MgO inner layer and a porous $Mg(OH)_2$ outer layer. However, this structure has still yet to be imaged and as a result, uncertainty in its presence still exists amongst many researchers. The Nordlien et al. tri-layer structure is still commonly referred to as the true representation of the natural corrosion film on AZ alloys even though no further experimental evidence has been provided by another research group.

2.3.5 pH Effect

Thermodynamically, an alkaline pH greater than approximately 11.5 should produce a significantly more stable corrosion film on AZ alloys than a neutral or acidic

pH. Evidence of this property can be observed in the Pourbaix diagram for Mg, as shown in Figure 2.7A, where $Mg(OH)_2$ is insoluble at pH > 11.5. However, the beneficial passive properties of Al_2O_3 in neutral environments disappear, as the soluble anion AlO_2^- is the stable corrosion product in alkaline solutions, as shown in Figure 2.7B.

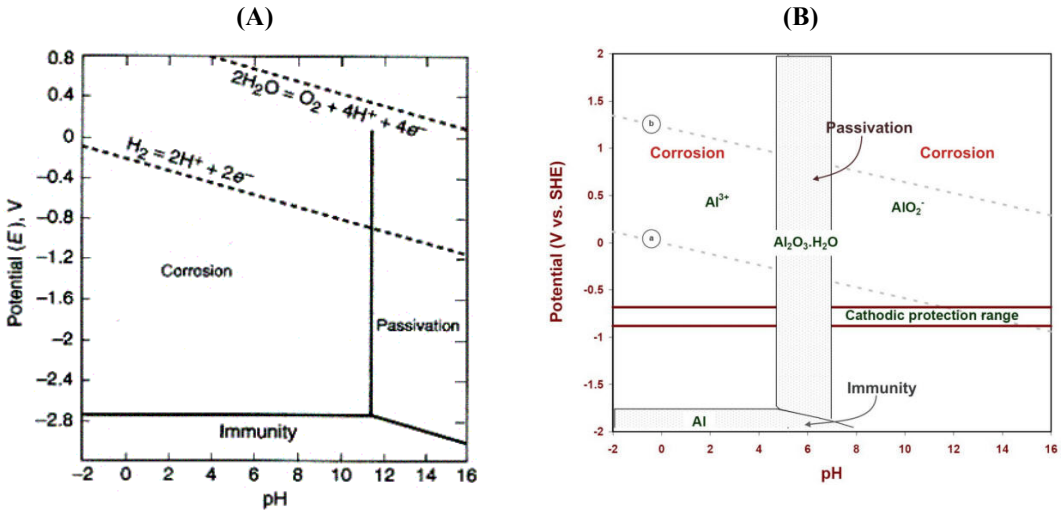

Figure 2.7: Pourbaix diagrams for (A) magnesium [68] **(B) aluminum.** [69]

The pH of the exposure environment significantly affects the corrosion resistance of AZ alloys [7, 38, 56, 58, 70]. Specifically, little resistance to corrosion is achieved in neutral or acidic environments, however in alkaline environments, corrosion hardly occurs [56, 58]. For example, in two separate works the corrosion current of AZ31 in alkaline solution was reported to be three orders of magnitude smaller than the corrosion current in a neutral environment [31, 43]. In addition, Badawy et al. studied the pH effect on AZ alloys and found significant reductions in corrosion rate as pH increased from acidic to neutral to alkaline conditions [7]. Furthermore, Ambat et al. found that corrosion rate of AZ91D exposed to 3.5 wt % NaCl was significantly reduced as the pH of the solution was increased to 12 [71]. Hallopeau et al. also saw reductions in corrosion

rates on AZ91E exposed to 0.5 M Na_2SO_4 as the pH increased from neutral to alkaline pH [72]. They also reported that the corrosion behaviour of AZ91E in pH > 13 was controlled by the properties of the Mg metal and alloyed Al had little effect on the observed corrosion resistance. At pH < 10.5, Al strongly influenced the corrosion behaviour of the AZ91E alloy. From the literature, it is clear that extensive natural passivation of AZ alloys is attainable in alkaline conditions and an attempt to duplicate this behaviour in neutral environments needed to be undertaken.

Anodizing is a logical technique to exploit the passive properties of the corrosion film formed on AZ alloys in alkaline environments. Anodizing is a common surface treatment used as a corrosion control strategy for automotive components [24]. AZ alloys are subject to high electrical voltages in alkaline solutions to produce a thick anodic film of MgO on the surface [24]. The film of MgO is formed in the secondary passivation regime of the anodization process where very high electrical voltages are attained [24]. After the film is formed, a sealant is applied as a coating and components are ready for use in automotive applications. While anodizing takes advantage of the passive properties of AZ alloys in alkaline environments, the anodic film formed is not a result of primary or natural passivation of the AZ alloy [24].

Natural passivation in alkaline environments occurs at much smaller electrical overpotentials, and although many researchers have studied its electrochemical behaviour, the corrosion film itself has rarely been studied [7, 31, 71, 72]. Ismail and Virtanen investigated the surface film on AZ31 when exposed to 0.5 M KOH (pH =13.5) solution using XPS along with EIS and found a bi-layer film structure of $MgO/Mg(OH)_2$

was present [31]. Therefore, it is likely that the surface films formed on AZ alloys in near-neutral and alkaline environments are strikingly similar. However, as previously mentioned, the electrochemical behaviours of AZ alloys in the two environments are drastically different.

2.4 Research Questions and Objectives

Throughout the literature review it was clear that some fundamental areas related to the natural corrosion of AZ alloys were lacking in knowledge. Furthermore, research findings concerning the corrosion resistance of AZ alloys are commonly inconsistent. The following research objectives will be discussed and analyzed throughout this work in an attempt to better understand the natural corrosion process of AZ alloys:

1. Investigate the structure and composition of the surface film formed in both neutral and alkaline environments to understand the effect of pH on the corrosion performance of AZ alloys.
2. Examine the effect of alloyed Al on the corrosion performance of AZ alloys and attempt to discover the specific mechanism(s) responsible for the improved corrosion resistance compared with pure Mg.
3. Investigate the stability of the corrosion film in mildly aggressive salt environments and discover what factors control the initiation of breakdown of the surface film.

3 Experimental Details

3.1 Materials

Commercial 99.99% (4N) Mg, as well as a variety of binary Mg-Al and ternary-based Mg-Al-Zn (AZ) alloys were utilized throughout the thesis project. The alloys can be broken up into two separate classes based on their production conditions: commercial and laboratory. The AZ alloys were fabricated in an industrial setting and are commercially available, whereas the Mg-Al binary alloys were produced in a laboratory setting. In order to omit any discrepancies between industrial and laboratory processing conditions, the alloys within each class were only compared to each other and not to those of dissimilar processing conditions.

3.1.1 Commercial 4N Mg

A wrought, polycrystalline Mg plate was included in the electrochemical testing portion of the thesis. The plate was obtained from Natural Resources Canada (CANMET-MTL) in the as-rolled condition. To homogenize the grain structure, the plate was annealed at 350°C for 0.5 hours and quenched in water.

3.1.2 Commercial Mg-Al-Zn (AZ) Alloys

The AZ alloys used in the thesis project were wrought AZ31 and AZ80. The AZ31 alloy was received in sheet form and was supplied by General Motors in the as-rolled condition. In contrast, the AZ80 alloy was received in the as-cast condition; fabricated using a direct chill casting process at the University of British Columbia. Both as-received alloys were subject to a 6 hour annealing heat treatment at 400°C. This treatment recrystallizes and slightly coarsens the grain structure [73, 74]. The purpose of recrystalizing the grains was to remove any inherent deformation caused by the

fabrication or cutting of the samples, as well as to produce a homogenized, wrought grain structure. Consequently, experiments comparing the two AZ alloys had no bearing on the past processing conditions of the alloys.

3.1.3 Binary Mg-Al Alloys

A variety of binary Mg-Al alloys, specifically, Mg-2Al, Mg-3Al, Mg-5Al, Mg-7Al and Mg-9Al were utilized in the electrochemical testing portion of the thesis. All binary alloys were received as extruded rods, produced by the National Research Council of Canada. No post-processing heat treatment was performed on these alloys due to their similar fabrication condition. Instead, the alloys were used to solely compare the electrochemical effect of alloyed Al concentration; the only variable changing between alloys.

3.2 Materials Characterization

3.2.1 Commercial 4N Mg

To verify the 99.99% purity of the Mg plate, Inductively Coupled Plasma Atomic Emission Spectroscopy (ICP-AES) was performed. The result of the measurement is shown below in Table 3.1. Impurity concentrations of Fe, Cu, and Ni were all within the required impurity threshold limits for 4N Mg samples.

Table 3.1: ICP-AES chemical analysis of 4N Mg.

	Atomic Concentration (ppm)							
Alloy	Al	Zn	Mn	Cu	Fe	Ni	Si	Mg
Mg	9.0	1.1	22	32	51	9.0	2.0	Balance

The annealed microstructure of the 4N Mg plate was obtained through standard laboratory metallography and is shown in Figure 3.1. Impurity particles were present throughout the microstructure and are indentified in Figure 3.1.

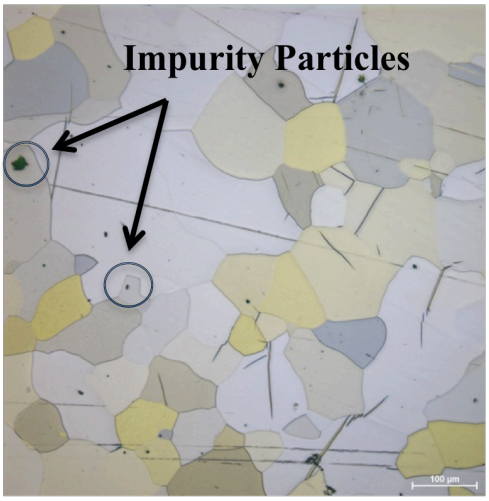

Figure 3.1: Light optical microscopy image of 4N Mg microstructure: magnification 200X.

3.2.2 Mg-Al-Zn (AZ) Alloys

To characterize the chemical composition and microstructure of the AZ31 and AZ80 alloys, ICP-AES and standard laboratory metallography were performed. The results of the ICP-AES analysis are shown below in Table 3.2.

Table 3.2: ICP-AES chemical analysis of AZ alloys.

	Atomic Weight %							
Alloy	Al	Zn	Mn	Cu	Fe	Ni	Si	Mg
AZ31	3.0	0.97	0.40	3.0E-03	6.0E-03	2.0E-03	1.0E-03	Balance
AZ80	7.8	0.43	0.26	2.0E-03	6.0E-03	2.0E-03	4.0E-03	Balance

In order to obtain quality micrographs, a detailed and delicate polishing procedure was undertaken. To begin, the samples were mounted using an epoxy, which required no heat or pressure to fabricate the mould. This is an important step since using a pressurized mounting press easily deformed the microstructure of the sample. Samples were then ground progressively using 1200 and 2400 grit silicon carbide (SiC) grinding paper with water as the lubricant. Next, the samples were auto-polished using 9 μm and 3 μm diamond suspensions on NAP polishing cloths with 20% glycerin, 80% ethylene glycol as the lubricant. The generic 1 μm OPS polishing stage was omitted because the

samples were not viewed under electron microscope. As a result, all issues regarding unwanted intermetallic removal and cleaning of the sample surface were avoided.

Etching was conducted using an acetic picral etchant: ASTM Etchant 8 [75]. The etchant was applied to the sample surface with a pipette and once the etchant turned brown (about 5 seconds), the sample was rinsed with ethanol and dried with a stream of warm air. The samples were immediately examined under a generic optical microscope and additional etching was conducted if the microstructure remained unclear.

Micrographs were taken with a Nikon LV100 Eclipse microscope at various magnifications. The general microstructures of AZ31 and AZ80 are shown in Figure 3.2. AZ31 has a single-phase microstructure with numerous intermetallic particles. These particles are consistent in size and shape with the AlMn particles reported in the literature [10]. The grain size was estimated qualitatively to be 10-20 μm and was uniformly distributed throughout the microstructure. In contrast, the AZ80 alloy has a two-phase microstructure, consisting of an Mg-Al-Zn solid solution phase and the $Mg_{17}Al_{12}$ (β) intermetallic phase [52]. Figure 3.2C shows a high-resolution micrograph of the β intermetallic phase. It was observed that the β phase forms a semi-continuous network along the grain boundaries of the Mg-Al-Zn solid solution phase. Furthermore, large lamellar colonies are apparent within specific grains. Intermetallic particles of AlMn were also present in the microstructure but were not captured by the images in Figure 3.2B or C.

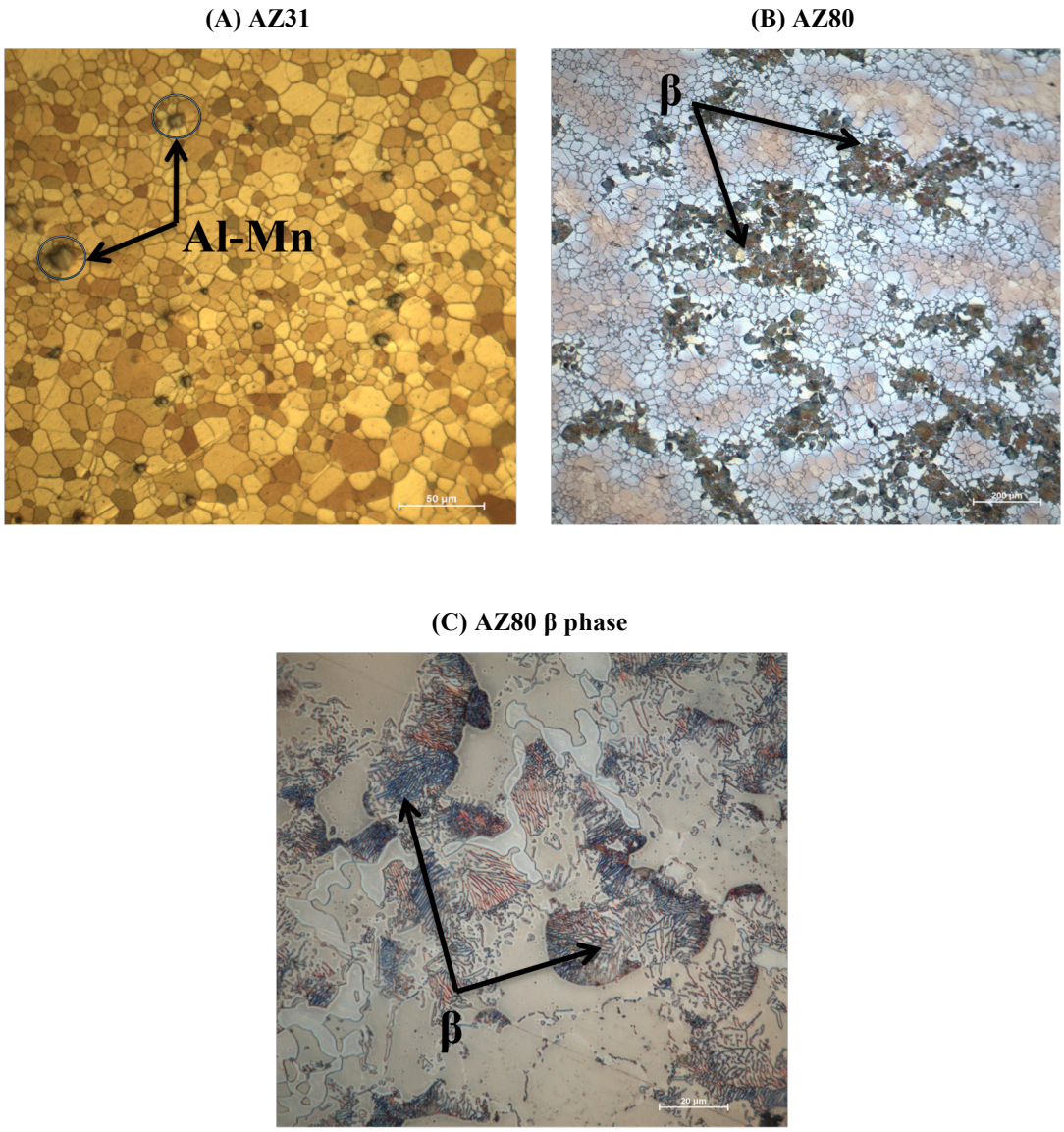

Figure 3.2: Light optical microscope images of recrystallized microstructures of (A) AZ31, (B) AZ80 and (C) AZ80 β phase.

3.2.3 Binary Mg-Al Alloys

Due to the number of binary Mg-Al alloys studied, Glow Discharge Optical Emission Spectroscopy (GDOES) was utilized to characterize the chemical composition. Prior to chemical analysis, the GDOES gas spectrometer was calibrated using Mg standards provided and certified by MBH® Analytical LTD. Table 3.3 lists the Mg standards utilized and their chemical compositions.

Table 3.3: Mg standards utilized for GDOES calibration.

	Element Weight %						
Standard	Al	Zn	Mn	Cu	Si	Fe	Ni
61X MGP2	6.50E-02	1.22E-02	1.18E-02	1.09E-02	2.90E-02	6.10E-03	2.90E-03
65X MGA11	3.63	1.59	4.40E-02	9.96E-02	2.20E-02	4.90E-03	1.34E-02
65X MGA12	5.68	3.18	1.98E-01	2.66E-01	1.42E-02	5.30E-03	1.48E-02
65X MGA13	7.45	0.925	9.20E-02	1.25E-01	2.20E-02	8.00E-03	3.90E-03
65X MGA14	9.09	0.685	2.82E-01	1.02E-02	8.00E-02	8.00E-03	8.20E-03
65X MGA21	12.4	5.11	7.80E-02	2.00E-03	2.80E-02	1.40E-02	1.00E-03

The purpose for using GDOES was related to the speed of analysis and limited material consumption. Since the approximate composition of the binary Mg-Al alloy samples was previously known, this step was only necessary to properly label the samples provided. The compositions determined by GDOES are listed in Table 3.4.

Table 3.4: GDOES analysis of binary Mg-Al alloy composition.

Mg-2Al					
Element	**Result**	**SD**	Measure 1	Measure 2	Measure 3
Mg	**98**	**0.020**	98	98	98
Al	**1.7**	**0.010**	1.7	1.7	1.7
Zn	**0.040**	**0**	0.040	0.040	0.030
Mg-3Al					
Element	**Result**	**SD**	Measure 1	Measure 2	Measure 3
Mg	**97**	**0.010**	97	97	97
Al	**2.6**	**0.020**	2.6	2.6	2.6
Zn	**0.030**	**0.020**	0.020	0.020	0.060
Mg-5Al					
Element	**Result**	**SD**	Measure 1	Measure 2	Measure 3
Mg	**96**	**0.030**	96	96	96
Al	**4.4**	**0.030**	4.4	4.4	4.3
Zn	**0.040**	**0.010**	0.040	0.030	0.050
Mg-7Al					
Element	**Result**	**SD**	Measure 1	Measure 2	Measure 3
Mg	**93**	**0.040**	93	93	93
Al	**6.8**	**0.040**	6.8	6.8	6.7
Zn	**0.030**	**0.010**	0.020	0.040	0.040
Mg-9Al					
Element	**Result**	**SD**	Measure 1	Measure 2	Measure 3
Mg	**91**	**0.10**	91	91	91
Al	**8.9**	**0.080**	9.0	9.0	8.8
Zn	**0.040**	**0.020**	0.070	0.020	0.020

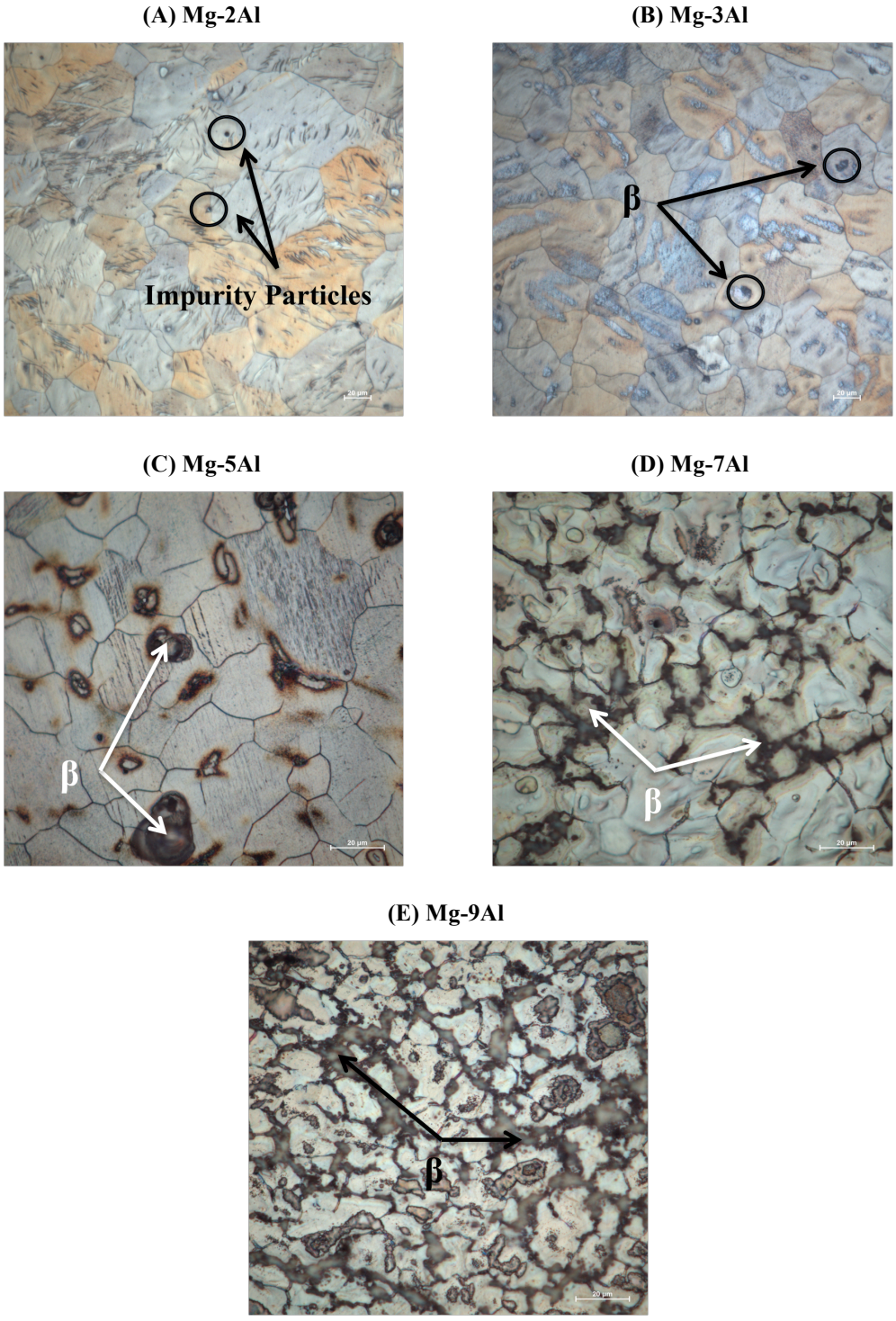

Figure 3.3: Light optical microscope images of microstructure of (A) Mg-2Al, (B) Mg-3Al, (C) Mg-5Al, (D) Mg-7Al and (E) Mg-9Al.

3.3 Electrochemical Measurements

3.3.1 Sample Preparation

All samples tested electrochemically had an area of 1 cm^2, a thickness of approximately 2-3 mm and were prepared via a five-stage process. First, a frayed end of a copper wire was taped to the back side of the sample and the connection was tested with a voltmeter to ensure electrical contact was present. Second, the sample surface, which would be exposed to the electrolyte, was superglued to a mounting mould. This step ensured that the sample remained flat against the bottom of the mould when the cold mounting epoxy was poured. Third, cold mounting epoxy was mixed and poured into the moulds over the samples and allowed to set for a minimum of 12 hours. Fourth, samples were removed from the moulds and using a quick-set epoxy, drinking straws were glued over the exposed length of copper wire to provide the sample with some rigidity when it was suspended inside an electrochemical cell. Fifth, the samples were polished with 1200 and 2400 grit SiC papers to remove any trace of tape, glue or dirt on the surface, as well as to obtain a freshly exposed metallic surface for testing. Figure 3.4 shows the completed sample construction used throughout the electrochemical testing section of the thesis.

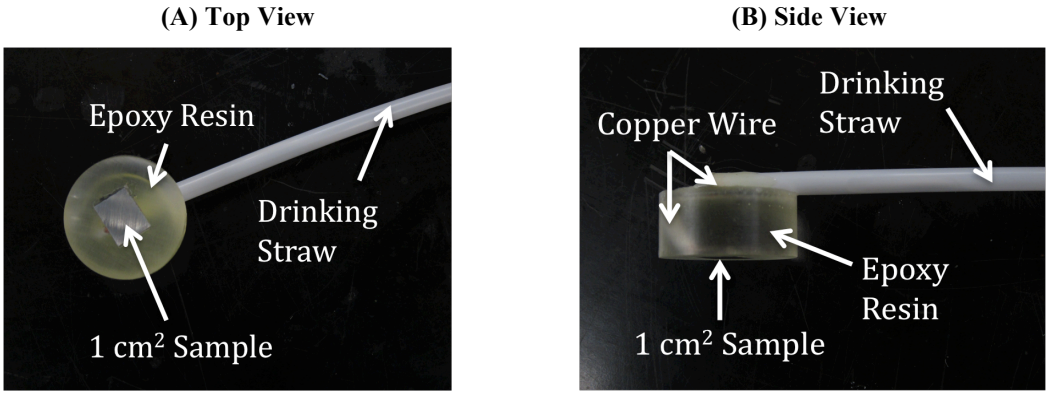

Figure 3.4: Electrochemical sample construction from (A) top view and (B) side view.

3.3.2 Electrochemical Cell Apparatus

For all experiments, a 1 L Gamry Multiport™ 3-electrode electrochemical cell was utilized. A saturated calomel electrode (SCE) was used as the reference and a graphite rod as a counter electrode. The working electrode was suspended from a clamp over the cell using the drinking straw for structural support. Figure 3.5 shows the experimental setup.

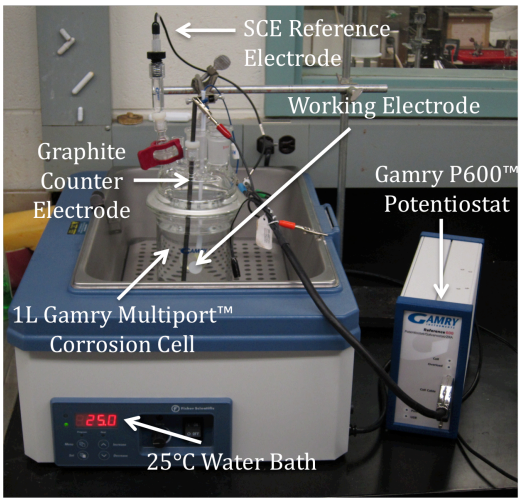

Figure 3.5: Experimental apparatus setup for electrochemical measurements.

3.3.3 Electrolyte Solutions

For electrochemical experiments, moderately corrosive 0.01 M NaCl solutions were exclusively used. This concentration was chosen, since solutions of 3.5 wt % NaCl were found to be too aggressive during preliminary experiments.

All solutions mixed for experimental testing used ultrapure water as a solvent. To produce the near-neutral 0.01 M NaCl solutions, 0.5845 g of metallurgical grade NaCl was added to 1 L of ultrapure water. For the pH 14 solutions, the same procedure was followed, however, 40 g of NaOH were also added to adjust the pH to 14. Solutions were

magnetically stirred and heated to a temperature of 25°C in a Fisher Scientific water bath where the experiments took place.

3.3.4 Corrosion Potential (E_{corr}) Experiments

E_{corr} monitoring experiments were performed using a Gamry Reference 600™ potentiostat and the Gamry Framework™ software package. Tests were conducted for a minimum of 30 minutes prior to each electrochemical measurement. This ensured that the E_{corr} was stable before any further testing was initiated.

3.3.5 Potentiodynamic Experiments

All potentiodynamic polarization experiments were conducted after the E_{corr} stabilization period. This assured that meaningful polarization curves were produced. Similar to the E_{corr} experiments, the potentiodynamic scans were carried out on a Gamry Reference 600™ potentiostat using the Gamry Framework™ software package. The scan rate was 1 mV/s and the scanned range was at least 250 mV either side of the measured E_{corr}. Each polarization curve was repeated at least once per sample to ensure the reproducibility of the experiment.

Potentiodynamic polarization curves were used to quantitatively compare corrosion behaviour amongst the different commercial and laboratory alloys tested. Values for i_{corr}, E_{corr}, β_c and $i_{o,c}$ were calculated using the Gamry Framework™ cathodic Tafel extrapolation method. For the pH 14 samples, limiting anodic current densities were present and these were used to calculate the maximum corrosion rate.

3.3.6 Linear Polarization Resistance (LPR) Experiments

LPR measurements were conducted to obtain rapid short-term corrosion rates and to compare with the rates calculated via the cathodic Tafel extrapolation method. As

before, the Gamry Reference 600™ potentiostat and Gamry Framework™ software package were used to perform all experiments. Prior to the LPR tests, the E_{corr} was required to stabilize as mentioned previously.

A LPR measurement, which included a +/- 50 mV overpotential about the $E_{corr,}$ was conducted on all commercial alloys. Tafel constants were approximated as $\beta_a = \beta_c =$ 0.12 V and the software package was used to determine the polarization resistance (R_p).

3.4 Surface Analysis Measurements

Commercial AZ alloys were exclusively used for surface analysis by STEM-EDS and ToF-SIMS. All samples were 1 cm^2 and approximately 2-3 mm thick. A total of six samples were produced: three for both STEM-EDS and ToF-SIMS analysis. The STEM-EDS samples produced were: 'AZ80 – pH 7,' 'AZ80 – pH 14' and 'AZ31 – pH 14.' The ToF-SIMS samples produced were: 'AZ80 – unexposed,' 'AZ80 – pH 7' and 'AZ80 – pH 14.' Each sample (excluding 'AZ80 – unexposed') was ground to 4000 SiC grit and exposed to near-neutral or pH 14 ultrapure water for 48 hours at E_{corr}. 'AZ80 – unexposed' was ground to 4000 SiC grit, exposed to ambient laboratory atmosphere and was used as a control sample for the ToF-SIMS experiment. Once the 48-hour period expired, the samples were rinsed with ethanol and dried in a stream of warm air.

A dessicator was used to transfer samples to the respective microscope chambers to avoid contamination from the ambient atmosphere. STEM-EDS samples were transferred to the FIB chamber in less than 15 minutes and ToF-SIMS samples spent approximately 24 hours in the dessicator.

3.4.1 Focused Ion Beam (FIB)

FIB specimens were prepared at the Canadian Centre for Electron Microscopy (CCEM) at McMaster University. Cross-sectional samples for STEM-EDS observations were prepared using a ZeissNVision 40 FIB/SEM. The specimens were milled with a Ga^+ ion beam at an accelerating voltage of 30 kV and thinned using the lift-out method. SEM observations of the general overview of the sample surface, as well as selections of the sites of interest were obtained with the same instrument. The accelerating voltage was set at either 5 or 10 kV and the FIB image probe was operated at 30 kV with a current of 80 pA.

3.4.2 STEM-EDS Analysis

STEM-EDS analysis was also conducted at the CCEM. Specimens produced with the FIB were analyzed using an FEI Titan 80-300 microscope. The accelerating voltage was 300kV and a spherical aberration corrector of the imaging lens was used. Samples were held at 77 K by cryogenically cooling the sample holder with liquid N_2 to avoid beam irradiation damage, which was significant in the first sample analyzed without any cooling. The High Angle Annular Dark Field (HAADF) STEM mode was primarily utilized for imaging.

Energy Dispersive X-ray Spectroscopy (EDS) was carried out using an Oxford Instruments detector. Due to the sensitivity of the corrosion film, line scans were unsuccessful, as the beam burned through the film region before the scan was completed. Instead, multiple SmartMaps™ were acquired for the elements Mg, Al, and O for each sample examined. SmartMaps™ rastered the beam over a region of the sample to collect

data, which avoided much of damage incurred by focusing the beam when conducting line scans.

3.4.3 SmartMap™ Quantification Procedure

In order to extract useful information about the corrosion film structure and composition, SmartMaps™ were utilized. In their raw form, a SmartMap™ is simply a pixel map that represents elemental concentration at specific sites within the map. Therefore, to obtain concentration versus depth distributions, a procedure was conceptualized and employed for the analysis.

To begin, sites of interest, such as interface boundaries within the corrosion film were identified and their depth from the surface were mapped using the scale bar from the HAADF image. These sites of interest were approximately every 20 nm from the surface of the film. Next, a grid of similarly sized boxes was drawn over the entire SmartMap™ at the aforementioned sites of interest. These boxes each contained an individual EDS spectrum that was quantified using the Inca™ diffraction software package. Each spectrum was quantified and the results were graphed as a scatter plot of atomic concentration versus depth from the surface. Knowledge of the expectant phases allowed for the identification of interface boundaries based upon (Mg + Al) : O ratio from the scatter plot. The locations of the interface boundaries were then compared to the HAADF images. An average concentration value of Mg, Al, and O was then computed over each phase region to approximate semi-quantitatively the composition of the constituent layers of the corrosion film.

3.4.4 ToF-SIMS Analysis

ToF-SIMS analysis was performed at Surface Interface Ontario at the University of Toronto. Negative depth profiles were acquired using an Ion-ToF IV and a 3 keV Cs^+ source with a current of 22.5 nA over an area of 150x150 μm. Analysis was then conducted over a 50x50 μm area using a 25 keV Bi^+ source. All profiles were collected in interlaced mode. To present the data, the IonSpec™ software package was utilized.

4 Results

4.1 Electrochemical Measurements – Commercial Alloys

4.1.1 E_{corr} Measurements – 0.5 Hours

E_{corr} curves for 4N Mg, AZ31 and AZ80 in the near-neutral (pH ≈ 7), as well as the alkaline (pH = 14) 0.01 M NaCl exposure condition are shown in Figure 4.1. For the pH ≈ 7 environment, it was observed that the E_{corr} of the AZ31 and AZ80 were similar in magnitude, about 50 mV nobler than the 4N Mg. The 10 mv E_{corr} difference was likely experimental error and therefore, was not viewed as significant. For all three samples, the E_{corr} initially increased steadily before leveling off near the end of the experiment. At that point, it was assumed that a steady state had been reached.

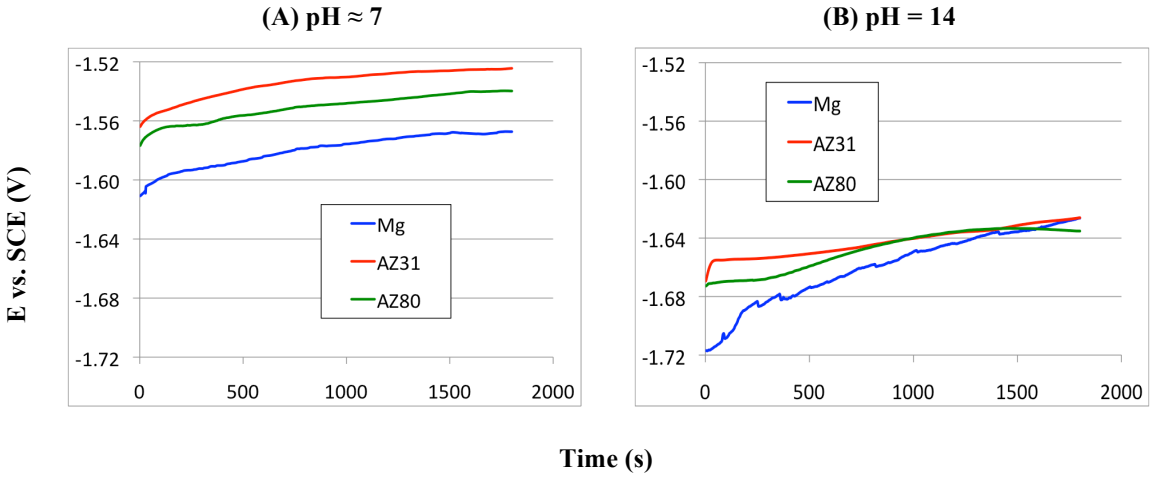

Figure 4.1: E_{corr} curves of 4N Mg, AZ31 & AZ80 exposed to 0.01 M NaCl solution for 0.5h in (A) near-neutral (pH ≈ 7) and (B) alkaline (pH = 14) environments.

In the pH =14 alkaline environment, the E_{corr} values slowly rose for the majority of the experiment and when the test concluded, the E_{corr} values for all three samples were within 10 mV of each other. Similar to the pH ≈ 7 environment, it was assumed at this point that the samples had reached a steady state condition. Furthermore, it appeared that alloyed Al content did not affect the final E_{corr} value. Both the AZ31 and AZ80

concluded the E_{corr} experiment with approximately equal E_{corr} values in both exposure environments. The final E_{corr} values in the pH = 14 environment were significantly lower than in the near-neutral environment.

4.1.2 E_{corr} Measurements – 48 Hours

E_{corr} curves for AZ31 and AZ80 in the near-neutral (pH ≈ 7), as well as the alkaline (pH = 14) ultrapure water exposure conditions are shown in Figure 4.2. These conditions were used for the STEM-EDS and ToF-SIMS examinations to study the naturally formed corrosion film structure in the absence of impurities.

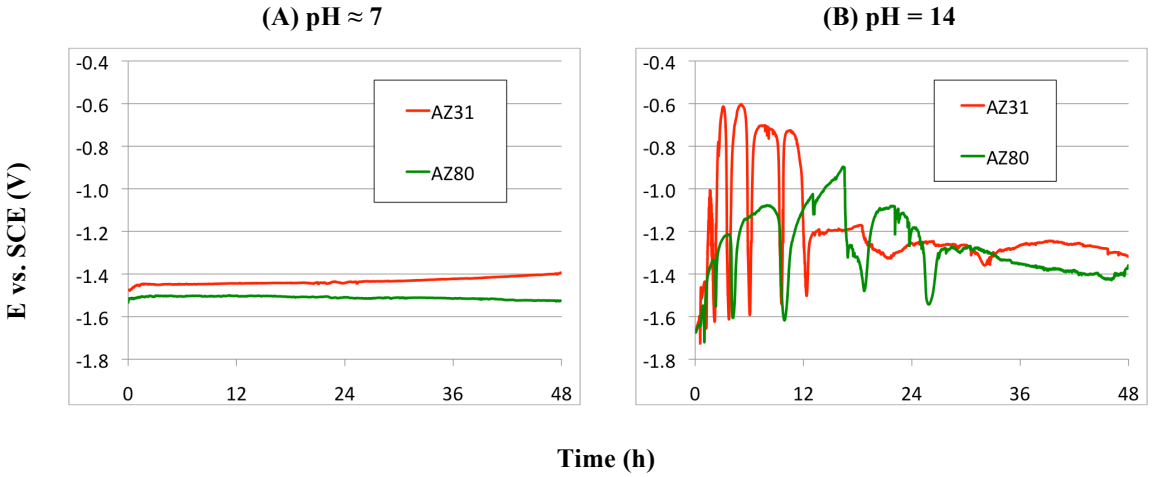

Figure 4.2: E_{corr} curves of AZ31 & AZ80 exposed to pure water for 48h in (A) near-neutral (pH ≈ 7) and (B) alkaline (pH = 14) environments.

In the near-neutral environment, the E_{corr} for both samples remained relatively stable throughout the 48-hour measurement. The E_{corr} of AZ31 was slightly ennobled with respect to AZ80. In contrast, severe oscillatory behaviour was witnessed in the alkaline pH 14 environment for both samples. This behaviour continued for approximately the first 24 hours and afterward, the E_{corr} of both samples became much more stable. Similar to the near-neutral exposures, the E_{corr} of AZ31 was slightly

ennobled with respect to AZ80. The final E_{corr} values in the alkaline environment were significantly nobler than the concluding E_{corr} values in the near-neutral environment.

4.1.3 Potentiodynamic Measurements

Potentiodynamic curves of 4N Mg, AZ31 and AZ80 are plotted in Figure 4.3 for the near-neutral (pH ≈ 7) and alkaline (pH = 14) 0.01 M NaCl environments.

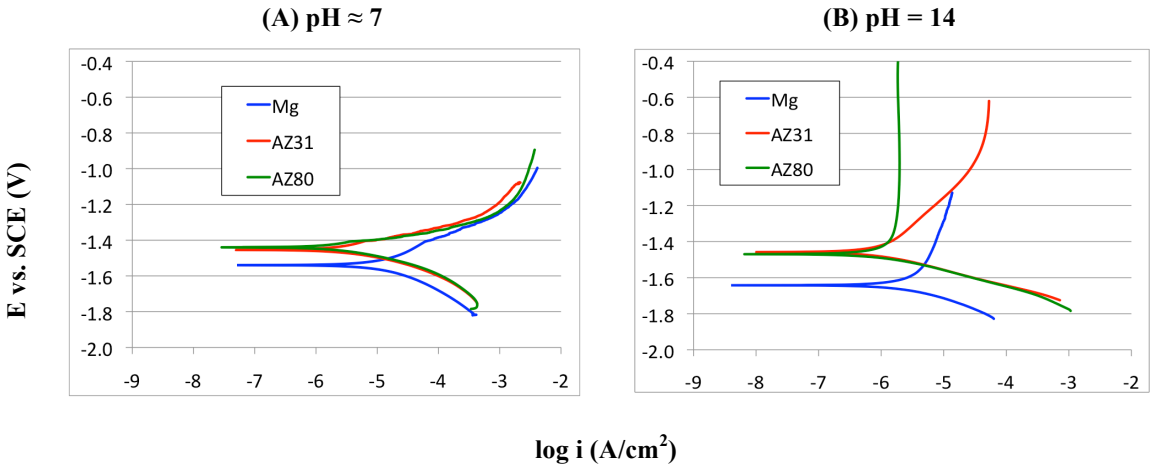

Figure 4.3: Potentiodynamic curves of 4N Mg, AZ31 & AZ80 exposed to 0.01 M NaCl solution in (A) near-neutral (pH ≈ 7) and (B) alkaline (pH = 14) environments.

In the near-neutral environment, little resistance to anodic polarization was witnessed, as pitting potentials were present at small anodic overpotentials for all three samples. Interestingly, regardless of the inherent microstructural differences, the breakdown potential for all three samples was identical at about -1.4 V_{SCE}. Despite the narrow regions of passivity present, the i_{corr} values for all three samples were actually quite low. E_{corr} values were slightly ennobled for AZ31 and AZ80 with respect to 4N Mg. Furthermore, the E_{corr} for all three samples was ennobled with respect to the concluding E_{corr} values of Figure 4.1. Alloyed Al content did not appear to affect the potentiodynamic behaviour of AZ31 or AZ80 as both curves seemingly overlapped each

other. In a similar fashion, the cathodic branches of AZ31 and AZ80 were essentially identical.

In contrast to the polarization curves for the near-neutral environment, significant corrosion resistance to anodic polarization was observed in the pH 14 environment. No pitting of the sample surface occurred on any of the three samples. Furthermore, anodic limiting current densities were present for all three samples; restricting anodically polarized corrosion rates to much lower levels than for the near-neutral environment. The anodic limiting current density on AZ80 was almost two orders of magnitude smaller than on AZ31. The i_{corr} values in the alkaline environment were slightly less than those of the near-neutral environment. Similar to the pH ≈ 7 environment, E_{corr} values for AZ31 and AZ80 were ennobled with respect to 4N Mg. In addition, the E_{corr} values were significantly ennobled compared with those of Figure 4.1. No differences were seen in the cathodic branch of the potentiodynamic curves for AZ31 and AZ80.

4.1.4 Surface Morphology (After Potentiodynamic Scans)

Representative pictures of the sample surface after the potentiodynamic scans for the near-neutral (pH ≈ 7) and alkaline (pH = 14) exposures are shown in Figure 4.4. Severe pitting was witnessed for all samples in the near-neutral environment, whereas the surface appeared relatively unaffected for the samples exposed to the alkaline environment. The severity of pitting increased with the magnitude of the current density attained on each sample.

(A) Pitted (pH ≈ 7) **(B) Not Pitted (pH = 14)**

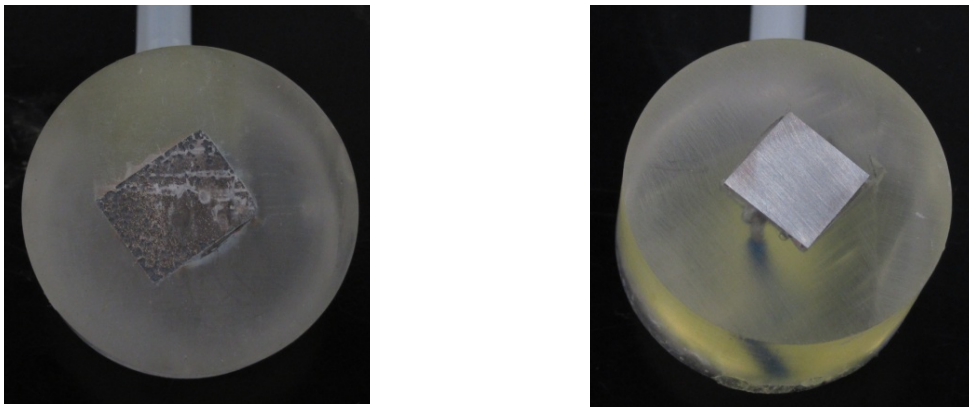

Figure 4.4: Characteristic surface appearance after potentiodynamic scans in 0.01 M NaCl solution in (A) near-neutral (pH ≈ 7) and (B) alkaline (pH = 14) environments.

4.1.4.1 Quantitative Potentiodynamic Analysis

Values of E_{corr}, i_{corr}, cathodic Tafel slope (β_c), cathodic exchange current density for the hydrogen evolution reaction ($i_{o,c}$), limiting current density (i_L), breakdown potential (E_b) and anodically polarized current density (i_a) have been calculated and are listed in Table 4.1. A sample polarization curve for each environment, with all parameters calculated, is shown in Figure 4.5. Adjustments to the standard redox potential of the hydrogen evolution reaction were made via the Nernst equation:

$$e_{H_2/H^+}(pH \approx 7) = e^{\circ}_{H_2/H^+} - 0.059\,pH = -0.413\,V_{SHE} = -0.172\,V_{SCE}$$

$$e_{H_2/H^+}(pH = 14) = e^{\circ}_{H_2/H^+} - 0.059\,pH = -0.826\,V_{SHE} = -0.585\,V_{SCE}$$

In the near-neutral environment, the calculated values of E_{corr}, i_{corr}, β_c and $i_{o,c}$ were very similar for AZ31 and AZ80. Consequently, their corrosion rates were essentially identical. The E_{corr} of the 4N Mg was much more active than the commercial AZ alloys and the corresponding corrosion parameters listed in Table 4.1 were also calculated to be much higher. In contrast, the E_b for all three samples were identical and the values of i_a

were very similar. Alloyed Al concentration did not appear to affect either of these two calculated parameters. Anodic limiting current densities were not observed until very high values of current density were achieved, and therefore, these current densities were not reported. By this time, the surfaces of all three samples were severely corroded.

Table 4.1: Quantitative analysis of potentiodynamic measurements on 4N Mg, AZ31 & AZ80 in 0.01 M NaCl solution in (A) near-neutral (pH ≈ 7) and (B) alkaline (pH = 14) environments.

Not Applicable

(A) pH ≈ 7

Sample	E_{corr} (V_{SCE})	i_{corr} (A/cm^2)	β_c (V/d)	$i_{o,c}$ (A/cm^2)	i_L ($\mu A/cm^2$)	E_b (V_{SCE})	i_a (A/cm^2)
Mg	-1.54	1.93E-5	0.200	3.00E-12	N/A*	-1.40	5.00E-3
AZ31	-1.45	7.60E-6	0.130	1.00E-15	N/A*	-1.40	4.00E-3
AZ80	-1.44	7.30E-6	0.140	7.00E-15	N/A*	-1.40	4.50E-3

(B) pH = 14

Sample	E_{corr} (V_{SCE})	i_{corr} (A/cm^2)	β_c (V/d)	$i_{o,c}$ (A/cm^2)	i_L ($\mu A/cm^2$)	E_b (V_{SCE})	i_a (A/cm^2)
Mg	-1.64	3.20E-6	0.130	2.00E-12	25.0	N/A*	2.50E-5
AZ31	-1.46	7.50E-7	0.088	9.00E-17	50.0	N/A*	3.50E-5
AZ80	-1.47	1.10E-6	0.091	2.00E-16	2.00	N/A*	2.00E-6

For the alkaline pH 14 environment, the calculated parameters were smaller for all three samples with respect to their values in the near-neutral environment. Again, AZ31 and AZ80 produced very similar results. The only significant difference was the value of anodic limiting current density where the current density was 25 times higher for AZ31 than it was for AZ80. The 4N Mg sample exhibited an anodic limiting current density, which was half the value of that of AZ31; however, its overall corrosion resistance, as determined by E_{corr}, i_{corr}, β_c and $i_{o,c}$, was still much lower than that of both AZ alloys. No E_b was observed on any of the three samples and i_a was essentially equal to i_L.

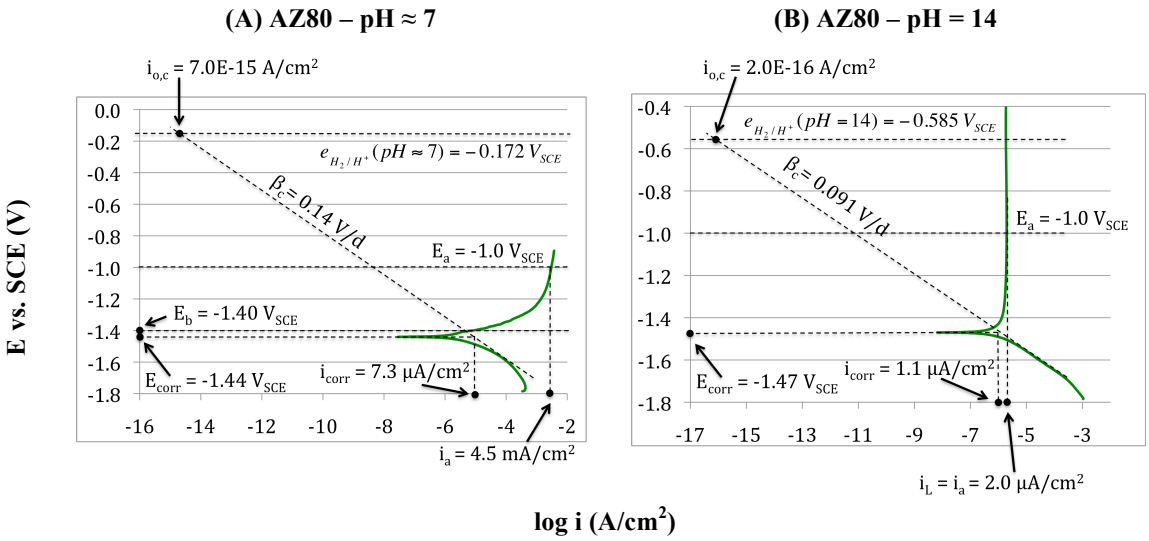

Figure 4.5: Quantified potentiodynamic curves of AZ80 alloy from the 0.01 M NaCl (A) near-neutral (pH ≈ 7) and (B) alkaline (pH = 14) environments.

4.1.5 LPR Measurements

LPR curves of the 4N Mg, AZ31 and AZ80 exposed to the near-neutral (pH ≈ 7) and alkaline (pH = 14) 0.01 M NaCl environments are shown in Figure 4.6. In the near-neutral environment, it was observed that AZ80, which had the highest nominal Al alloying concentration, had the lowest corrosion rate. AZ31 was next lowest and the 4N Mg sample, with no alloyed Al, had the highest corrosion rate. This was determined qualitatively by comparison of the slope of the LPR curve at zero net current.

For the alkaline pH 14 environment, three major differences were present with respect to the near-neutral exposure. First, the corrosion rates were much lower for all three samples. Second, AZ31 and AZ80 had nearly identical corrosion rates: dissimilar to the near-neutral exposure. Third, the shape of the LPR curves changed from essentially straight lines in the near-neutral environment to curved lines in the alkaline pH 14 environment.

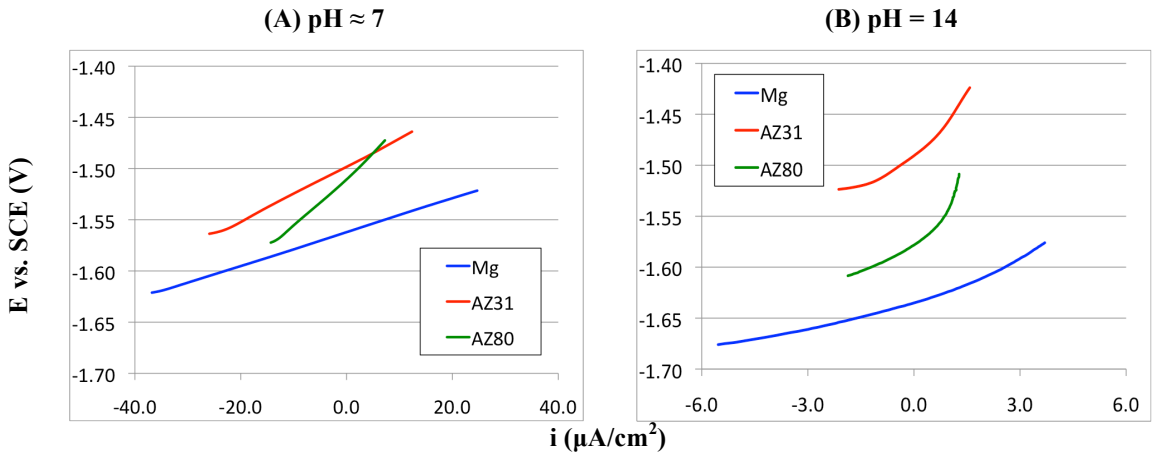

Figure 4.6: LPR curves of 4N Mg, AZ31 & AZ80 exposed to 0.01 M NaCl solution in (A) near-neutral (pH ≈ 7) and (B) alkaline (pH = 14) environments.

4.1.5.1 Quantitative LPR Measurements

R_p values were calculated using equivalent alloy weights and estimating $\beta_a = \beta_c =$ 0.12 V. The results of the LPR experiment are listed in Table 4.2. Similar to the potentiodynamic results, the corrosion resistance was superior in the pH 14 environment. Values of R_p increased dramatically and the resulting corrosion rates were decreased by an order of magnitude. AZ31 and AZ80 exhibited essentially identical R_p values, about half that of the 4N Mg sample.

For the near-neutral environment, AZ80 had the lowest R_p; about half that of AZ31. 4N Mg had the lowest R_p overall, and therefore, the highest corrosion rate. In both environments, the R_p of 4N Mg was approximately double that of the AZ alloys.

Table 4.2: Quantitative LPR analysis of commercial alloys.

Environment	Alloy	Equiv. Wt. (EW)	R_p (kΩ)
0.01 M NaCl (pH ≈ 7)	Mg	12.0	1.70
	AZ31	12.1	2.60
	AZ80	11.8	4.80
0.01 M NaCl (pH = 14)	Mg	12.0	10.1
	AZ31	12.1	25.7
	AZ80	11.8	22.4

The corrosion rates tabulated in Table 4.2 were achieved by fitting tangents to the LPR curves. Theses tangents were fitted by the Gamry Framework™ software package at the point of zero net current. An example of a fitted LPR curve is shown in Figure 4.7.

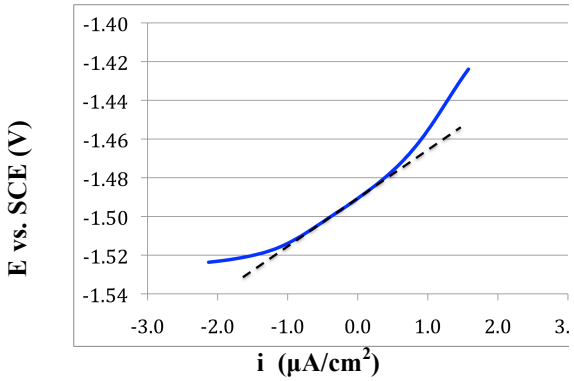

Figure 4.7: Fitted LPR curve of AZ31 in 0.01 M NaCl alkaline (pH = 14) environment using Gamry Framework™ software.

4.2 Electrochemical Measurements – Laboratory Alloys

4.2.1 E_{corr} Measurements

E_{corr} curves for the binary Mg-Al laboratory alloys exposed to the near-neutral (pH ≈ 7) and alkaline (pH = 14) 0.01 M NaCl environments are shown in Figure 4.8. For the near-neutral environment, it was observed that all binary alloys essentially concluded the E_{corr} experiment with a similar E_{corr} value; about 100 mV nobler than the 4N Mg sample. Consequently, there did not appear to be any trend regarding alloyed Al concentration.

Similarly, all binary alloys exposed to the alkaline pH 14 environment concluded the measurement with a similar E_{corr} value; about 50 mV nobler than the common, final E_{corr} value in the near-neutral environment. However, it was observed that a steady rise followed by a rapid fall in E_{corr} took place for the Mg-7Al and Mg-9Al. This behaviour was not present in the alloys with lower alloyed Al concentration. The difference in final

E_{corr} value between the binary alloys and 4N Mg increased to 250 mV from 100 mV in the near-neutral environment.

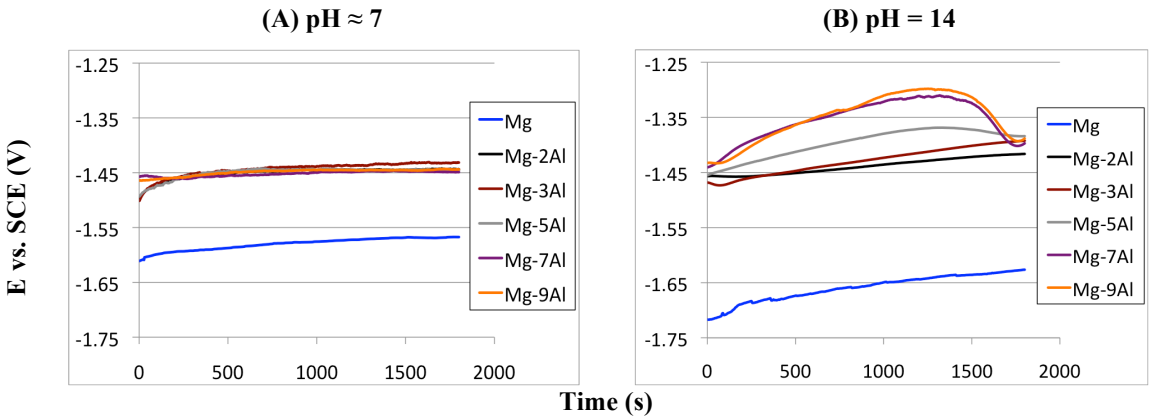

Figure 4.8: E_{corr} curves of binary Mg-Al alloys exposed to 0.01 M NaCl solution in (A) near-neutral (pH ≈ 7) and (B) alkaline (pH = 14) environments.

4.2.2 Potentiodynamic Measurements

Potentiodynamic curves for binary Mg-Al laboratory alloys exposed to the near-neutral (pH ≈ 7) and alkaline (pH = 14) 0.01 M NaCl environments are shown in Figure 4.9. In the near-neutral environment, no breakdown potentials were observed, as all laboratory alloys began pitting immediately upon anodic polarization. Severe corrosion occurred on the surface and large amounts of hydrogen gas were readily evolved. Alloyed Al content did not appear to significantly affect the potentiodynamic behaviour of the laboratory alloys in this environment. The only difference in polarization behaviour was the location of E_{corr}. For Mg-2Al and Mg-3Al, the E_{corr} value was slightly ennobled with respect to Mg-5Al, Mg-7Al and Mg-9Al. The cathodic branches of the potentiodynamic curves appeared to converge as cathodic overpotential increased to about 100 mV.

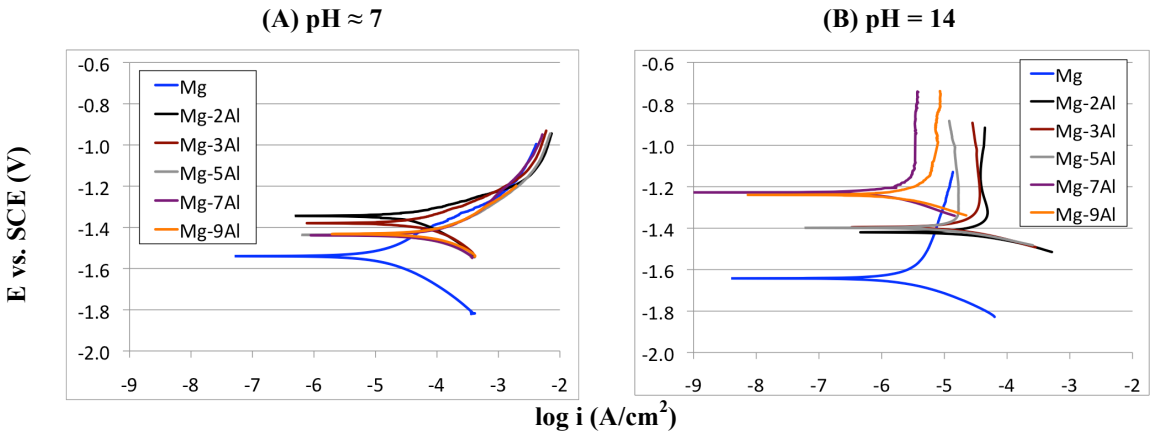

Figure 4.9: Potentiodynamic curves of binary Mg-Al alloys exposed to 0.01 M NaCl solution in (A) near-neutral (pH ≈ 7) and (B) alkaline (pH = 14) environments.

For the alkaline pH 14 environment, three major differences were noticed with respect to the near-neutral exposure. First, the E_{corr} values appeared to act in the reverse order. Mg-7Al and Mg-9Al exhibited ennobled E_{corr} values, whereas Mg-2Al and Mg-3Al showed this behaviour in the near-neutral environment. Second, significant corrosion resistance to anodic polarization was present for all laboratory alloys in the pH 14 environment. Anodic limiting current densities were observed for all alloys; reducing anodically polarized corrosion rates to much lower levels than in the near-neutral environment. The anodic limiting current density tended to decrease as the alloyed Al concentration increased. The limiting current density for 4N Mg appeared to fall in between the alloys of low and high-alloyed Al concentration. Finally, no pitting was observed on any of the binary alloys during the experiment.

4.2.3 Surface Morphology (After Potentiodynamic Scans)

Representative pictures of the sample surface after the potentiodynamic measurements for the near-neutral (pH ≈ 7) and alkaline (pH = 14) exposures are shown in Figure 4.10. Similar to the commercial alloys, severe pitting occurred on all alloys

exposed to the near-neutral environment whereas the samples exposed to the alkaline environment appeared unaffected. For the near-neutral environment, pitting began the instant anodic overpotential was applied.

(A) Pitted (pH ≈ 7) **(B) Not Pitted (pH = 14)**

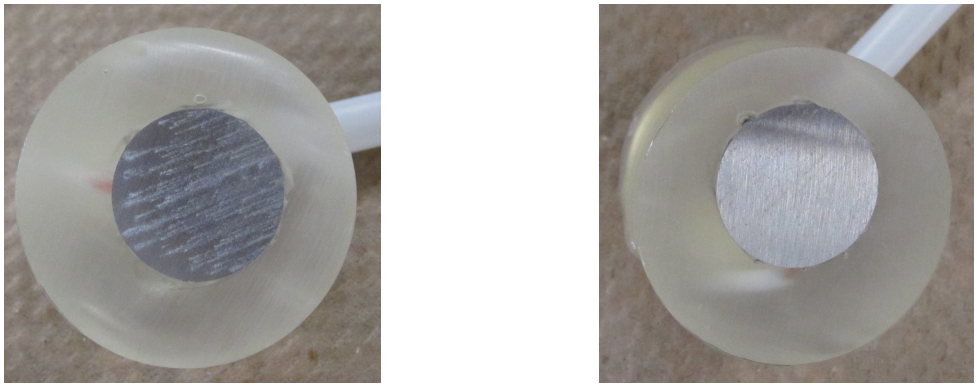

Figure 4.10: Characteristic surface appearance on Mg-Al alloys after potentiodynamic scans in 0.01 M NaCl solution in (A) near-neutral (pH ≈ 7) and (B) alkaline (pH = 14) environments.

4.2.3.1 Quantitative Potentiodynamic Analysis

Quantitative potentiodynamic parameters were calculated similar to the method outlined in Figure 4.5. Values for E_{corr}, i_{corr}, cathodic Tafel slope (β_c), exchange current density for the cathodic hydrogen evolution reaction ($i_{o,c}$) limiting current density (i_L) and anodically polarized current density (i_a) are listed in Table 4.3.

Corrosion performance was again far superior in the pH 14 alkaline environment. However, dissimilar trends were observed for the laboratory alloys in the near-neutral and alkaline exposures. In the near-neutral environment, the corrosion rates steadily increased as the alloyed Al concentration increased. The 4N Mg sample tested previously had the lowest corrosion rate overall. The E_{corr} of Mg-2Al and Mg-3Al were slightly ennobled with respect to Mg-5Al, Mg-7Al and Mg-9Al. Furthermore, their β_c and $i_{o,c}$ were also significantly higher than the higher alloyed Al alloys. No breakdown potentials

were witnessed for any binary Mg-Al sample as pitting occurred immediately upon anodic polarization. Values of i_a were extremely high and essentially identical amongst all of the samples.

Table 4.3: Quantitative analysis of potentiodynamic measurements on binary Mg-Al Alloys in 0.01 M NaCl solution in (A) near-neutral (pH ≈ 7) and (B) alkaline (pH = 14) environments.

Not Applicable

(A) pH ≈ 7

Sample	E_{corr} (V_{SCE})	i_{corr} (A/cm^2)	β_c (V/d)	$i_{o,c}$ (A/cm^2)	i_L ($\mu A/cm^2$)	E_b (V_{SCE})	i_a (A/cm^2)
Mg	-1.54	1.93E-5	0.200	3.00E-12	N/A*	N/A*	5.00E-3
Mg-2Al	-1.34	5.57E-5	0.220	3.00E-10	N/A*	N/A*	7.50E-3
Mg-3Al	-1.38	8.19E-5	0.210	1.00E-10	N/A*	N/A*	6.00E-3
Mg-5Al	-1.44	8.57E-5	0.160	1.00E-12	N/A*	N/A*	7.00E-3
Mg-7Al	-1.44	9.48E-5	0.170	3.00E-12	N/A*	N/A*	5.50E-3
Mg-9Al	-1.43	1.01E-4	0.160	1.00E-12	N/A*	N/A*	6.50E-3

(B) pH = 14

Sample	E_{corr} (V_{SCE})	i_{corr} (A/cm^2)	β_c (V/d)	$i_{o,c}$ (A/cm^2)	i_L ($\mu A/cm^2$)	E_b (V_{SCE})	i_a (A/cm^2)
Mg	-1.64	3.20E-6	0.130	2.00E-12	25.0	N/A*	2.50E-5
Mg-2Al	-1.42	3.89E-5	0.084	4.00E-15	50.0	N/A*	6.00E-5
Mg-3Al	-1.40	1.85E-5	0.081	2.00E-15	30.0	N/A*	5.00E-5
Mg-5Al	-1.40	1.41E-5	0.080	9.00E-16	15.0	N/A*	2.00E-5
Mg-7Al	-1.23	1.20E-6	0.100	4.00E-13	4.00	N/A*	4.00E-6
Mg-9Al	-1.24	2.00E-6	0.095	3.00E-13	7.00	N/A*	1.00E-5

For the alkaline environment, a reverse trend was observed. The corrosion rates generally improved as the alloyed Al concentration increased with the exception of Mg-9Al, whose rate was slightly higher than Mg-7Al. Furthermore, Mg-7Al and Mg-9Al had the highest values of $i_{o,c}$ and β_c. Values of i_L and i_a also decreased as the alloyed Al concentration increased. The anodic limiting current densities on Mg-7Al and Mg-9Al were about an order of magnitude smaller than on Mg-2Al and Mg-3Al. No E_b was observed for any sample.

4.3 STEM-EDS/FIB Analysis

4.3.1 FIB Results

Images representing the surface prior to the FIB milling process are shown in Figure 4.11. The 'AZ80 – pH 7' sample was only polished to 2400 SiC grit, and thus, a much rougher surface morphology was observed than for the samples polished to 4000 SiC grit. Residue, likely from the cleaning process, was present on all samples in the form of flaky deposits. Therefore, the area of interest was carefully selected away from these deposits. The 'AZ80 – pH 14' sample appeared to have the thinnest corrosion film of the three samples examined as evidenced by the cleanliness of the underlying substrate. Thick, corrosion products were observed on the 'AZ31 – pH 14' sample.

Cross-sectional images depicting the corrosion film thickness of all three samples are shown in Figure 4.12. Qualitative observations of the film thickness determined that the 'AZ80 – pH 14' specimen had the thinnest film followed by the 'AZ80 – pH 7' specimen and the 'AZ31 – pH 14' specimen. Furthermore, the 'AZ80 – pH 14' sample had the most uniform film thickness across the substrate surface. In contrast, the 'AZ80 – pH 7' sample had a highly irregular thickness profile.

(A) AZ80 – pH 7

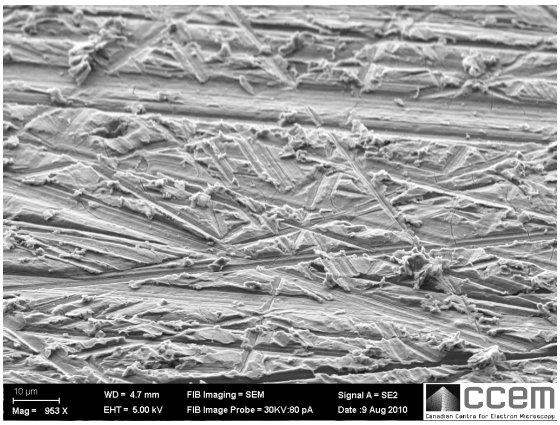

(B) AZ80 – pH 14

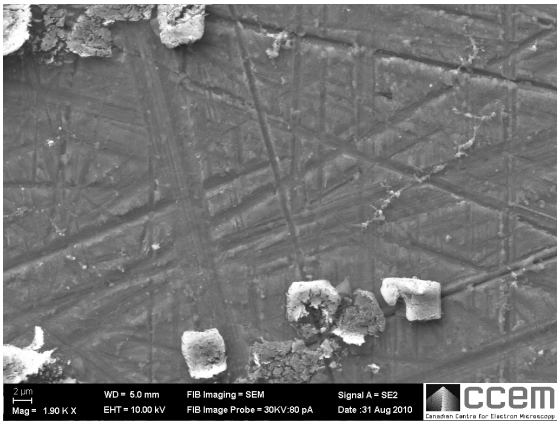

(C) AZ31 – pH 14

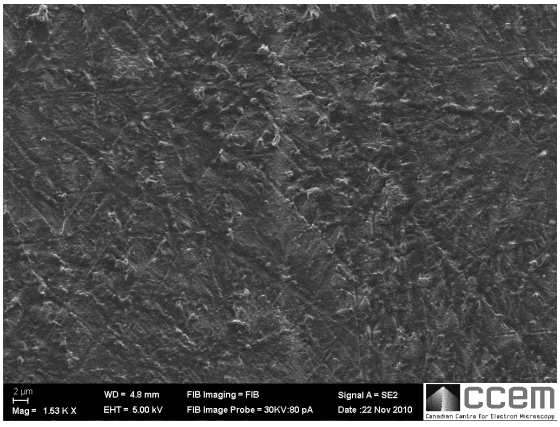

Figure 4.11: FIB/SEM images of sample surface prior to FIB milling of (A) AZ80 - pH 7, (B) AZ80 - pH 14 and (C) AZ31 - pH 14.

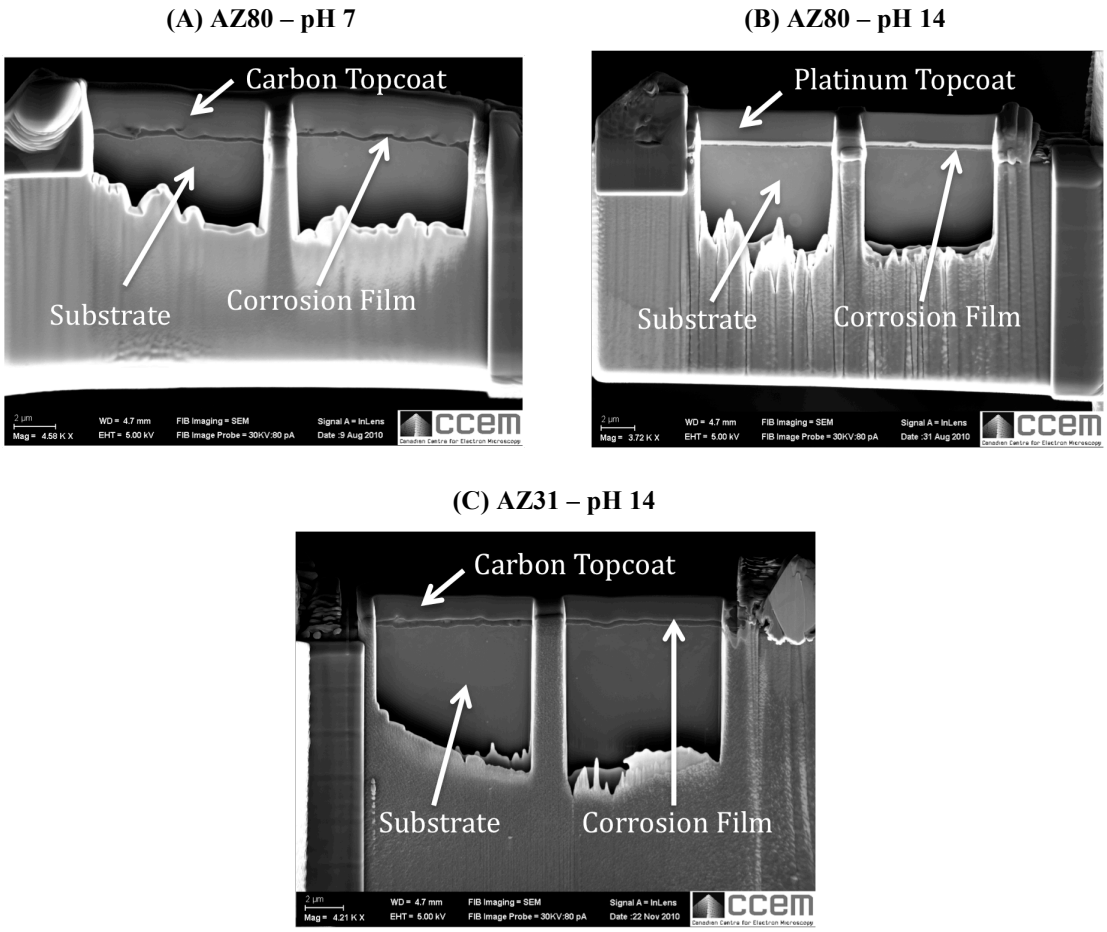

Figure 4.12: FIB/SEM images of cross-sectional FIB specimens after milling process of (A) AZ80 - pH 7, (B) AZ80 - pH 14 and (C) AZ31 - pH 14.

4.3.2 STEM Results

4.3.2.1 AZ80 – pH 7

The 'AZ80 – pH 7' sample was the first sample examined and did not use cryogenic cooling. Figure 4.13 shows low magnification images of the characteristic film structure. It was clearly observed that the film was non-uniform in thickness. Generally, the film appeared to be approximately 200 nm thick. Furthermore, the corrosion film incorporated at least two separate layers. The presence of a third layer at the outer interface of the corrosion film and carbon topcoat could not be identified qualitatively and required EDS analysis. Significant porosity was also observed throughout the corrosion

film. The highest degree of porosity was primarily located in the thickest layer of the film.

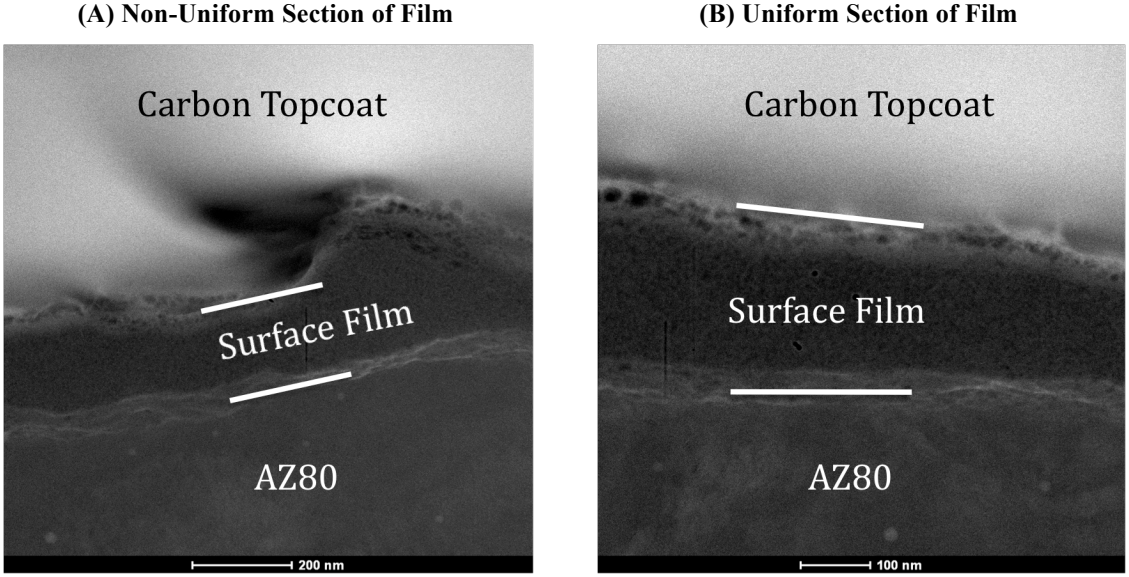

Figure 4.13: HAADF STEM images of the 'AZ80 - pH 7' surface film at (A) non-uniform section of the film and at (B) uniform section of the film.

High-resolution bright field TEM images were acquired and are shown in Figure 4.14. Unfortunately, once the TEM beam was focused at a high magnification over the specimen, significant beam irradiation damage occurred. New grains appeared to crystallize and evidence of a third layer of the corrosion film became apparent. Qualitative analysis of this damaged area was extremely difficult, and therefore, EDS was solely used for the characterization.

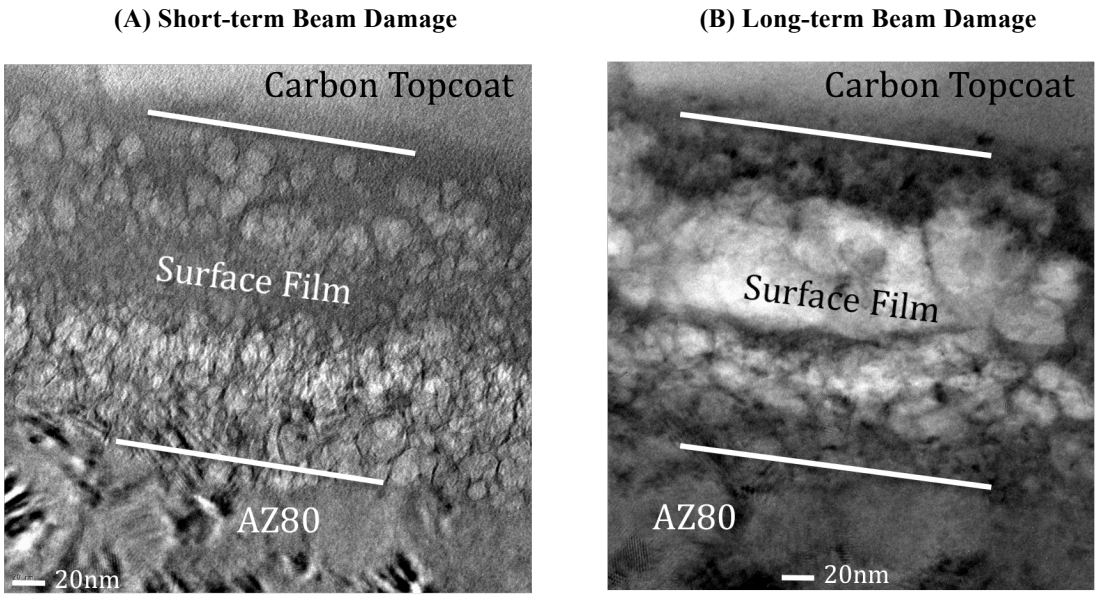

Figure 4.14: High resolution TEM bright field images of 'AZ80 - pH 7' surface film showing (A) short-term beam damage and (B) long-term beam damage.

4.3.2.2 AZ80 – pH 14

The second sample analyzed was 'AZ80 – pH 14' and this sample was cryogenically cooled, as well as coated with platinum (Pt). Pt was used in order to separate any contribution of carbon within the corrosion film from that of the carbon topcoat used in the 'AZ80 – pH 7 sample.' Characteristic images of the corrosion film are shown below in Figure 4.15. HAADF STEM images were difficult to analyze due to the extreme chemical contrast between Pt and Mg. The corrosion film was barely visible in HAADF mode, however it was clearly observed in the bright field operation mode. The film was uniform in thickness and quite compact measuring approximately 100 nm in thickness. In addition, the film contained two distinct layers: a thin inner layer and a thick outer layer as seen in Figure 4.15B.

(A) HAADF STEM Image **(B) Bright Field TEM Image**

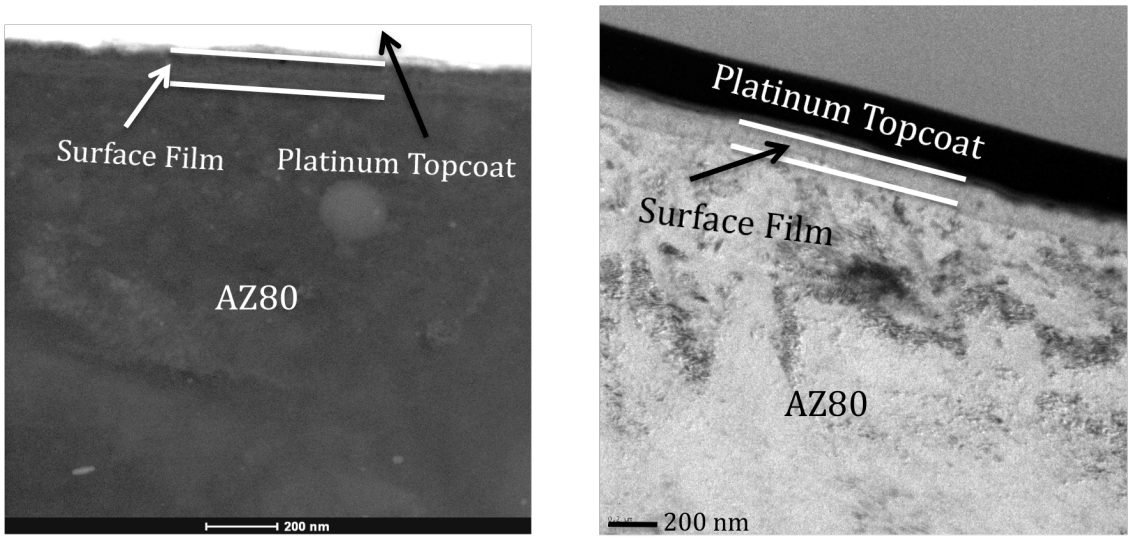

Figure 4.15: Characterisitc images of the 'AZ80 - pH 14' surface film using a (A) HAADF STEM image and a (B) bright field TEM image.

High-resolution bright field TEM images were taken to investigate the structure of the two-layer corrosion film in greater detail. These images are shown below in Figure 4.16. The interface between the substrate and corrosion film appeared to be relatively rough in morphology. Furthermore, no bands of atomic planes were readily observed for this inner layer. In contrast, the outer layer exhibited clear bands of atomic planes in certain areas suggesting the layer was at least partly crystalline. No further significant information was found at higher magnifications.

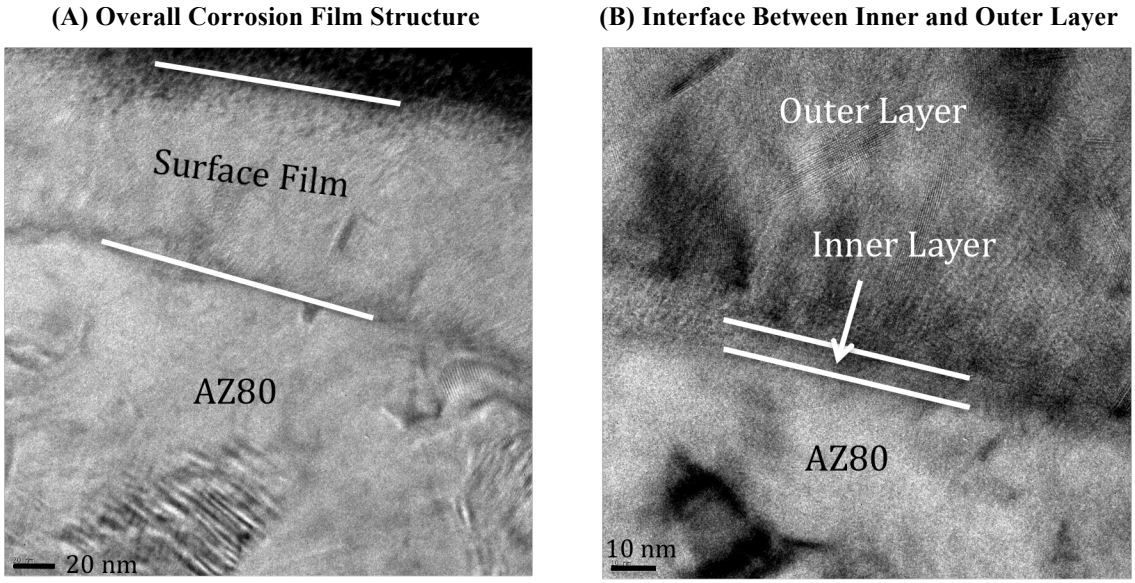

Figure 4.16: High resolution TEM bright field images of the 'AZ80 - pH 14' surface film, showing the (A) overall corrosion film structure and the (B) interface between the inner and outer layer of the film.

4.3.2.3 AZ31 – pH 14

The final sample analyzed was 'AZ31 – pH 14.' This specimen was cryogenically cooled and utilized a carbon topcoat in order to obtain high quality HAADF images. Characteristic images of the film structure are shown below in Figure 4.17. Similar to the 'AZ80 – pH 14' sample, a clear two-layer corrosion film was observed with a relatively uniform thickness of approximately 300 nm. The inner layer was thin and compact, whereas the outer layer was thick and porous. Bright contrast was observed at the location of the inner layer and the porosity of the outer layer was clearly evident in the form of dark voids. A rough, weaving pattern was also witnessed for the structure of the inner layer. High magnification HAADF images were taken to examine the structure of the inner layer, as well as the extent of porosity in the outer layer. These images are shown in Figure 4.18. The inner layer clearly showed a weaving pattern with bright contrast. However, the contrast was not observed throughout the full layer signifying the

properties of the film were not uniform. The porosity in the outer layer was extensive and increased toward the exterior of the corrosion film.

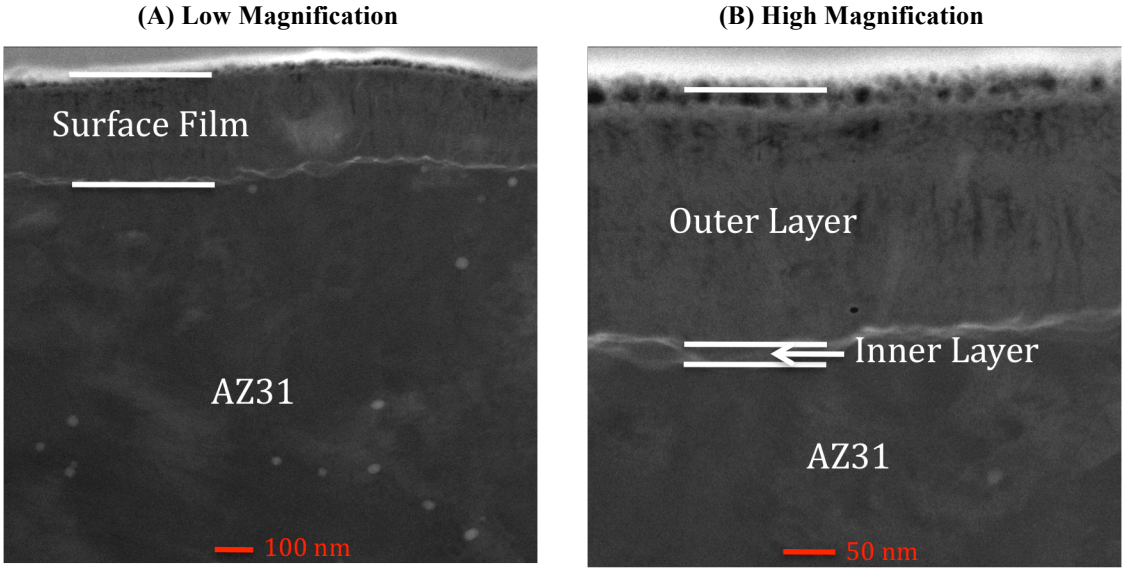

Figure 4.17: HAADF STEM images of the 'AZ31 - pH 14' surface film at (A) low magnification and (B) high magnification.

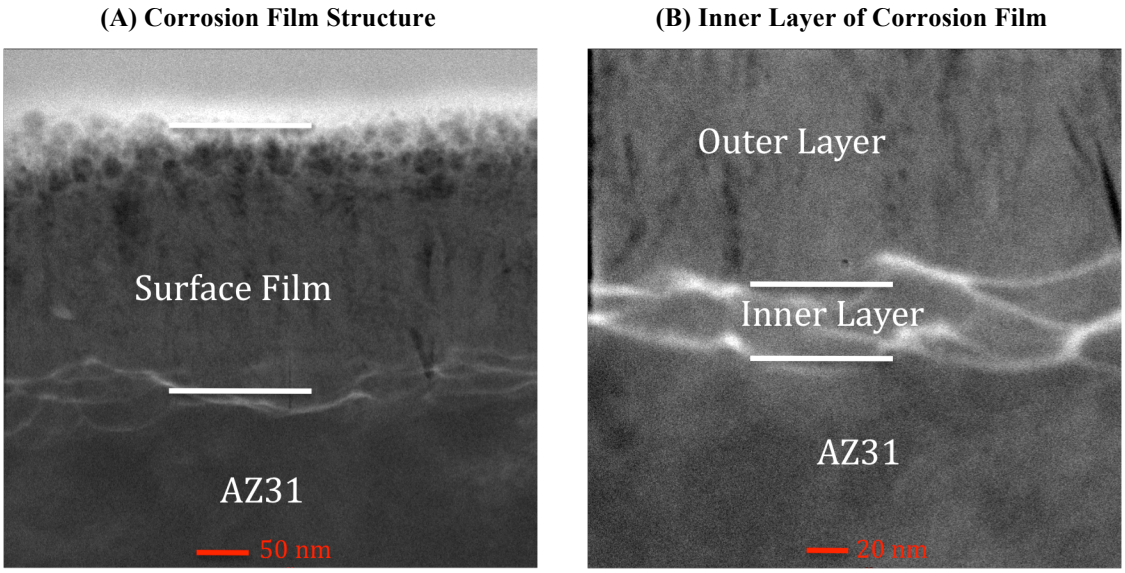

Figure 4.18: HAADF STEM images of 'AZ31 - pH 14' showing the (A) overall surface film structure and the (B) inner layer of the film.

4.3.3 EDS Results

4.3.3.1 AZ80 – pH 7

EDS point spectra of intermetallic particles were acquired prior to SmartMapping™. Figure 4.19 shows an HAADF STEM image, as well as the accompanying EDS spectra of both an AlMn intermetallic particle and the surrounding matrix phase. No Mn was detected in the solid solution matrix phase. The Cu contribution to the EDS spectra was from the Cu grid the TEM specimen was placed on to protect the sample from charging effects.

(A) AZ80 – pH 7: AlMn Particle **(B) AZ80 – pH 7: Matrix Phase**

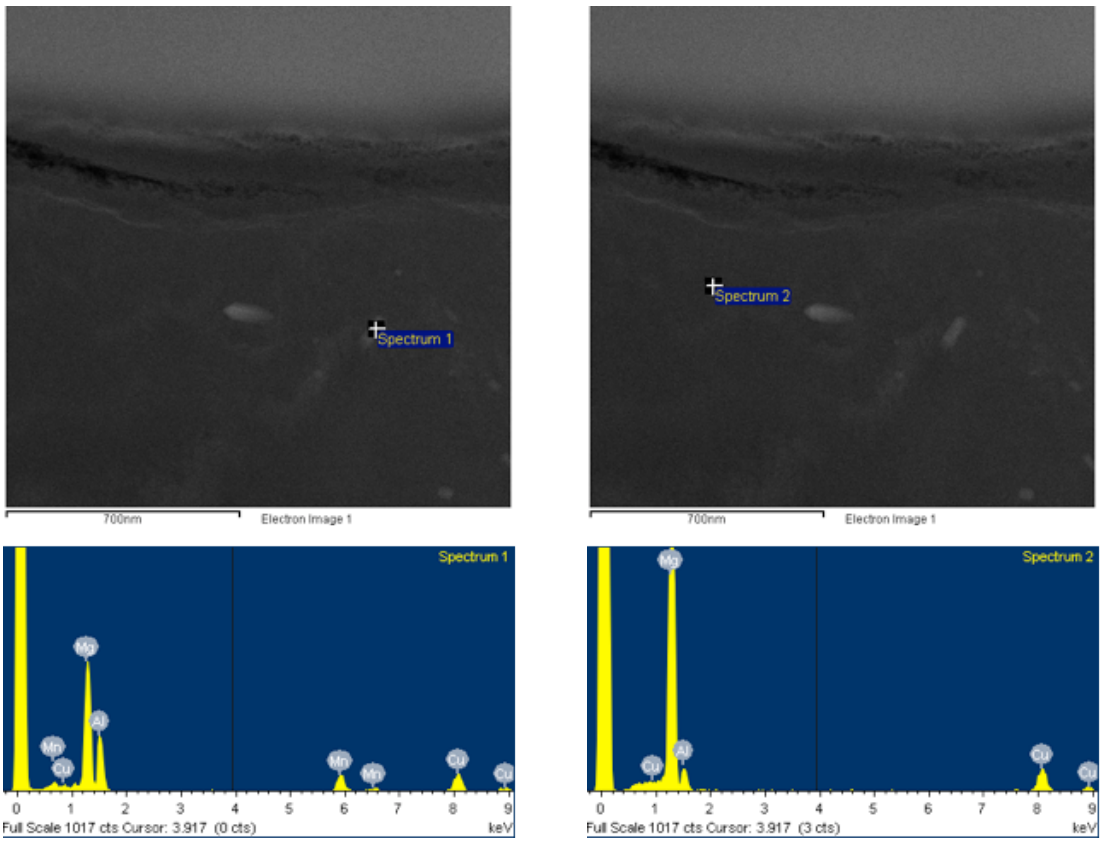

Figure 4.19: HAADF STEM image & EDS spectrum of an 'AZ80 - pH 7' (A) AlMn intermetallic particle and the (B) matrix phase.

Preliminary attempts at acquiring point scan EDS spectra of the corrosion film are shown in Figure 4.20. The porous outer layer of the film was so sensitive to beam irradiation that no spectra could be acquired. Only the signal from the Cu grid was found. In contrast, EDS spectra were able to be collected for the denser inner layer of the corrosion film.

(A) AZ80 – pH 7: Inner Layer **(B) AZ80 – pH 7: Outer Layer**

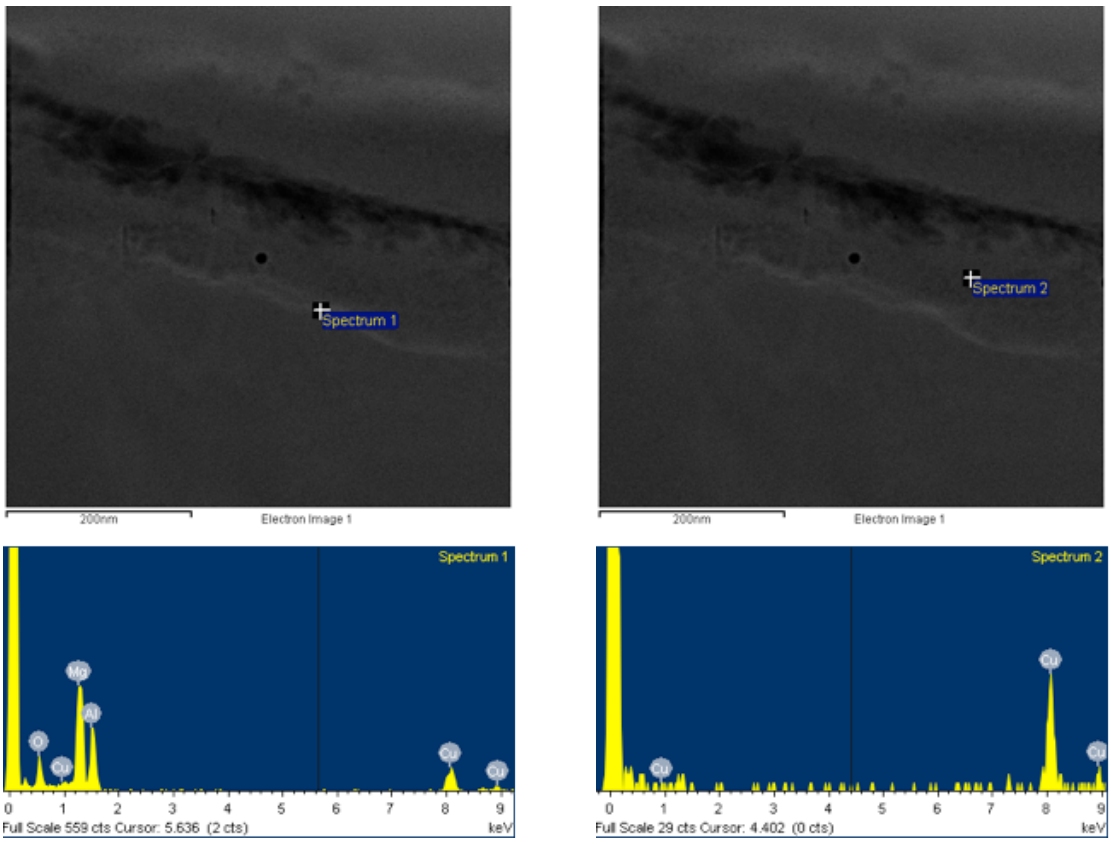

Figure 4.20: HAADF STEM image & EDS spectrum of the 'AZ80 - pH 7' (A) inner layer and (B) outer layer of the surface film.

A characteristic section of the corrosion film was identified and is shown in Figure 4.21. The corresponding SmartMap™ of the corrosion film was acquired and is displayed in Figure 4.22. Two distinct interfaces can be seen from the SmartMap™. First, the interface between the carbon topcoat and the outer porous layer was evident

from the O and C elemental pixel maps. Second, the dense inner layer or interface between the substrate and the porous outer layer was observed by examining the Mg and O pixel maps. Furthermore, it appeared that the Al concentration was higher in the film region than in the substrate. Zn concentration was diversely scattered in minute amounts throughout the SmartMap™. Similarly, Ga concentration from the FIB milling process was also distributed evenly throughout the film and no accumulation was observed.

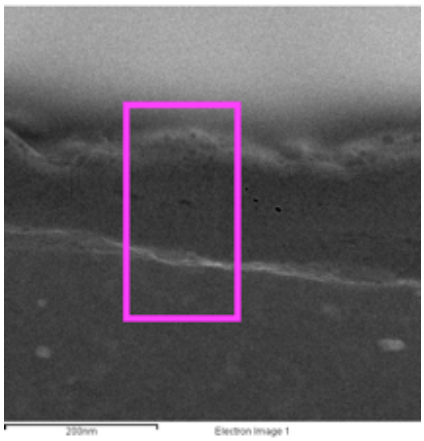

Figure 4.21: HAADF STEM image of the 'AZ80 – pH 7' site of interest for SmartMap™ 1.

To further process the data and obtain a clearer view regarding the structure, composition and thickness of the corrosion film, three characteristic regions of (Mg + Al) : O ratio were developed. 'Region 1' included (Mg + Al) : O ratios of approximately 0.5 and was indicative of an Al enriched $Mg(OH)_2$ phase at the exterior of the surface film. 'Region 2' was related to the inner barrier layer of the corrosion film and incorporated (Mg + Al) : O ratios of approximately 1; representing an Al enriched MgO structure. Finally, 'Region 3' was characteristic of the AZ alloy substrate and included (Mg + Al) : O ratios much greater than 1.

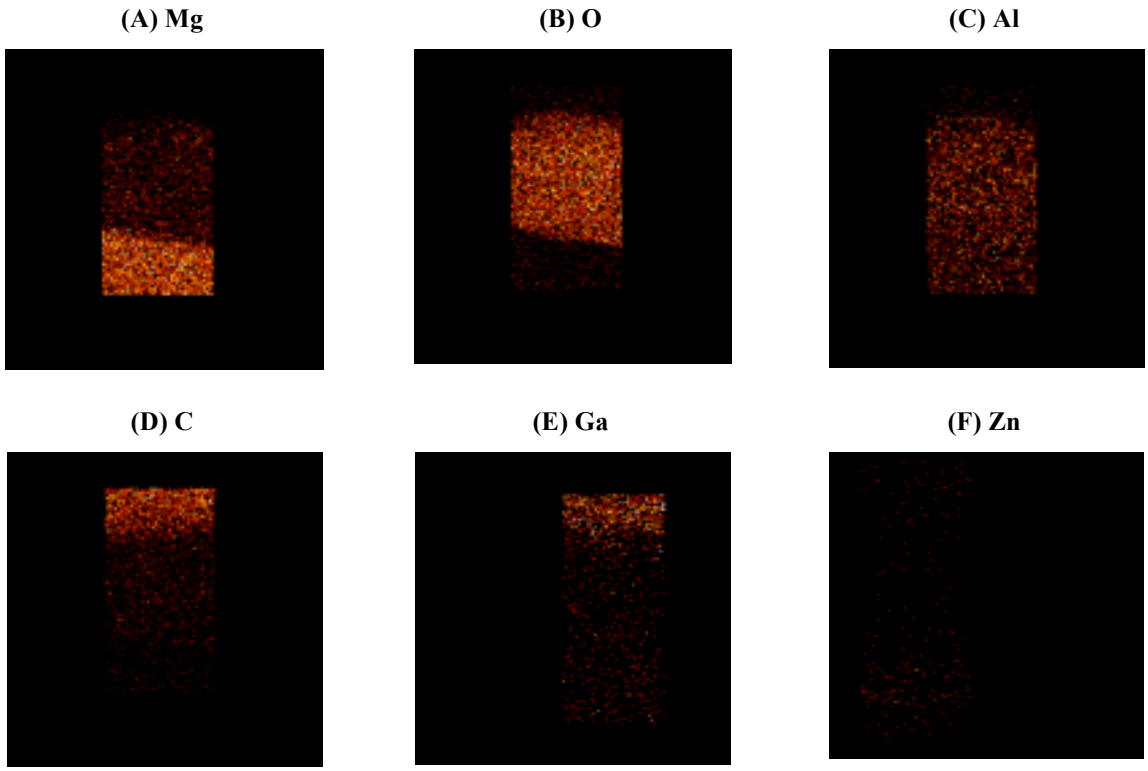

Figure 4.22: SmartMap™ 1 elemental maps of (A) Mg (B) O (C) Al (D) C (E) Ga (F) Zn for 'AZ80 – pH 7.'

The individual spectra used to quantify SmartMap™ 1 are shown in Figure 4.23. Sites of interest were chosen in approximately 25 nm intervals from the surface of the film. The corrosion film on the 'AZ80 – pH 7' sample was highly irregular in thickness. It was much thicker on the right side of the analyzed region in Figure 4.23, and thus, depth adjustments were performed manually to correct for this inconsistency.

A scatter plot for the 'AZ80 – pH 7' sample is shown in Figure 4.24 with each point representing an average atomic concentration value of Mg, Al or O for each set of spectra obtained at a certain depth from the surface. Error bars represent one standard deviation on each side of the average value. Considerable scatter was present, specifically in 'Region 2', however the three distinctive regions could be identified from

the plot. 'Region 1' was estimated to be about 160 nm thick. 'Region 2' was approximately 40 nm thick and 'Region 3' was estimated to begin at about 200 nm from the surface.

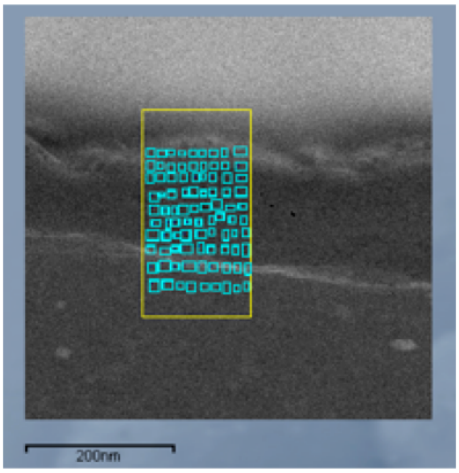

Figure 4.23: Setup for Inca™ quantification of SmartMap™ 1 on 'AZ80 – pH 7.'

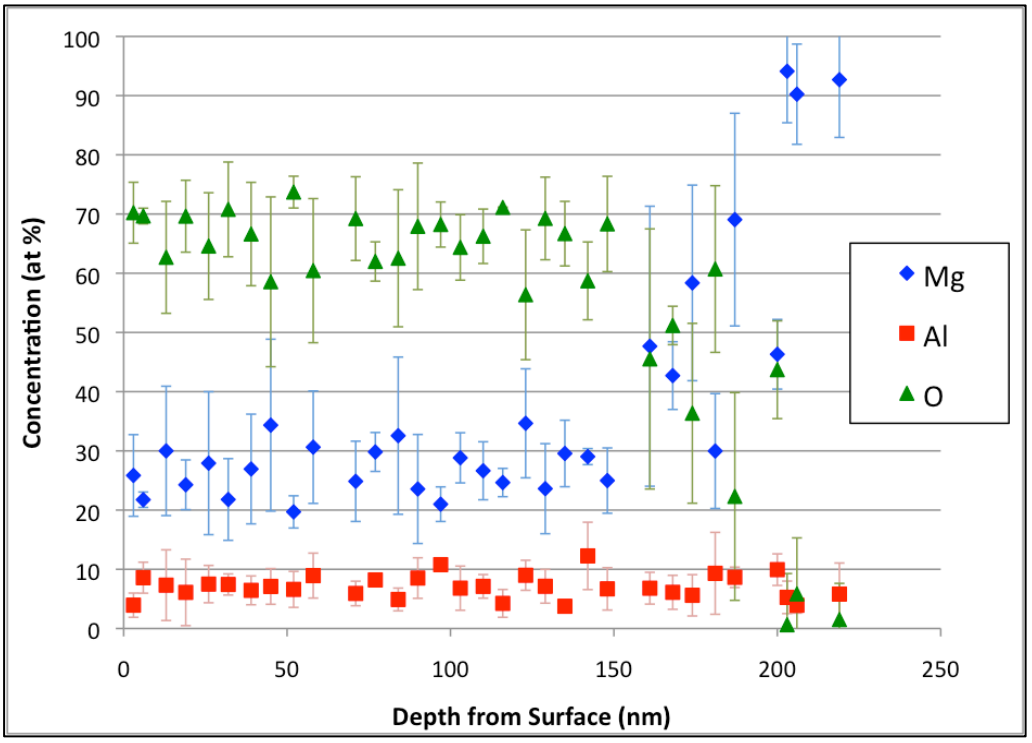

Figure 4.24: Scatter plot of Mg/Al/O concentrations from Inca™ quantitative SmartMap™ analysis of 'AZ80 – pH 7.'

Average atomic concentration values of Mg, Al and O were calculated for each respective region and are listed in Table 4.4. The (Mg + Al) : O ratio for the outer and inner layers was 0.51 and 1.3 respectively. At a depth of 200 nm, the quantified EDS spectra were clearly attributable to the AZ alloy substrate. Concentration of Al was higher in the surface film than in the alloy substrate.

Table 4.4: (Mg + Al) : O ratio and average concentration value (at%) of Mg/O/Al in surface film at various depths on 'AZ80 – pH 7.'

	Average At% Value				
Depth (nm)	**Mg**	**Al**	**O**	**(Mg + Al) : O Ratio**	**Predominant Phase**
0-160	27	7.0	66	0.51	$Mg(OH)_2$
161-200	49	8.0	43	1.3	$MgO + Mg(OH)_2$
201+	92	5.0	3.0	>> 1	AZ80 Substrate

A bounded scatter plot including the three regions of different (Mg + Al) : O atomic ratio is shown in Figure 4.25. The outer layer exhibited relatively consistent behaviour, while the inner layer produced significantly more scattered concentration values, which made identification of the inner barrier layer more difficult. It appeared from the acquired TEM images and the resulting EDS analysis, that the inner layer had suffered significant breakdown in its structure and this caused the atomic concentration values to vary so sizably.

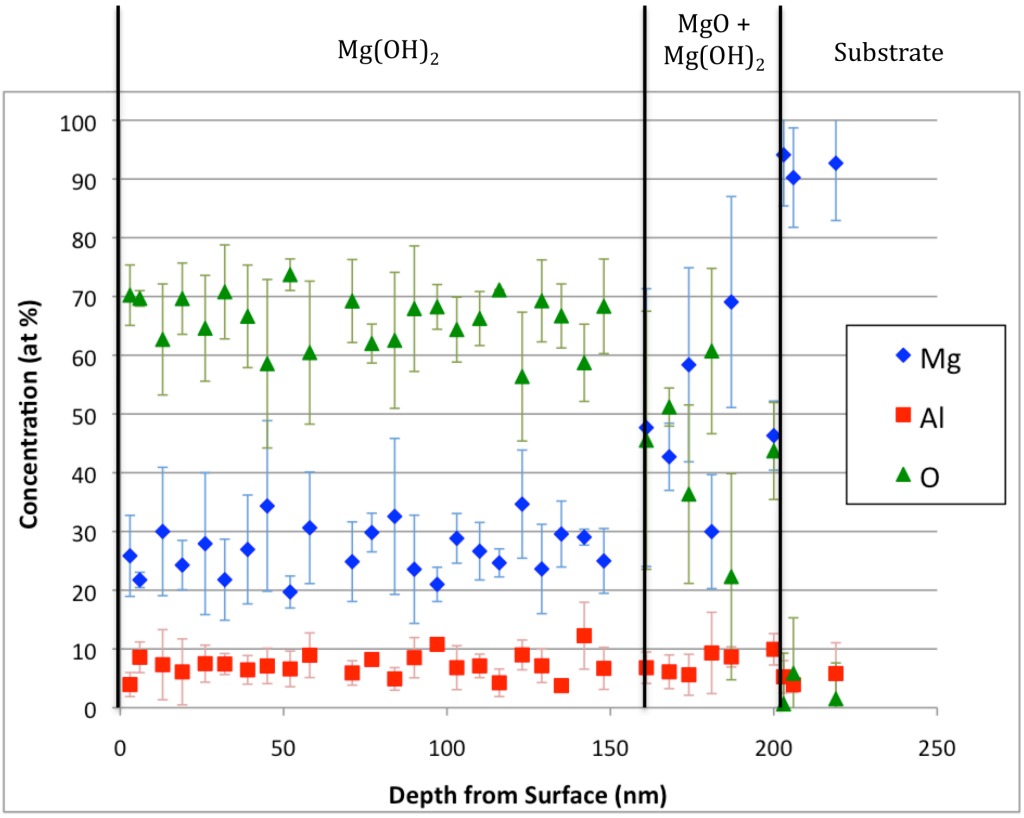

Figure 4.25: Approximated surface film structure of 'AZ80 - pH 7.'

4.3.3.2 AZ80 – pH 14

EDS point spectra of intermetallic particles, as well as the matrix phase, were acquired prior to the SmartMapping™ process. Figure 4.26 shows an HAADF STEM image, as well as the accompanying EDS spectra, of both an AlMn and likely β intermetallic particle. The β particle was considerably larger in size than the AlMn particle.

(A) AZ80 – pH 14: AlMn Particle **(B) AZ80 – pH 14: Possible (β) Particle**

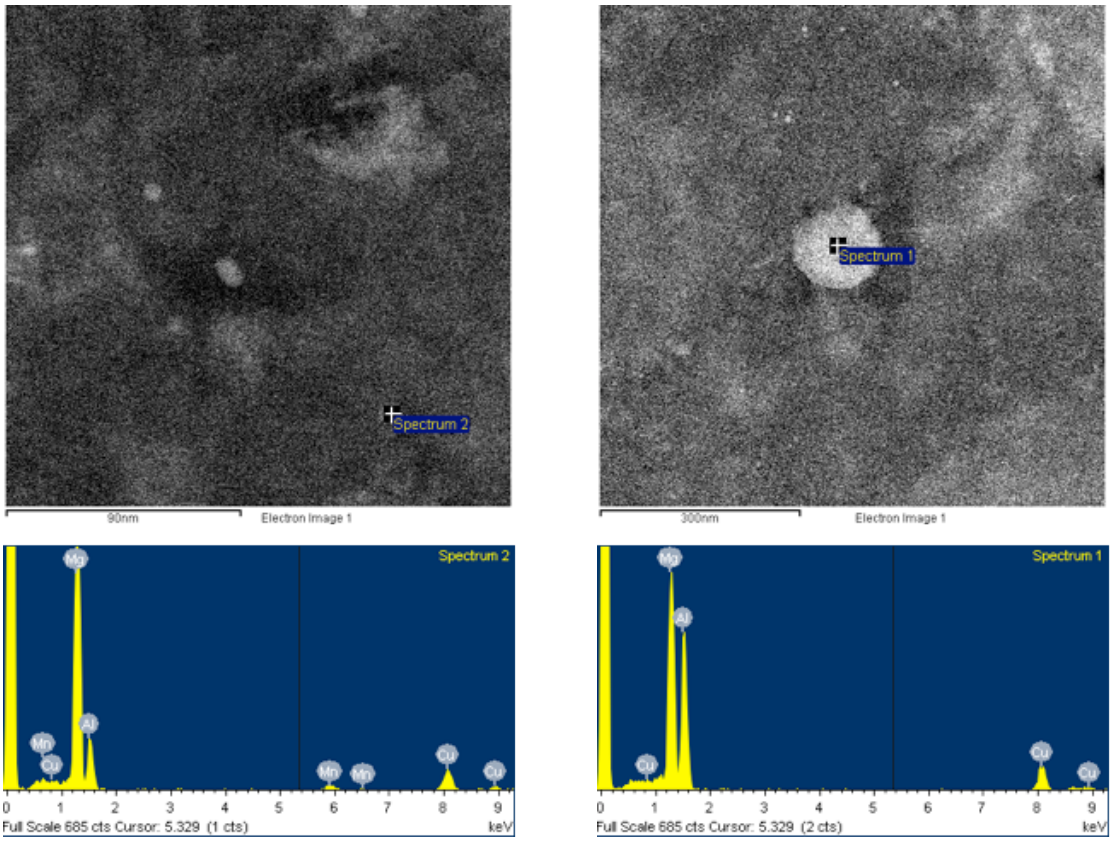

Figure 4.26: HAADF STEM image & EDS spectrum of an 'AZ80 - pH 14' (A) AlMn intermetallic particle and a (B) likely β intermetallic particle.

Figure 4.27 shows another likely region associated with the β phase, as well as, the surrounding matrix phase of the 'AZ80 – pH 14' sample for comparison. Significantly less Al content was present within the matrix phase, as observed by the shorter Al peak of the EDS spectrum. As with the 'AZ80 – pH 7' sample, no Mn was detected in the solid solution matrix phase. The Cu peaks of the EDS spectra were again due to the Cu grid the TEM specimen was placed on.

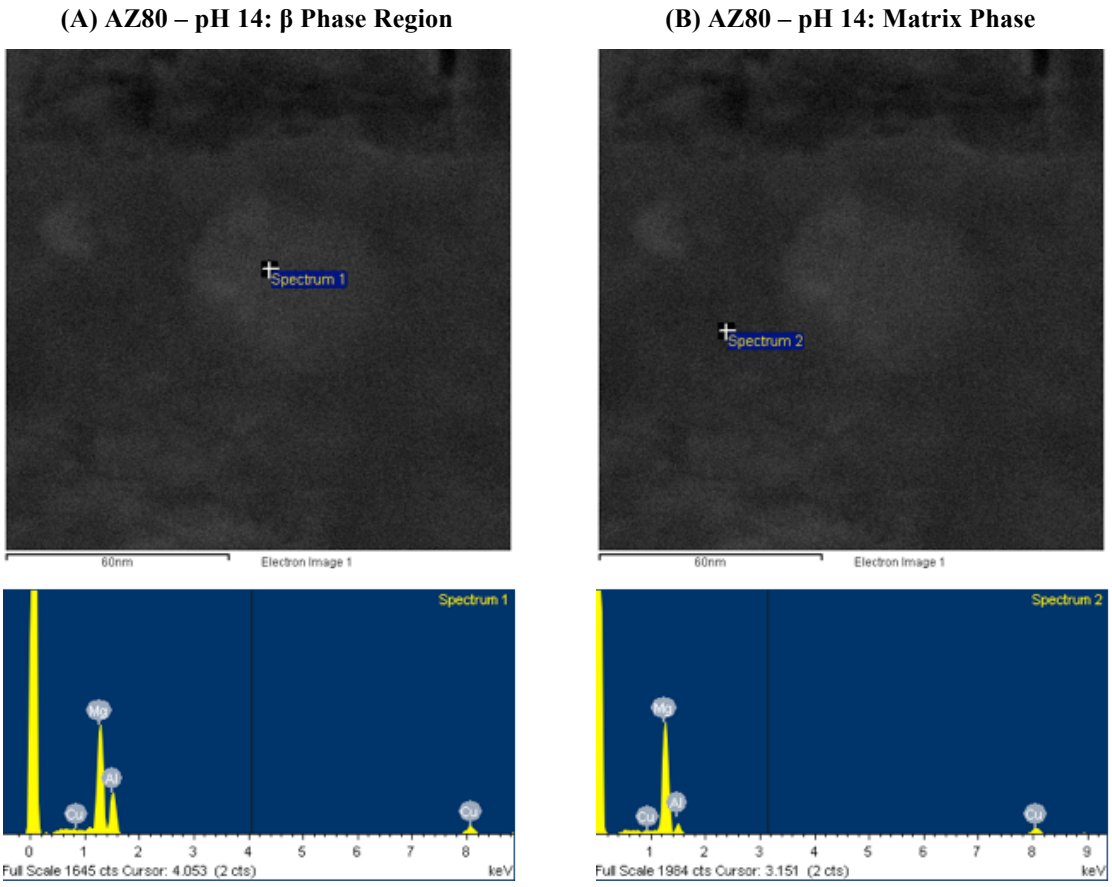

Figure 4.27: HAADF STEM image & EDS spectrum of the 'AZ80 – pH 14' (A) β phase and (B) matrix phase.

A characteristic section of the 'AZ80 – pH 14' corrosion film was selected and is shown in Figure 4.28. Due to the high chemical contrast between the Pt topcoat and the corrosion film itself, the boundaries of the film layers were difficult to identify qualitatively. The corresponding SmartMap™ of the corrosion film, shown in Figure 4.28, was acquired and is displayed in Figure 4.29. A bi-layer structure was easily identified through a similar procedure to 'AZ80 – pH 7'. The corrosion film appeared non-uniform in thickness as observed by the elemental pixel maps. Depletion of Al was observed in the film region with respect to the substrate. Generally, C was found at the

exterior of the corrosion film and uniformly distributed throughout the porous outer layer. Accumulation of Pt and Ga were both observed above the corrosion film with only slight amounts within the interior.

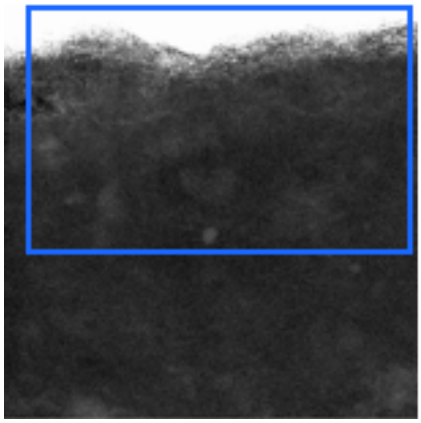

Figure 4.28: HAADF STEM image of the 'AZ80 – pH 14' site of interest for SmartMap™ 1.

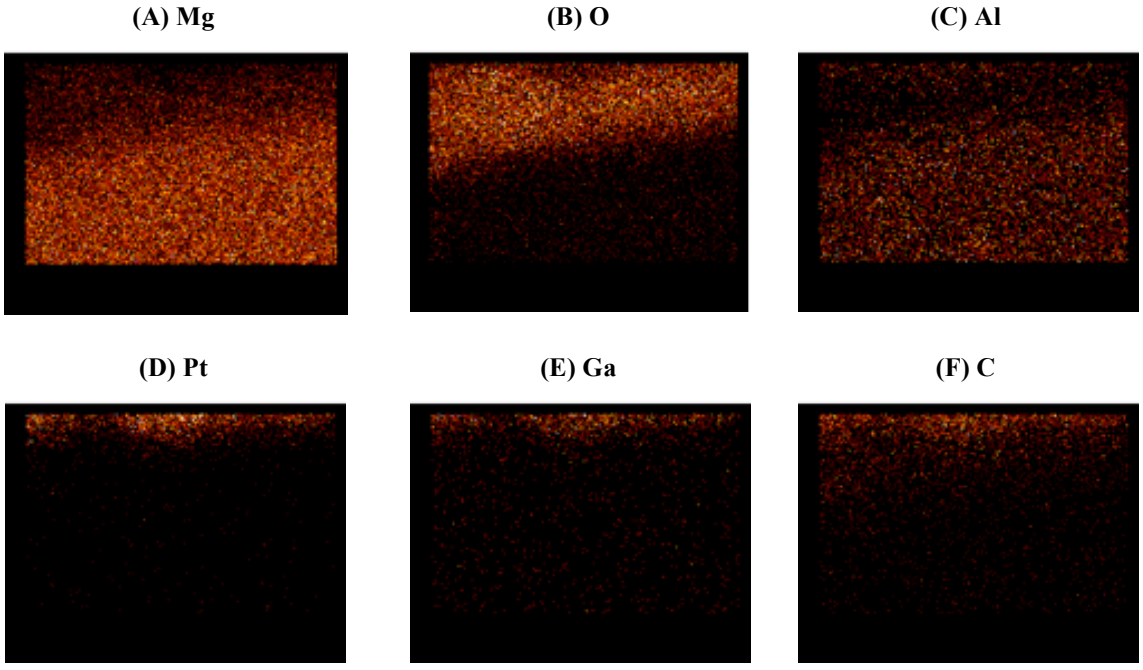

Figure 4.29: SmartMap™ 1 elemental maps of (A) Mg (B) O (C) Al (D) Pt (E) Ga (F) C on 'AZ80 – pH 14.'

Individual EDS spectra used to quantify SmartMap™ 1 are shown in Figure 4.30. Sites of interest were chosen in approximately 25 nm intervals from the surface of the

film. Preliminary EDS spectra were quantified to estimate the uniformity of the film thickness. This step was required for this sample due to the difficulty in visualizing the film, as a result of the high chemical contrast between the sample and the Pt topcoat. The thickness of the film was found to be slightly thicker on the left side of Figure 4.30 than on the right. Adjustments were performed manually to correct for this discrepancy.

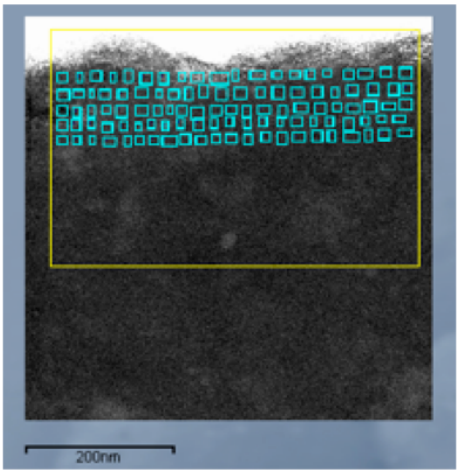

Figure 4.30: Setup for Inca™ quantification of SmartMap™ 1 on 'AZ80 – pH 14.'

The scatter plot produced for 'AZ80 – pH 14' is shown in Figure 4.31 with each point representing an average atomic concentration of Mg, Al or O for each individual set of spectra at the give depth. Similar to the prior AZ80 sample, the (Mg + Al) : O ratios were investigated and fit into characteristic regions. Significant scatter was present, however, the three distinctive regions could again be ascertained. 'Region 1' was estimated to be about 55 nm thick. 'Region 2' was approximately 40 nm thick and 'Region 3' was estimated to begin at about 95 nm from the surface.

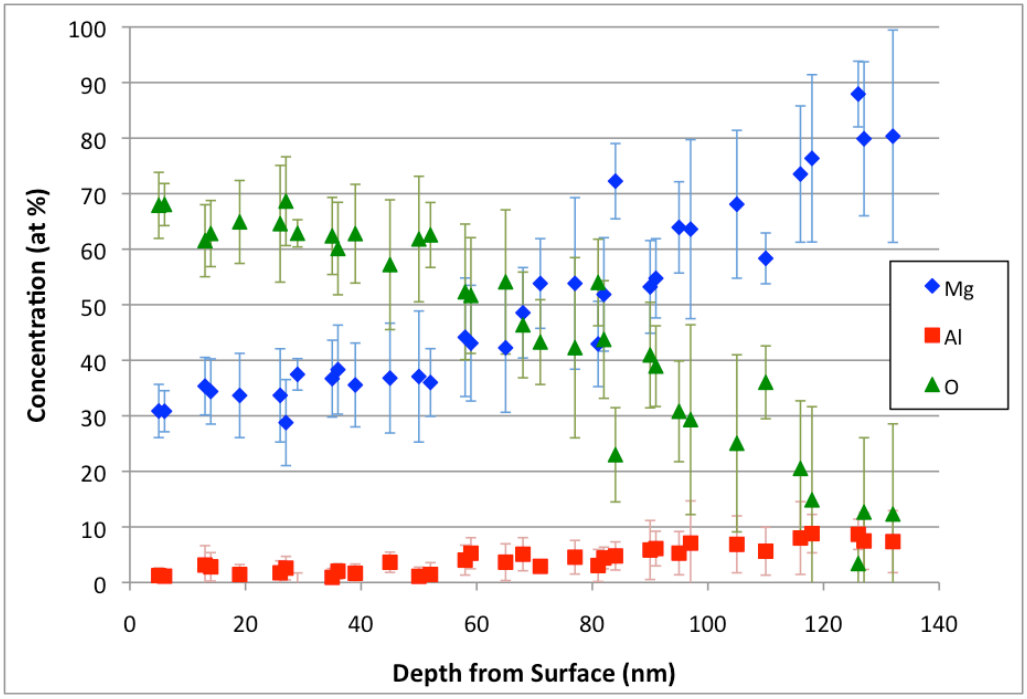

Figure 4.31: Scatter plot of Mg/Al/O concentrations from Inca™ quantitative SmartMap™ analysis on 'AZ80 – pH 14.'

The average atomic concentration values of Mg, Al and O were calculated for Regions 1 - 3. These values are listed in Table 4.5. For the 'AZ80 – pH 14' sample, the outer layer (Mg + Al) : O ratio was 0.59 and the inner layer ratio was 1.2. 'Region 3' still contained a fair amount of O at the interface, however this quickly dissipated at about 120 nm from the surface. Al concentration was much higher in the substrate than in the corrosion film. However, despite this deficiency in Al, the corrosion film was half the thickness of the 'AZ80 – pH 7 sample.'

Table 4.5: (Mg + Al) : O ratio and average concentration value (at%) of Mg/O/Al in surface film at various depths on 'AZ80 – pH 14.'

	Average at% Value				
Depth (nm)	**Mg**	**Al**	**O**	**(Mg + Al) : O Ratio**	**Predominant Phase**
0-55	35	2.0	63	0.59	$Mg(OH)_2$
56-94	51	5.0	45	1.2	MgO
95+	72	7.0	21	>> 1	AZ80 Substrate

The bounded scatter plot including the three regions of different (Mg + Al) : O atomic ratio for the 'AZ80 – pH 14' sample is shown in Figure 4.32. While significant scatter was present in the analysis, a clear bi-layer corrosion film structure was observed.

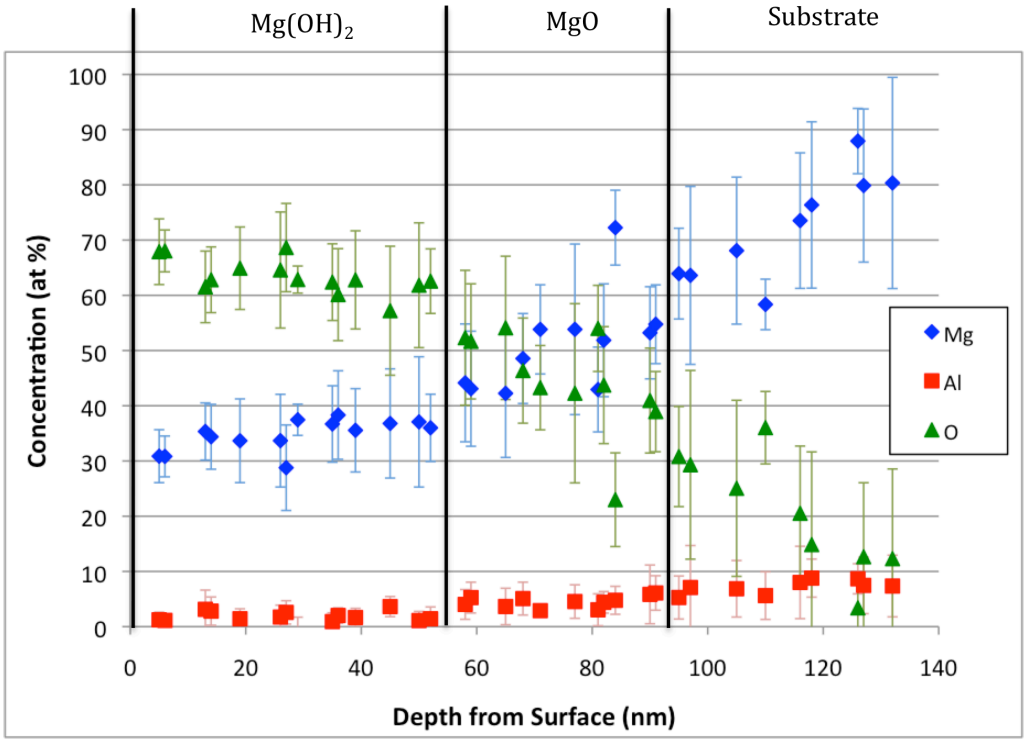

Figure 4.32: Approximated film structure on 'AZ80 – pH 14.'

4.3.3.3 AZ31 – pH 14

Many intermetallic particles were identified within the 'AZ31 – pH 14' substrate. EDS point spectra of a characteristic AlMn intermetallic particle, as well as the matrix phase, are shown in Figure 4.33. All intermetallic particles analyzed produced similar EDS spectra, regardless of their shape or size. Similar to the previous two samples, no Mn concentration was detected within the matrix phase. As before, The Cu peaks of the EDS spectra were due to the Cu grid the TEM specimen was placed on.

(A) AZ31 – pH 14: AlMn Particle **(B) AZ31 – pH 14: Matrix Phase**

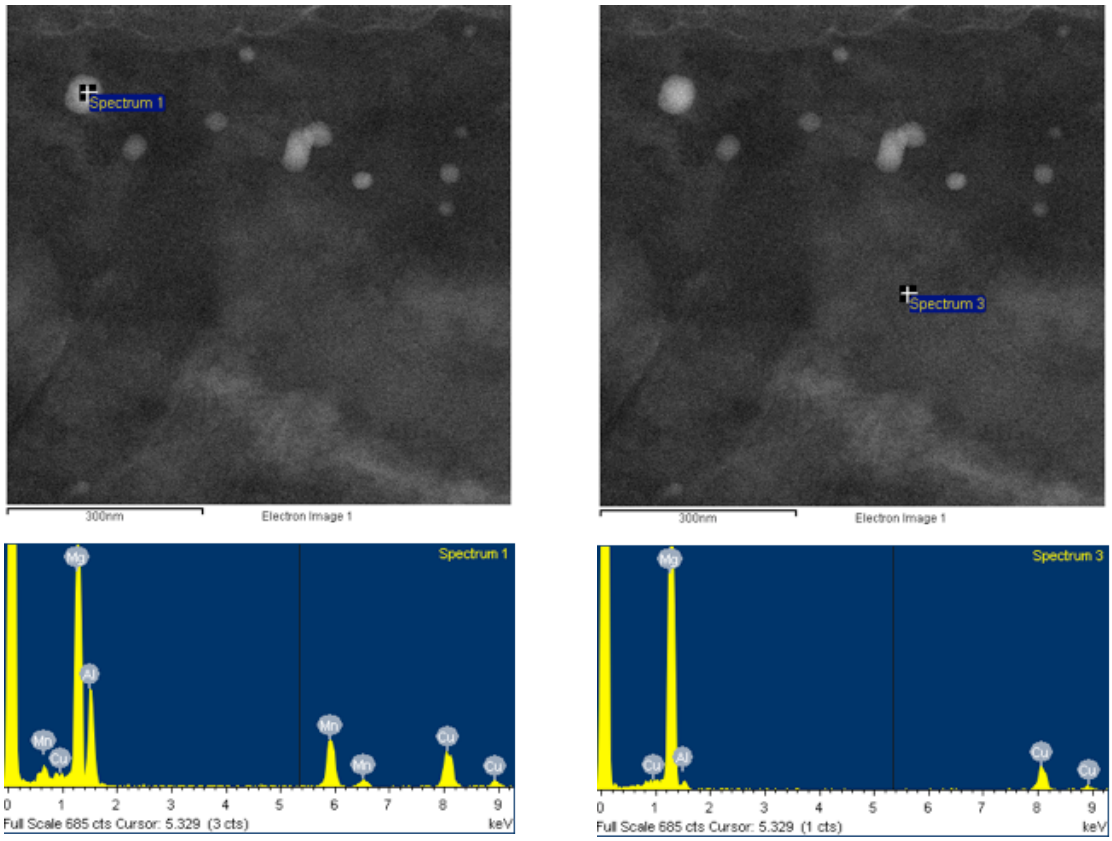

Figure 4.33: HAADF STEM image & EDS spectrum of an 'AZ31 – pH 14' (A) AlMn intermetallic particle and the (B) matrix phase.

A uniform characteristic section of the corrosion film on the 'AZ31 – pH 14' sample was selected and is shown in Figure 4.34. The corresponding SmartMap™ from the selected region is presented in Figure 4.35. A similar bi-layer corrosion film structure to the prior two AZ80 samples was observed by examining the Mg and O elemental maps. The porous outer layer of the corrosion film was the thickest of all three samples. Concentration of Al was much lower in the film for the 'AZ31 – pH 14' sample with respect to the previous two samples as observed by the much darker Al elemental map in Figure 4.35. Furthermore, the concentration of Al appeared to be higher in the substrate than in the film, which was similar to the 'AZ80 – pH 14 sample.' Accumulation of C

and Ga both occurred at the surface of the film and small amounts of C were also distributed uniformly throughout the porous outer layer.

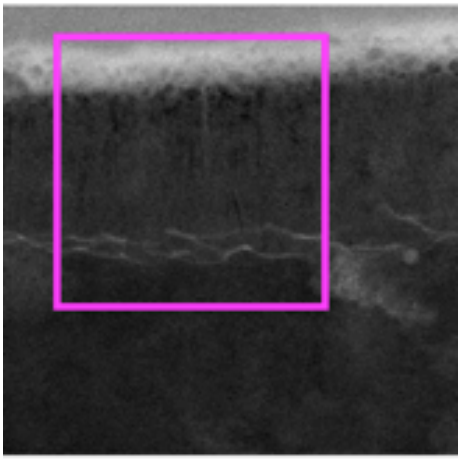

Figure 4.34: HAADF STEM image of 'AZ31 – pH 14' site of interest for SmartMap™ 1.

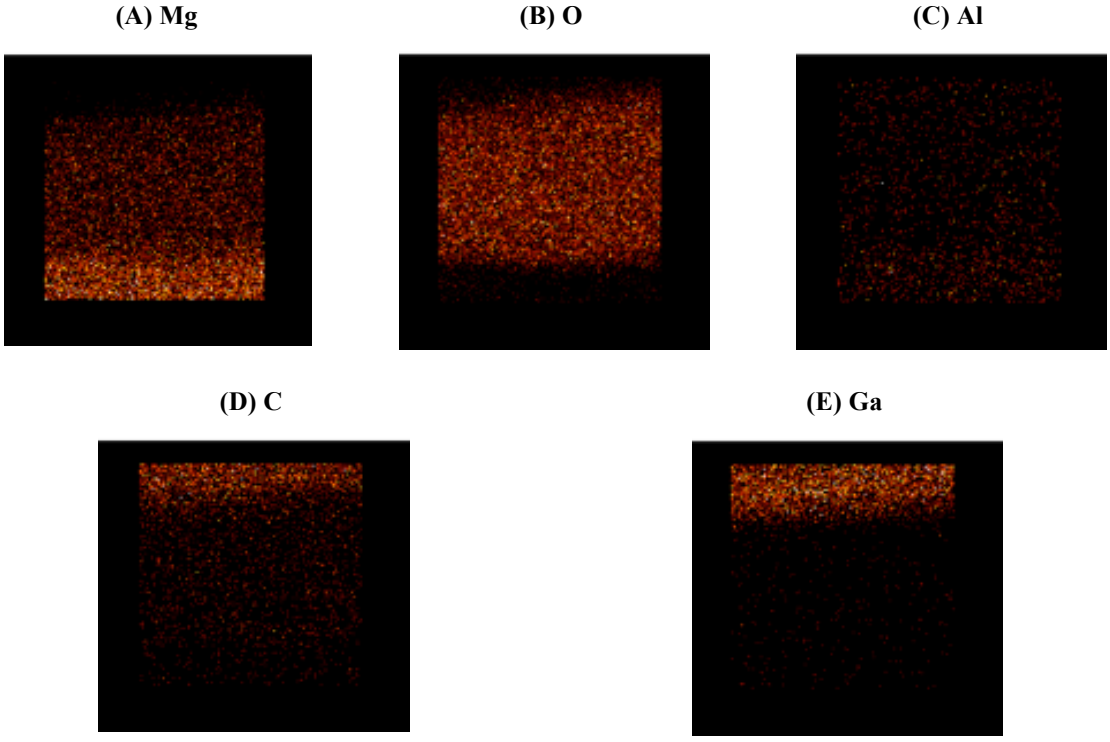

Figure 4.35: SmartMap™ 1 elemental maps of (A) Mg (B) O (C) Al (D) C (E) Ga on 'AZ31 – pH 14.'

The individual spectra utilized to quantify SmartMap™ 1 are shown in Figure 4.36. Sites of interest were chosen in approximately 50 nm intervals from the surface of

the film. Due to the uniformity of the film, few corrections regarding the depth of the film across the examined area were required to ensure the depth measurements were consistent. A scatter plot was produced with each point representing an average atomic concentration of Mg, Al or O for each individual set of spectra at a given depth. This graph is displayed in Figure 4.37. Clearly, the careful preparation of this sample produced excellent results with little scatter present except for in 'Region 2.' The bi-layer structure was readily apparent and distinct film boundaries were easily identified. Similar to the analysis performed on the previous two AZ80 samples, the (Mg + Al) : O ratios were investigated and fit into the characteristic regions. 'Region 1' was estimated to be about 250 nm thick. 'Region 2' was approximately 30 nm thick and 'Region 3' was estimated to begin at about 280 nm from the surface.

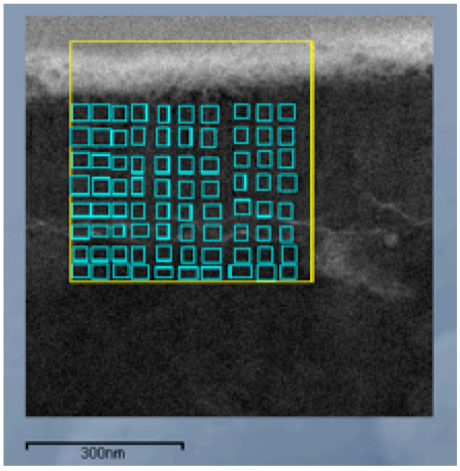

Figure 4.36: Setup for Inca™ quantification of SmartMap™ 1 on 'AZ31 – pH 14.'

Average atomic concentration values of Mg, Al and O were calculated for each point within each respective region. These values are listed in Table 4.6. Clearly, for the 'AZ31 – pH 14', the (Mg + Al) : O ratios fit well within the defined values. The outer layer (Mg + Al) : O ratio was 0.47 and the inner layer ratio was 1.1. High atomic

concentrations of Mg, as well as low atomic concentrations of O, were evident in the approximated substrate region. Al concentration was lower in the corrosion film than the alloys substrate overall. Furthermore, the Al concentration in the inner layer was much lower than that present in the inner layer of the prior two AZ80 samples.

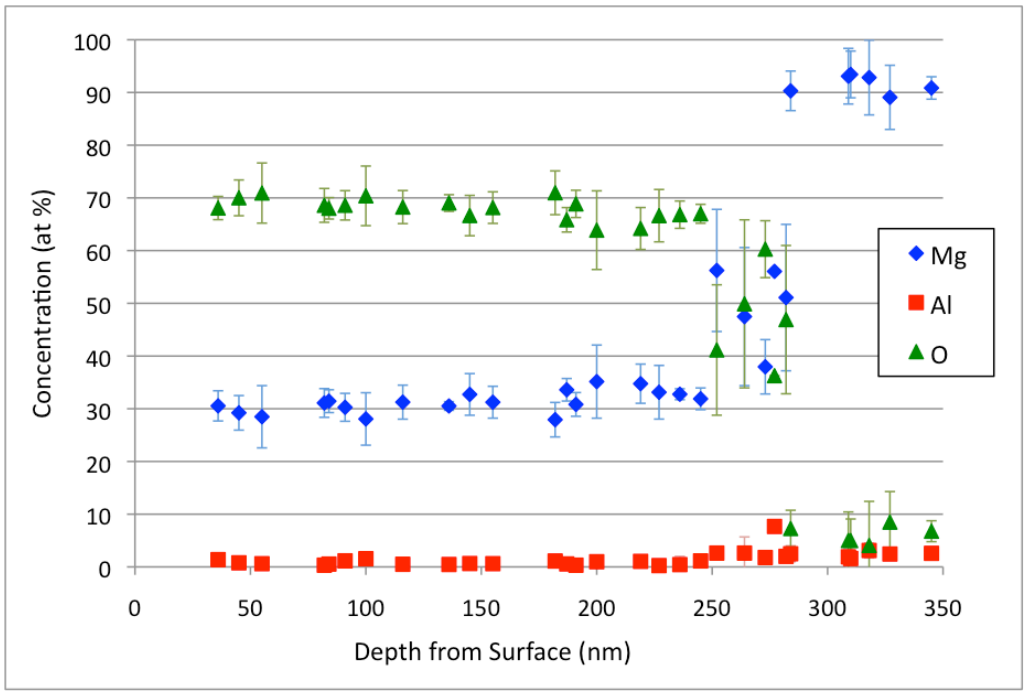

Figure 4.37: Scatter plot of Mg/Al/O concentrations from Inca™ quantitative SmartMap™ analysis of 'AZ31 – pH 14.'

Figure 4.38 shows a bounded scatter plot including the three regions of different (Mg + Al) : O atomic ratio. The consistency of the concentration values in 'Region 1' and 'Region 3' were excellent and although more scatter was present in 'Region 2,' it was significantly less than the prior two AZ80 samples. Vast improvements in sample preparation and data collection were evident when examining the results of 'AZ31 – pH 14' compared with the AZ80 samples.

Table 4.6: (Mg + Al) : O ratio and average concentration value (at%) of Mg/O/Al in the surface film at various depths on 'AZ31 – pH 14.'

	Average At% Value				
Depth (nm)	**Mg**	**Al**	**O**	**(Mg + Al) : O Ratio**	**Predominant Phase**
0-250	31	1.0	68	0.47	$Mg(OH)_2$
251-282	50	3.0	47	1.1	MgO
283+	92	2.0	6	>> 1	AZ31 substrate

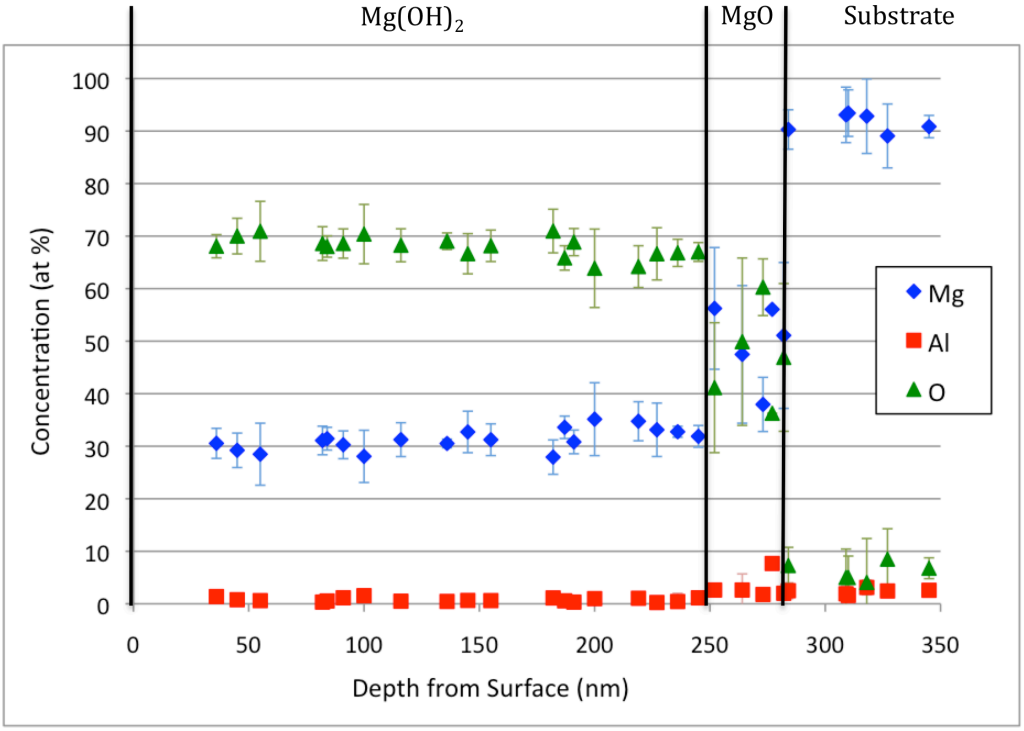

Figure 4.38: Approximated film structure of 'AZ31 – pH 14.'

4.4 ToF-SIMS Analysis

4.4.1 Overall Depth Profiles

The 'AZ80 – unexposed' sample was used to calibrate the ToF-SIMS instrument. A depth profile was acquired and is shown in Figure 4.39. It was observed that only a very thin corrosion layer was present on the surface. The signals from the various compounds analyzed decreased dramatically after about a minute of sputtering.

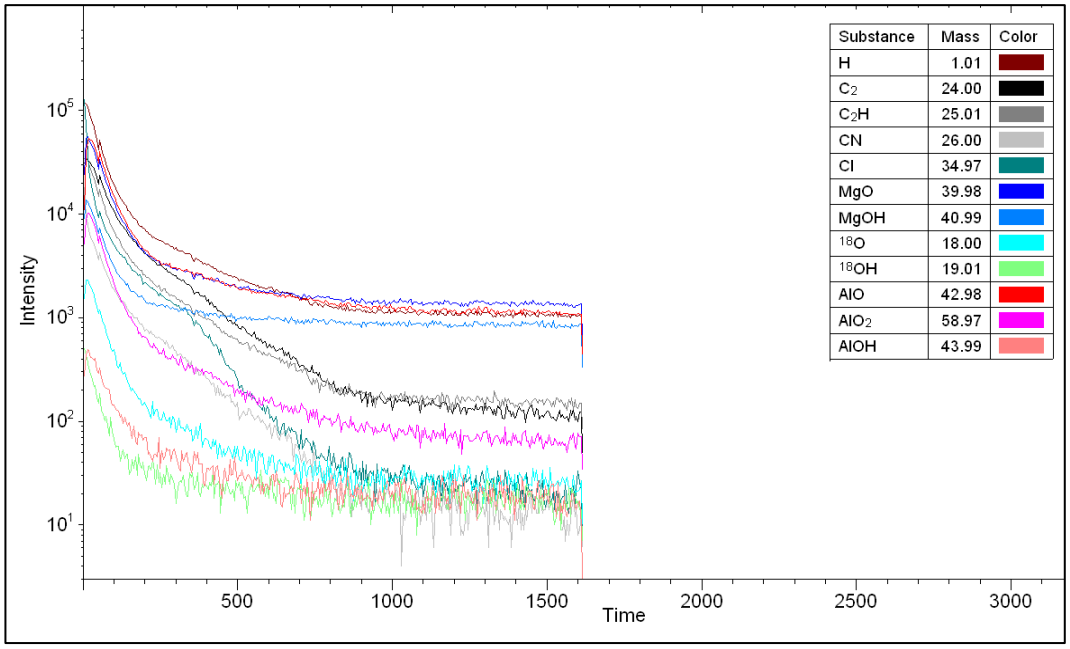

Figure 4.39: ToF-SIMS depth profile of 'AZ80 – unexposed' sample.

Depth profiles of the 'AZ80 – pH 7' and 'AZ80 – pH 14' samples are displayed in Figure 4.40. Compared to the unexposed sample, the corrosion layer on surface of the 'AZ80 – pH 7' sample was much thicker and required approximately 15 minutes to sputter through. Furthermore, a bi-layer film structure was evident. The film structure was dominated in thickness by the outer layer, but a thinner inner layer was clearly observed, as witnessed by the peaks in intensity around the 15-minute mark of Figure 4.40. Compounds containing Al appeared to exhibit the largest increase in intensity at this region. Due to the differences in sputtering yield, no estimations regarding the thickness of either layer could be ascertained.

(A) AZ80 – pH 7

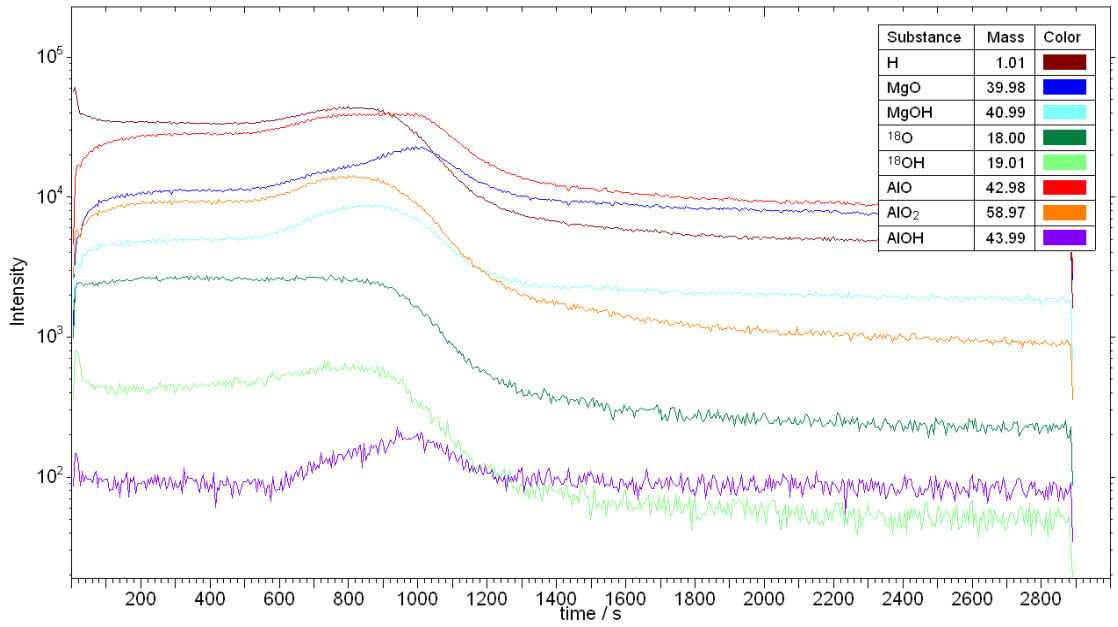

(B) AZ80 – pH 14

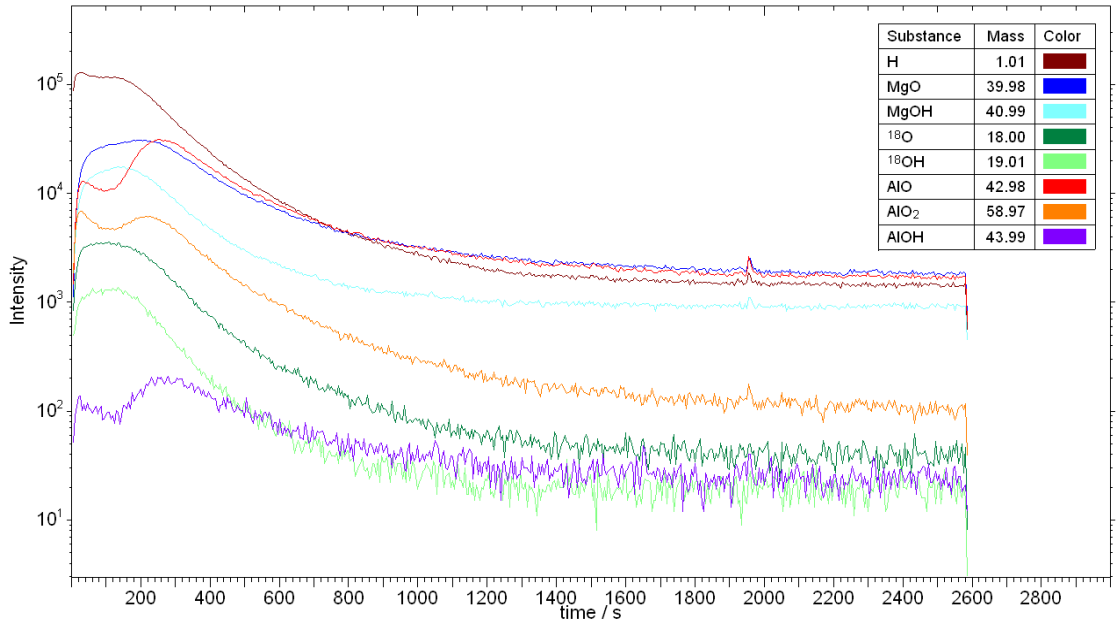

Figure 4.40: ToF-SIMS depth profiles of (A) 'AZ80 – pH 7' sample and (B) 'AZ80 – pH 14' sample.

A bi-layer structure for the 'AZ80 – pH 14' corrosion film was also observed similar to the 'AZ80 – pH 7' sample. However, the overall thickness of the corrosion film was significantly smaller and the sputtering process took only 5 minutes to fully penetrate the film. While the inner layer appeared to be similar in thickness to the 'AZ80 – pH 7' sample, the outer layer was dramatically thinner. As before, no quantitative thickness information regarding the two layers could be acquired, as the sputtering yields of each layer were different.

4.4.2 Corrosion Film Structure

4.4.2.1 AZ80 – pH 7

Individual mass spectra were acquired for both layers of the 'AZ80 – pH 7' corrosion film and are shown in Figure 4.41. Although the acquired depth profile shown in Figure 4.40 exhibited a clear two layer structure, the individual mass spectra did not show any significant differences in film composition between the two layers. Both layers were dominated in composition by MgOH and only a slight increase of MgO within the inner layer was noticed. Intensities of Al containing compounds remained relatively constant throughout the corrosion film structure. These observations are consistent with the findings of the STEM-EDS examination.

(A) Outer Layer

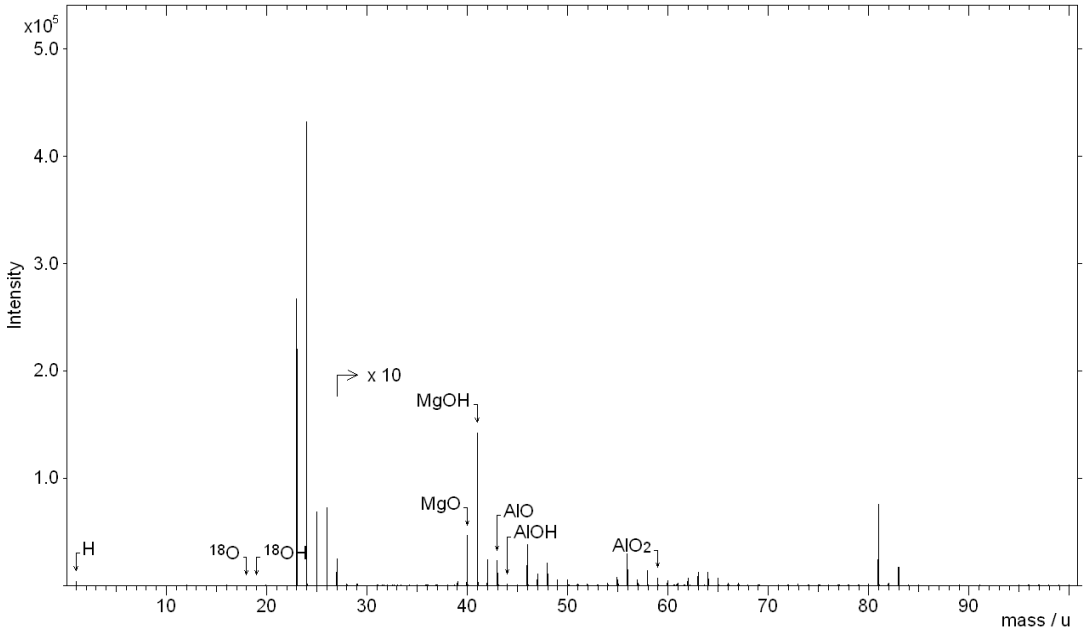

(B) Inner Layer

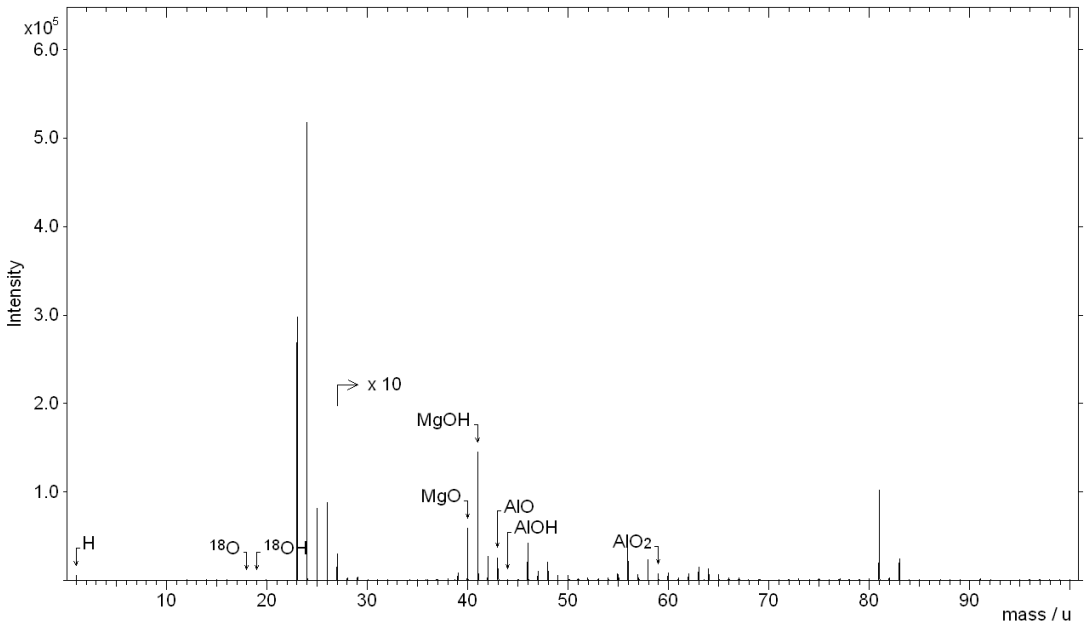

Figure 4.41: ToF – SIMS mass spectra of (A) outer layer of film and (B) inner layer of film on 'AZ80 – pH 7.'

4.4.2.2 AZ80 – pH 14

Individual mass spectra were acquired for both layers of the 'AZ80 – pH 14' corrosion film. These spectra are shown below in Figure 4.42.

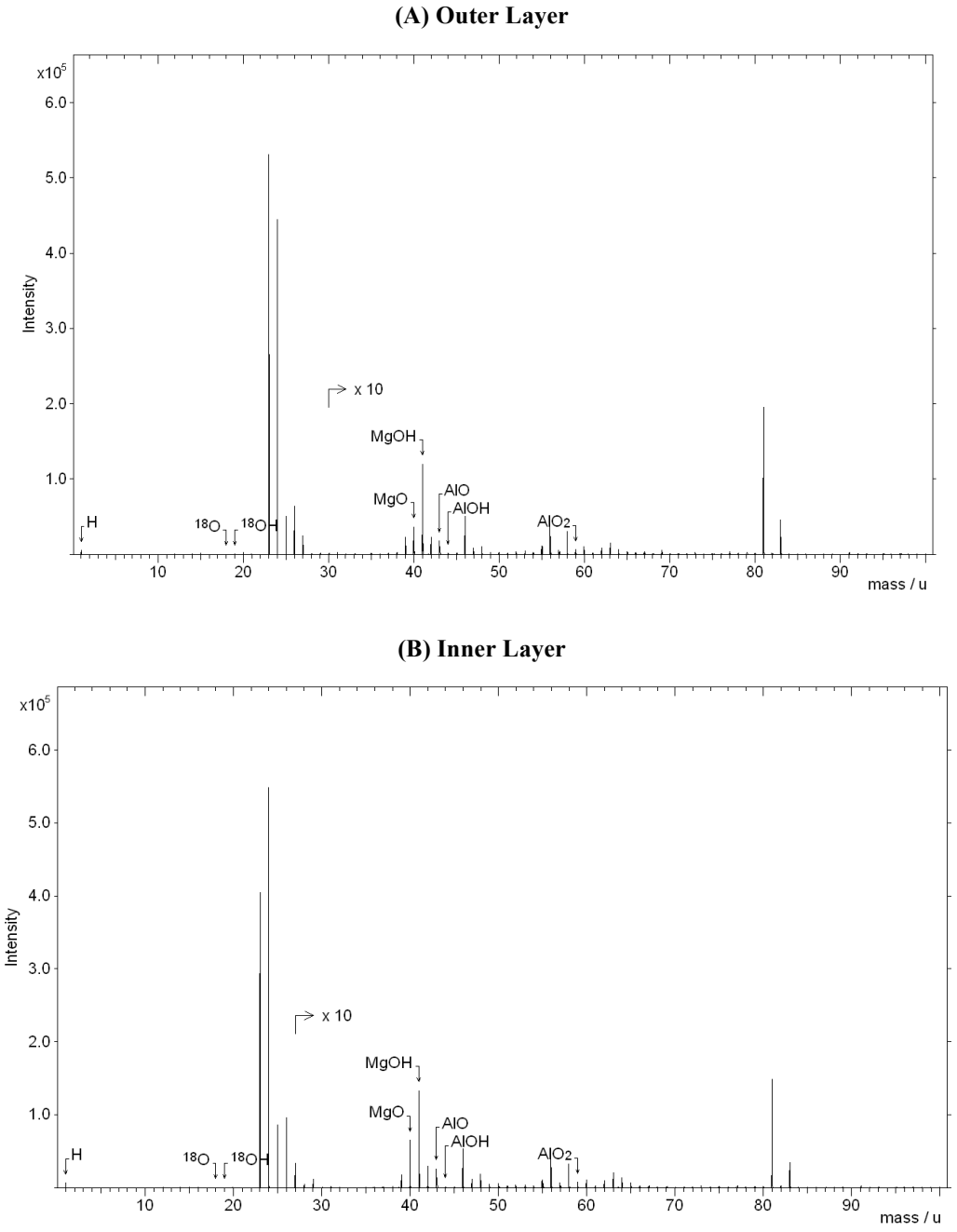

Figure 4.42: ToF – SIMS mass spectra of (A) outer layer of film and (B) inner layer of film on 'AZ80 – pH 14.'

It was found that the MgO signal intensity increased significantly in the inner layer compared to the outer layer of the corrosion film. Both layers had contributions of MgOH and MgO, however, MgOH dominated in the outer layer of the film. In addition, AlO, AlO_2 and AlOH signals were present in both layers. The Al signal intensities decreased slightly in the outer layer of the 'AZ80 – pH 14' sample, similar to what was found in the STEM-EDS examination.

4.4.3 Presence of MgH_2

Incorporation of MgH_2 into the corrosion film as a separate layer has been reported [76]. No signal corresponding to MgH_2 was found in either of the AZ80 samples during the ToF-SIMS depth profiles. The H negative profiles seen in Figure 4.40 appeared to follow the various acquired OH signals with only slight variations.

5 Discussion

5.1 Nature of Surface Film on AZ Alloys

The structure and composition of the surface film on AZ alloys when exposed to ultrapure water has been analyzed in depth using STEM/EDS and ToF-SIMS. Many important conclusions regarding both structure and composition were ascertained from the surface analysis measurements. A summary of the significant findings related to the surface film on AZ alloys is shown in Table 5.1.

Table 5.1: Summary of significant findings on the structure and composition of the surface film on AZ alloys.

Sample	Film Thickness	Film Structure	Film Composition	Al Enrichment
AZ80 pH ≈ 7	200 nm	Bi-layer: broken down inner layer	Inner: $MgO/Mg(OH)_2$ Outer: $Mg(OH)_2$	Overall, greater in film than substrate
AZ80 pH = 14	100 nm (thinnest)	Bi-Layer: stable inner layer	Inner: Mostly MgO Outer: $Mg(OH)_2$	Overall, less in film than substrate
AZ31 pH = 14	300 nm (thickest)	Bi-Layer: stable inner layer	Inner: Mostly MgO Outer: $Mg(OH)_2$	Overall, less in film than substrate

From Table 5.1, it is clear that the general structure and composition of the surface films formed in near-neutral and alkaline environments on AZ alloys were similar regardless of the vast difference in pH. All three samples possessed bi-layer film structures consisting of an inner barrier layer and an outer hydroxide layer. However, it was noticeable that the inner barrier layer on 'AZ80 – pH 7' was significantly more broken down than the inner barrier layers on 'AZ80 – pH 14' and 'AZ31 – pH 14.' The composition of this layer was a mixture of $MgO/Mg(OH)_2$ whereas the inner barrier layers on the pH 14 samples were predominantly composed of MgO. The surface film on 'AZ80 – pH 7' was twice as thick as the film on 'AZ80 – pH14.' In addition, all films

were porous in structure with 'AZ80 – pH 7' exhibiting the highest degree of porosity. Therefore, increasing the pH from 7 – 14 increased the stability of the inner barrier layer as well as the overall film structure itself.

The effect of alloyed Al concentration on the structure and composition of the film was less apparent. Increasing alloyed Al concentration from 3 wt % in AZ31 to 8 wt % in AZ80 caused a reduction in the thickness of the surface film by 3 times. Thus, the higher amount of Al enrichment into the surface film on 'AZ80 – pH 14,' increased the stability of the surface film with respect to 'AZ31 – pH 14.' However, Al enrichment of the surface film on 'AZ80 – pH 7' was much greater than in the film on 'AZ80 – pH 14,' but the film thickness in the near-neutral environment was double that of the alkaline environment. As a result, the effect of alloyed Al concentration on the AZ alloy surface film structure and composition is less significant than the effect of environmental pH.

5.1.1 Structure and Composition of Surface Film from the Literature

5.1.1.1 Short Time Exposures (< 12 hrs)

Since this study focuses on the evolution of the surface film during long time exposures, it is important to begin a detailed comparison with the literature by examining the initial state of the corrosion film at short time exposures. That way an understanding of how the film transforms over long periods of time can be ascertained. Splinter and McIntyre studied the atmospheric corrosion behaviour of Mg-Al surfaces in humid D_2O environments and found that Al enriched the air-formed oxide film [8]. They also observed a thin hydroxide layer growing on the surface of the oxide film, which suggests hydration of the oxide occurred immediately. Feliu Jr et al. has also studied the atmospheric corrosion behaviour of AZ alloys in humid environments [6, 26-29]. They

reported a bi-layer structure where a thin hydroxide layer grows on the surface of the initial air-formed oxide layer [26]. Liu et al. proposed the hydroxide layer formed on pure Mg in atmospheric conditions was very thin, and the overall structure of the surface film was more indicative of a single oxide layer [33]. However, when they exposed the sample to ultrapure water, the film quickly hydrated and a duplex film structure composed of $MgO/Mg(OH)_2$ with significant porosity was observed. Santamaria et al. also observed similar behaviour on pure Mg exposed to NaOH solutions (pH > 13) for 1 – 2 hrs, where only a thin MgO layer was detected by XPS, and the dominant species in the corrosion film was $Mg(OH)_2$ [39]. Clearly, a relatively general consensus regarding the structure and composition of the surface film on AZ alloys at short time exposures has been reached. A bi-layer structure of $MgO/Mg(OH)_2$ is present and as time elapses, the thickness of the $Mg(OH)_2$ layer continues to increase.

5.1.1.2 Long Time Exposures (≥ 12 hrs)

Previous studies concerning the structure and composition of surface films formed on pure Mg and AZ alloys after long time exposures have been undertaken. However, quite often dramatically different observations concerning the corrosion film structure and composition are reported. Song et al. reported a bi-layer film structure on AZ21 and AZ91 when exposed to 1 N NaCl environment (pH = 11) for 24 hrs using XPS and EIS [19]. They proposed the possibility of an Al_2O_3 healing layer occurring beneath the bi-layer film structure, however they were unable to prove its existence and suggested it may not be continuous across the surface. Wang et al. found that after 20 hrs of exposure to 0.01 M NaCl solution, the film on AZ31 was composed of a mixture of MgO and

$Mg(OH)_2$ [44]. The inner region of the corrosion film contained higher concentrations of MgO and the outer region was predominantly $Mg(OH)_2$. Ismail and Virtanen reported the surface film on AZ31 exposed to 0.5 M KOH solution (pH = 13.5) for 24 hrs consisted of both a MgO and $Mg(OH)_2$ layer [31]. The outer Mg(OH)2 layer was composed of platelets likely through a dissolution-precipitation reaction. Mathieu et al. found a layered double hydroxide hydrotalcite film structure on synthetic α-phases exposed to ASTM D1384 water for 12 hrs [14]. The hydrotalcite film structure was said to form naturally due to charge deficiencies in the $Mg(OH)_2$ film structure as a result of Al enrichment.

Perhaps the most well known study focused on the structure and composition of the surface film on AZ alloys after long time exposures is that of Nordlien et al. They observed a three-layer film structure on AZ alloys exposed to distilled water for 48 hours under TEM consisting of a rapidly damaged inner layer, a dense intermediate layer and a platelet-like outer layer [5]. While they were able to identify the intermediate and outer layers of the corrosion film, they were unable to classify the phase or structure of the inner layer. It was reported that the inner layer transformed from an unknown phase into new crystalline grains of MgO after dehydration from the electron beam. The damage observed on the 'AZ80 – pH 7' sample (Figure 4.14) was visually similar to the damage witnessed by Nordlien et al., however the location was slightly different. Damage occurred above and beneath the air-formed oxide layer whereas Nordlien et al. only observed the damage beneath it. It is possible that this damage caused Nordlien et al. to

believe that the film structure consisted of three distinct layers, when in fact the inner layer was likely an artifact of beam irradiation damage.

Unlike the short time exposures, the research findings concerning the structure and composition of the surface film on AZ alloys are highly inconsistent. The results of this study shows that the bi-layer structure formed at short time exposures remains mostly in tact even after long times. Further hydration of the inner barrier layer occurs and the hydroxide layer grows thicker on the surface of AZ alloys. The surface film is similar to that reported by Ismail and Virtanen as well as Wang et al [31, 45]. No evidence of a tri-layer film, layered double hydroxide structure, or Al_2O_3 healing layer was observed in this work.

5.1.2 Stability of Surface Film on AZ Alloys

5.1.2.1 E_{corr} Stability of the Surface Film

The 48 hr E_{corr} behaviour of AZ alloys differed significantly between the near-neutral (pH ≈ 7) and alkaline (pH = 14) environments (Figure 4.2). While the near-neutral exposures exhibited essentially constant values of E_{corr}, the alkaline environment produced highly erratic fluctuations in E_{corr}. The large potential drops of nearly 1 V were evident in all 48 hr E_{corr} measurements, however the curves were not entirely reproducible. Different samples produced potential drops that occurred at different times and the magnitude of the drop varied regularly as shown in Figure 4.2. It was noticed however that after a period of about 24 hrs, the E_{corr} appeared to level approximately 200 mV nobler than the starting potential signifying a steady-state may have been reached.

Ismail and Virtanen reported these irregular fluctuations on AZ31 exposed to 0.5 M KOH (pH = 13.5) solution for 24 hrs [31]. However, they found that the steady-state

potential was reproducible after 24 hrs and occurred approximately 1.2 V nobler than the initial E_{corr}. The potential drops represented cyclic active-passive corrosion behaviour where the potential drops were related to exposure of the bare metal surface to the electrolyte. XPS, along with EIS measurements revealed the film structure was in fact bi-layer with an inner layer of MgO and an outer layer of $Mg(OH)_2$; both were enriched with Al. To expose the bare metal, they proposed that the sizeable difference in Pilling Bedworth Ratio (PBR) for MgO and $Mg(OH)_2$ caused internal stresses within the oxide/hydroxide structure and inevitably lead to rupture of the corrosion film. The film would then flake off, dissolve into solution and the metal surface would be exposed to the solution before re-passivating via precipitation of $Mg(OH)_2$. Alternatively, the inner layer of the film could undergo self-healing and resist dissolution altogether.

The cause for rupture of the corrosion film was solely attributable to the PBR of the oxide/hydroxide. While the difference in PBR is sizeable, the favourable hydration of MgO to $Mg(OH)_2$ was overlooked. The wide-scale chemical breakdown observed in the near-neutral environment likely required a much larger driving force than a mismatch in PBR. Furthermore, if PBR mismatch were responsible for breakdown of the MgO, similar active-passive transitions would have been present in the E_{corr} behaviour at near-neutral pH as the surface film structure formed on AZ31 was similar. However, no potential drops were observed suggesting that the mechanism responsible for the breakdown of MgO behaved differently in both environments and therefore, could not be due to PBR mismatch.

5.1.2.2 Hydration of MgO (Chemical Breakdown)

The inner barrier layer on 'AZ31 – pH 14' displayed a clear weaving pattern with non-uniform contrast throughout (Figure 4.18). This weaving pattern was indicative of a rough interface. Natural aqueous corrosion processes are likely to produce rough interfaces, due to ion transfer from metal and electrolyte through the air-formed oxide barrier layer. Furthermore, samples were only polished to 4000 grit and thus, significant micro-roughness was likely present. The contrast, which was present in the inner barrier layer, could arise from two separate possibilities: elemental enrichment or micro-strain at the interface. EDS scans (Figure 4.35) did not show any significant enrichment of any of the elements within the AZ alloy or from the FIB process and therefore, elemental enrichment was ruled out.

Favourable hydration of MgO to $Mg(OH)_2$, produces a sizeable volume expansion which likely caused significant strain on the structure of the inner barrier layer [77]. Porosity as well as some $Mg(OH)_2$ was observed in the inner barrier layer on 'AZ31 – pH 14,' and therefore, it was probable that considerable hydration had occurred. Examination of the lattice structures of Mg, MgO and $Mg(OH)_2$ could provide further evidence of why micro-strain likely caused the bright contrast observed in the inner layer. Mg and $Mg(OH)_2$ are two well known hexagonal materials, however, MgO is cubic and therefore, lattice mismatch between the different phases will cause strain at the interface [78-80]. Nonetheless, lattice mismatch would likely only cause strain at the inner barrier layer interfaces and not throughout the layer itself. As a result, hydration of MgO to $Mg(OH)_2$ was probably responsible for the majority of the strain observed in the inner

barrier layer on 'AZ31 – pH 14.' This highly strained inner oxide layer was also observed on the 'AZ80 – pH 7' sample and was likely present on the 'AZ80 – pH 14' sample, however the Pt topcoat did not allow for the contrast to be observed.

It appeared that the favourable hydration of MgO to $Mg(OH)_2$ played the largest role in controlling the structure of the surface film on AZ alloys. The inner oxide barrier layer was severely compromised in the near-neutral environment to the point where its identification was difficult. Significant $Mg(OH)_2$ was found within the inner layer suggesting wide scale hydration took place. In the alkaline environment, the inner barrier layer could be identified clearly on both samples. However, some $Mg(OH)_2$ was still evident, suggesting hydration also occurred but at a much slower rate.

Hydration of MgO to $Mg(OH)_2$ in alkaline pH has been shown to be significantly slower than in neutral pH [66]. As a result, the majority of the Al enriched MgO inner layer remained in tact for both 'AZ80 – pH 14' and 'AZ31 – pH 14.' Since no aggressive ions were present in the solutions of ultrapure water, classical electrochemical breakdown of the inner oxide layer was not responsible for its breakdown. Breakdown of the inner oxide barrier layer occurred via natural hydration and as such was not influenced by the microstructure of the alloy.

Mejias et al. reported that hydration of MgO initiated at defect sites within the film structure such as dislocations and grain boundaries [66]. The hydration of MgO to $Mg(OH)_2$ produces a sizeable volume expansion, which has been a considerable problem in refractory design for furnace linings [77]. Cracking of the MgO refractories and furthermore, the furnace lining has been attributed to natural hydration of MgO to

$Mg(OH)_2$. Therefore, it is possible that once hydration initiates, cracks in the inner barrier layer form due to the associated volume expansion. As a result, more defect sites are produced and hydration rates increase causing widespread breakdown of the inner oxide barrier layer as was observed on 'AZ80 – pH 7'. Since hydration rates are much slower in alkaline solution, this process may be far less severe than in neutral conditions. The specific hydration mechanism responsible for the breakdown of the MgO inner barrier layer requires further study.

5.1.2.3 Electrochemical Breakdown of Surface Film

Natural hydration of MgO to $Mg(OH)_2$ significantly affected the inner layer, especially in neutral pH where the layer was difficult to identify using EDS. However, potentiodynamic experiments (Figure 4.3) showed the corrosion rate at E_{corr} was quite low suggesting the surface film on AZ alloys was in fact stable even in the 0.01 M NaCl solution.

Electrochemical breakdown occurred at very small anodic overpotentials during the potentiodynamic measurements (Figure 4.3). In addition, no breakdown potentials were observed in the 0.01 M NaCl near-neutral (pH ≈ 7) environment for the Mg-Al binary alloys but widespread pitting occurred across the surface (Figure 4.10). This suggested that the breakdown potential was actually lower than the corrosion potential itself. The breakdown of the corrosion film during electrochemical testing is different than the breakdown of the inner barrier layer due to natural hydration (chemical breakdown), which would not be potential dependent. Therefore, it is necessary to

consider the possibilities responsible for causing the electrochemical breakdown and instability of the $MgO/Mg(OH)_2$ film structure in mildly aggressive neutral environments.

Microgalvanic activity between the α matrix phase and secondary phases is another possible explanation for the exceedingly low breakdown potential exhibited by AZ alloys in mildly aggressive solutions. Lunder et al. have tabulated galvanic potential values for various AlMn intermetallic particles as well as the β phase [4]. They have demonstrated that a large driving force for microgalvanic attack is present on AZ alloys and this coupling could be responsible for limited corrosion resistance in neutral environments. It has also been reported on multiple occasions that the β phase forms highly efficient cathodes within the AZ alloy microstructure and causes widespread breakdown of the surface film [3, 10, 12-15].

However, no evidence of microgalvanic corrosion controlling the breakdown of the surface film was observed. Breakdown potentials for Mg, AZ31 and AZ80 were all identical (Table 4.1), and as a result, microstructural features such as AlMn intermetallic particles or the β phase could not be deemed responsible for the breakdown of the surface film. Williams et al. proposed that Cl^- concentration of the test solution was a precursor to the breakdown of the surface film formed on pure Mg [67]. Cl^- ions are incorporated into the surface film at weak points and form soluble magnesium hydroxy-chloride complexes, which dissolve readily and deteriorate the film structure. Since, the breakdown potentials in this study appeared to be independent of microstructure and the test solution concentration was constant, their theory appears to be plausible. It is difficult to validate this theory due to the close proximity of the breakdown potential to

the corrosion potential. Commonly, 3.5 - 5 wt % NaCl test solutions are used to study AZ alloys and pitting potentials are commonly absent (although widespread pitting occurs on the surface) due to the aggressiveness of the solution [3, 15, 19, 21]. Pitting occurs at the corrosion potential, and therefore, no conclusions can be made regarding the location of the breakdown potential. Extremely dilute solutions (< 0.01 M NaCl) would need to be utilized to investigate the movement of the breakdown potential and verify the theory proposed by Williams et al. Since, this work focused on the effect of alloying, no investigation regarding the influence of solution concentration was performed. Consequently, it is left as a topic for future consideration.

5.2 Factors Controlling Anodic and Cathodic Kinetics on AZ Alloys

Table 5.2 summarizes whether the anodic or cathodic kinetics were affected or unaffected with respect to 4N Mg by alloyed Al concentration and solution pH.

Table 5.2: Summary of Al alloying and solution pH effect on the anodic and cathodic parameters of AZ alloys with respect to 4N Mg.

Alloyed Al %	Near-Neutral (pH ≈ 7)		Alkaline (pH = 14)	
	Anodic Kinetics	Cathodic Kinetics	Anodic Kinetics	Cathodic Kinetics
0 – 3 wt % (Mg vs AZ31)	Slightly Affected	Affected	Affected	Affected
3 – 8 wt % (AZ31 vs AZ80)	Unaffected	Unaffected	Significantly Affected	Unaffected

From Table 5.2, it is clear that alloying Al up to 3 wt % affected the anodic and cathodic kinetics of AZ alloys compared with 4N Mg. It was also found that as Al alloying increased from 3 - 8 wt %, only the anodic kinetics of the alkaline (pH = 14) environment were altered, while the remainder of the parameters were unaffected by the increase in alloying.

5.2.1 Anodic Behaviour

The anodic kinetics on AZ alloys are governed by the stability of the surface film formed through aqueous exposure. Therefore, the properties of the corrosion film itself plays a large role in determining the current density exhibited at anodic overpotentials. In the 0.01 M NaCl near-neutral (pH ≈ 7) environment, the anodic kinetics were only slightly affected by alloying Al from 0 – 3 wt % as observed by the polarization behaviour (Figure 4.3). Furthermore, no change in the anodic parameter i_a was perceived with respect to 4N Mg (Table 4.1). This suggested that Al alloying only affected the extremely narrow range of passivity before electrochemical breakdown occurred. Once electrochemical breakdown of the surface film initiated, wide scale pitting of the surface on AZ alloys was similar to that on 4N Mg.

The effect of Al on the narrow range of passivity may be attributable to the enrichment of the corrosion film with Al^{3+} cations, lowering the concentration of Mg^{2+} interstitial defects inherent within the metal excess air-formed oxide film. Splinter and McIntyre proposed this concept on Mg-Al surfaces exposed to D_2O water vapour and appears to be a plausible explanation for the marked decrease in anodic dissolution rate [8].

Electrochemical breakdown of AZ alloys occurred at very small anodic overpotentials (Figure 4.3) and was likely correlated to the compromised inner barrier layer. In the earlier sections addressing the corrosion film structure in near-neutral (pH ≈ 7) ultrapure water environments, rapid hydration leading to a chemical breakdown of the inner air-formed oxide layer decreased the stability of the layer dramatically.

Introduction of aggressive Cl^- ions into the exposure environment likely penetrated the compromised layer rather easily and initiated pitting corrosion of the alloy surface immediately. Multiple studies using more aggressive 3.5 – 5 wt % NaCl solutions were unable to identify a breakdown potential at all on AZ alloys, which was likely lower than the corrosion potential itself [3, 15, 19, 21]. This suggested that the affect of lowering Mg^{2+} concentration defects within the inner barrier layer through Al alloying, only played a minor role in controlling the anodic dissolution rate. It also explained the similarity in the values of i_a and the seemingly overlapping anodic branches of the polarization curves for AZ31 and AZ80 (Table 4.1 & Figure 4.3). Hydration and Cl^- concentration had a much larger influence on the anodic kinetics in the near-neutral environment.

The anodic kinetics in the 0.01 M NaCl alkaline (pH = 14) environment exhibited drastically different behaviour from those of the near-neutral environment (Figure 4.3). Measurements of anodically polarized current densities (i_a) were orders of magnitude smaller, and limiting current densities (i_L), representing mass transport controlled kinetics were present on all samples tested. Furthermore, no electrochemical breakdown potentials were observed, suggesting the inner barrier layer was significantly more stable. This observation was verified by the STEM images and EDS analysis of 'AZ31 – pH 14' (Figure 4.18 & Table 4.6). Hydration rates are markedly slower in alkaline environments, and thus, chemical breakdown of the inner barrier layer was far less severe than for the near-neutral environment. The increased stability probably caused an increase in the driving force for dissolution of cations through the surface film and into solution. It also

prevented the aggressive Cl^- ions from electrochemically breaking down the structure of the film and initiating pitting corrosion.

Limiting current densities on the anodic branch of the polarization curve are indicative of maximum dissolution rates of cations through the surface film. This indicates that diffusion of cations through the surface film governs the observed anodic current densities. As alloyed Al content increased from 3 – 8 wt %, the limiting current density decreased by more than one order of magnitude (Figure 4.3). In addition, the film thickness was three times thinner on 'AZ80 – pH 14' than on 'AZ31 – pH 14' (Table 4.5 & Table 4.6), suggesting the degree of hydration was also reduced by further Al alloying. Therefore, the stability of the inner barrier layer was increased on AZ80 in alkaline solutions. Enhancement of the properties of the inner air-formed oxide layer occurred despite the thermodynamic instability of Al in alkaline environments. The specific mechanism responsible for this increased stability remains uncertain and requires further study.

5.2.2 Cathodic Behaviour

The cathodic kinetics on AZ alloys are controlled by the rates of hydrogen evolution [56]. Oxygen reduction does not play a role in the overall corrosion process, and thus, unlike Fe, Al or other structural engineering metals; it does not affect the cathodic kinetics [36]. As a result, it is important to understand where the hydrogen evolution reaction is occurring. The hydrogen evolution reaction could feasibly occur on the surface of the alloy or on the surface of one of the film layers.

If the cathodic reaction was occurring on the substrate of AZ alloys, four possible cathodic factors could be controlling the reaction: [Al], [Zn], [β phase], or [AlMn intermetallic particles]. Since the cathodic behaviour on AZ31 and AZ80 was markedly similar (Figure 4.3 & Table 4.1), the β phase cannot be controlling the hydrogen evolution reaction. AZ80 contains the β phase and AZ31 does not, so therefore, the β phase can be ruled out. AlMn intermetallic particles only cover a very small portion of the microstructure on both AZ31 and AZ80 (Figure 3.2), and therefore, are also unlikely to control the cathodic kinetics. Alloyed Zn concentration between the AZ31 and AZ80 is similar (Table 3.2) and has been reported to increase the rate of hydrogen evolution on AZ alloys, making them more susceptible to corrosion [5]. However, the calculated values of $i_{o,c}$ (Table 4.1) in this study were lower on AZ alloys, which contained Zn than on 4N Mg that contained no Zn. As a result, Zn concentration at the metal surface controlling the cathodic kinetics is unlikely. Alloyed Al content cannot be excluded by examining the measurements performed in this study. However, the extracted values of $i_{o,c}$ (Table 4.1) are much smaller than those typically found on a bare metal surface [81]. Therefore, it is unlikely that Al concentration at the metal surface controls the kinetics of the hydrogen evolution reaction.

It is expected that the cathodic hydrogen evolution reaction is not occurring directly on the surface of the AZ alloys. Instead, the cathodic reaction may occur on the surface of the inner barrier layer or outer hydroxide layer of the corrosion film where exchange currents are much smaller. Song et al. found the hydrogen evolved at the surface of the film on pure Mg exposed to 1 N NaCl solution [40]. They reported an $i_{o,c}$

value of 50 x 10^{-12} A/cm^2, which is strikingly similar to the value found on 4N Mg in this study (Table 4.1) and bestows confidence in the values of $i_{o,c}$ extracted through Tafel extrapolation in this work. [40] As a result, it is reasonable to assume that the cathodic kinetics are independent of the surface microstructure and in fact, dependent on the chemical and structural aspects of the corrosion film itself. However, which surface in the corrosion film structure the hydrogen evolution reaction occurred on remains unclear, as the film models presented by Song et al. are not corroborated by other research studies [19].

Al enrichment within the inner barrier layer was observed on all AZ alloy samples analyzed by STEM (Table 4.4, Table 4.5 & Table 4.6). The incorporation of Al at the surface of the air-formed oxide structure may in fact alter the electrocatalytic properties of the film, with respect to an oxide composed of pure MgO. If Al enrichment of MgO does slow down the rate of hydrogen evolution at the surface of the inner barrier layer, the drastic reduction in $i_{o,c}$ may be justified. This property requires further study.

The rate of hydrogen evolution was slightly reduced in the 0.01 M NaCl alkaline (pH = 14) compared to the 0.01 M NaCl near-neutral (pH ≈ 7) environment (Table 4.1). This was likely due to the increased stability of the inner barrier layer in the alkaline environment. Significantly, more porosity and breakdown was observed in the inner barrier layer of the 'AZ80 – pH 7' sample (Figure 4.13A) and, as a result, the driving forces controlling the hydrogen evolution process may have been reduced. The porosity present in the inner barrier layer could have caused more surface area to come into contact with the solution; increasing the rate of the cathodic reaction. Further study

focused on the effect of solution pH on the rate of hydrogen evolution on AZ alloys is required.

Interestingly, as alloyed Al concentration increased from 3 – 8 wt %, no effect was observed on the cathodic kinetics of AZ alloys (Table 4.1). Therefore, reduction of the rate of hydrogen evolution was solely caused by alloying Al up to 3 wt % and any further additions did not reduce the rate any further. This was slightly unexpected as more Al was incorporated into the inner barrier layer on AZ80 than on AZ31. If enrichment of Al were in fact responsible for the reduction in hydrogen evolution, it would be expected that more Al incorporation into the inner barrier layer would reduce the rate further. However, this was not observed. The apparent saturation of the reduction in hydrogen evolution rate as alloyed Al concentration increases above 3 wt % on AZ alloys also requires further study.

5.2.3 Corrosion Rate

Throughout this study it was witnessed that slight improvements to the corrosion behaviour resulted from alloyed Al concentration. In the near-neutral environment, the corrosion rates of the tested alloys, regardless of whether the potential was at E_{corr} or anodically polarized, were AZ80 ≅ AZ31 < 4N Mg. In the alkaline environment, the corrosion rate at E_{corr} was also AZ80 ≅ AZ31 < 4N Mg. However, if the potential was anodically polarized in the alkaline environment, the corrosion rate of AZ80 < AZ31 due to the increased stability of the inner barrier layer. Therefore, from an overall corrosion perspective, AZ80 provided the best corrosion resistance.

The corrosion rates in the near-neutral environment were significantly higher than those of the alkaline environment. Hydration of the MgO layer at pH ≈ 7 was extensive, and as a result, anodic current densities were exceedingly high. Only a narrow region of passivity was observed, and therefore, AZ alloys cannot be successfully used in an environment this aggressive where anodic polarization is possible. If the AZ alloy remained at the corrosion potential exclusively, the alloy could be utilized, but that is highly unlikely given the electrochemical reactivity of Mg with respect to other engineering metals.

The increased stability of the inner barrier layer played the largest role in the reduction of corrosion rates in the alkaline environment. Anodic currents ($i_a \cong i_L$) were controlled by the diffusion of the cations through the surface film. Due to slower hydration of the inner MgO layer in the alkaline environment, diffusion of cations from the surface of the metal into solution was more difficult, and thus, mass transport controlled kinetics were exhibited on AZ alloys. Corrosion currents were acceptable even at significant anodic overpotentials, and therefore, AZ alloys can be employed in alkaline mildly aggressive solutions with confidence.

6 Conclusion

Throughout this study, it was clear that the corrosion performance of AZ alloys was primarily related to the structure and composition of the surface film. Cryogenically cooled cross-sections of the corrosion film on AZ alloys were accurately imaged and analyzed using STEM-EDS. The surface film was verified to be bi-layer in nature, consisting of an inner MgO rich layer and a porous outer $Mg(OH)_2$ layer. The outer $Mg(OH)_2$ layer dominated the thickness of the surface film in most cases and both layers were enriched with Al. While MgO and $Mg(OH)_2$ dominated the composition of the inner and outer layers respectively, a mixed oxide/hydroxide more accurately described the overall film composition. No evidence of a tri-layer film, layered double hydroxide structure, or distinct Al_2O_3 healing layer was found on any of the samples studied using STEM.

While the surface film formed on AZ alloys in near-neutral and alkaline environments was mostly similar, one major difference was observed throughout this work. The inner barrier layer was significantly easier to identify in the alkaline environment, whereas it was difficult to locate in the near-neutral exposure. Structurally, the inner barrier layer was noticeably more deteriorated in the 'AZ80 – pH 7' sample. Furthermore, its composition was not predominantly Al-enriched MgO and likely contained as much or more Al-enriched $Mg(OH)_2$. The thickness of the surface film on 'AZ80 – pH 14' was half that of 'AZ80 – pH 7' further demonstrating the increased stability of the inner barrier layer in alkaline conditions.

The most likely cause for the noticeable difference in stability of the inner barrier layer was the rate of favourable hydration of MgO to $Mg(OH)_2$. Hydration is much quicker in neutral than alkaline environments and therefore, likely was responsible for the difficulty in locating the inner barrier layer of 'AZ80 – pH 7' through STEM/EDS. As a result of hydration, it was clear that a chemical breakdown of the initial air-formed oxide film occurred on AZ alloys. Mismatch in the lattice parameters of Mg (hexagonal), MgO (cubic) and $Mg(OH)_2$ (hexagonal), along with the sizeable volume expansion produced by hydration of MgO, was the most probable cause of chemical breakdown initiation within the inner barrier layer. The severity of the chemical breakdown was a function of the pH of the environment and this seemed to be best related to the rate at which hydration of MgO occurred.

Although the inner barrier layer underwent breakdown primarily due to hydration, the film was electrochemically stable even after significant hydration had transpired. No breakdown potentials were observed even at large anodic overpotentials on any of the samples analyzed and i_{corr} values were very low. However, the introduction of Cl^- ions into the electrolyte caused electrochemical breakdown of the $MgO/Mg(OH)_2$ surface film at low anodic overpotentials in the near-neutral environment. The specific mechanism for breakdown is likely related to incorporation of Cl^- ions into the corrosion film where soluble complexes are formed at weak points in the film. Consequently, if the concentration of Cl^- ions is increased, the breakdown will occur at lower anodic overpotentials and possibly even at E_{corr} itself, as was observed on the Mg-Al binary samples in this study. Breakdown due to microgalvanic coupling of the matrix phase

with microstructural features, such as the β phase or AlMn intermetallic particles was not consistent with the observations of this work. No breakdown potential was observed on the samples exposed to the alkaline environment due to the increased stability of the inner barrier layer.

The disparity in the stability of the inner barrier layer between the near-neutral and alkaline environments lead to drastic differences in the kinetics of the inherent corrosion processes on AZ alloys. Both the cathodic and anodic reaction rates were reduced in the alkaline environment. Values of $i_{o,c}$ for the hydrogen evolution reaction were an order of magnitude lower, and anodic limiting current densities were observed on all samples exposed to the alkaline solution. Alloyed Al concentration noticeably affected both the anodic and cathodic kinetics in the alkaline environment, whereas only the cathodic kinetics were significantly affected in the near-neutral environment.

In both environments, alloyed Al concentration from 0 - 3 wt % slowed the rate of hydrogen evolution by orders of magnitude with respect to 4N Mg. The magnitudes of exchange current densities for hydrogen evolution were exceedingly low, and as a result, the reaction likely did not occur on the surface of the metal, but on the surface film itself. Specifically, the mechanism for the reduction in hydrogen evolution appeared to be related to enrichment of Al into the surface film, altering the electrocatalytic properties of the film. Further alloying of Al from 3 – 8 wt % did not affect the cathodic kinetics additionally in either environment. The anodic kinetics were only slightly affected by alloying Al from 0 – 3 wt % in the near-neutral environment. Hydration of MgO appeared to play the dominant role in determining the corrosion resistance of AZ alloys in

this environment and thus, the effect of Al alloying was only minor. However, when hydration rates were low in the alkaline environment, significant effects due to alloyed Al were observed. Increasing the concentration of Al from 3 – 8 wt % resulted in a decrease in the i_L by two orders of magnitude. A much more protective inner barrier layer was formed and diffusion of metal cations through this layer was likely increasingly more difficult.

Overall, the corrosion rate of AZ alloys was low in both environments. Furthermore, increasing alloyed Al concentration from 3 – 8 wt % did not appear to affect i_{corr}. Improvements to the cathodic kinetics were observed by alloying Al from 0 – 3 wt %. The anodic kinetics appeared to be predominantly controlled by hydration in the near-neutral environment and by enrichment of Al into the passive film in the alkaline environment. Since hydration broke down the protective barrier layer relatively easily, minimal resistance to anodic polarization was witnessed at near-neutral pH and both AZ alloys performed similarly. In contrast, the resistance to anodic dissolution in alkaline pH of AZ80 was far superior to AZ31. Therefore, AZ alloys with higher alloyed Al concentration provided greater resistance to anodic polarization in mildly aggressive environments.

6.1 Next Steps and Future Research Opportunities

Throughout this study, major improvements to the current knowledge of the natural corrosion processes occurring on AZ alloys were established. However, it became apparent that further research was necessary to solidify the findings of this study and

further investigate methods to improve the corrosion resistance of AZ alloys in mildly aggressive solutions.

First, the most important future research topic to be explored is the specific mechanism of hydration of the Al-enriched MgO air-formed inner barrier layer on AZ alloys. Hydration, leading to the subsequent breakdown of the inner barrier layer, appeared to dominate the corrosion behaviour in neutral environments. Furthermore, although the severity was dramatically reduced in alkaline environments, hydration and breakdown still occurred. The breakdown compromised the ability of the surface film to protect against aggressive Cl^- ions, even in mildly aggressive solutions. A comprehensive study investigating ways to slow hydration of MgO through surface modification may lead to substantial improvements in the corrosion resistance of AZ alloys.

An appealing research topic focused on AZ alloy corrosion deals with the apparent active-passive transition behaviour of E_{corr} in alkaline environments. Both AZ31 and AZ80 exhibited irregular oscillating potential behaviour in pure water at pH 14 whereas E_{corr} was essentially constant in the same solution at pH $\approx$ 7. Interestingly, superior corrosion performance was observed on AZ alloys, which exhibited this erratic active-passive behaviour. Therefore, these fluctuations in potential apparently were beneficial to the corrosion resistance of the AZ alloy despite the instability. Thus, it would be advantageous to the scientific community to examine the specific mechanism(s) responsible for the active-passive behaviour.

Another topic requiring further research is the apparent saturation of the reduction in hydrogen evolution as alloyed Al concentration reaches 3 wt %. Electrocatalytic

alteration of the surface film seemed the most likely explanation for the lower rate of hydrogen evolution. However, if incorporation of Al into the corrosion film slowed the rate of the cathodic reaction, it would be expected that increasing the amount of Al enrichment would further reduce the cathodic kinetics. Oddly enough, this property was not observed, as alloying Al from 3 – 8 wt % did not affect the cathodic hydrogen evolution rate at all. A study focused on the rationale for this apparent saturation is required to ensure the cathodic reaction in fact occurs on the surface film itself and is independent of microstructural features.

The resistance to corrosion in alkaline solutions appeared to increase as alloyed Al content increased, as a result of further stabilization of the inner barrier layer. However, thermodynamically Al is unstable and forms a soluble anion in alkaline environments, suggesting increased Al enrichment into the surface film would be deleterious to the corrosion resistance of the AZ alloy. The rate at which this reaction occurs may be relatively slow and therefore, not harmful to the corrosion resistance on AZ alloys, but this property requires further research.

7 References

[1] United States Automotive Materials Partnership (USAMP), Automotive Metals Division (AMD), "Magnesium vison 2020: A north american automotive vision for magnesium." 2004.

[2] J. Wang, D. Li, X. Yu, X. Jing, M. Zhang and Z. Jiang. "Hydrotalcite conversion coating on mg alloy and its corrosion resistance." *J. Alloys Compounds 494(1-2),* pp. 271-274. 2010.

[3] M. Zhao, P. Schmutz, S. Brunner, M. Liu, G. Song and A. Atrens. "An exploratory study of the corrosion of Mg alloys during interrupted salt spray testing." *Corros. Sci. 51(6),* pp. 1277-1292. 2009.

[4] O. Lunder, K. Nisancioglu and R. S. Hansen, "Corrosion of die cast magnesium-aluminum alloys." pp. 117-126. 1993.

[5] J. H. Nordlien, K. Nisancioglu, S. Ono and N. Masuko. "Morphology and structure of Water‐Formed oxides on ternary MgAl alloys." *J. Electrochem. Soc. 144,* pp. 461-466. 1997.

[6] S. Feliu Jr, M. C. Merino, R. Arrabal, A. E. Coy and E. Matykina. "XPS study of the effect of aluminium on the atmospheric corrosion of the AZ31 magnesium alloy." *Surf Interface Anal 41(3),* pp. 143-150. 2009.

[7] W. A. Badawy, N. H. Hilal, M. El-Rabiee and H. Nady. "Electrochemical behavior of mg and some Mg alloys in aqueous solutions of different pH." *Electrochim. Acta 55(6),* pp. 1880-1887. 2010.

[8] S. J. Splinter and N. S. McIntyre. "The initial interaction of water vapour with Mg Al alloy surfaces at room temperature." *Surf. Sci. 314(2),* pp. 157-171. 1994.

[9] J. H. Nordlien, K. Nisancioglu, S. Ono and N. Masuko. "Morphology and structure of oxide films formed on MgAl alloys by exposure to air and water." *J. Electrochem. Soc. 14*3, pp. 2564-2572. 1996.

[10] A. Pardo, M. C. Merino, A. E. Coy, F. Viejo, R. Arrabal and S. Feliú Jr. "Influence of microstructure and composition on the corrosion behaviour of Mg/Al alloys in chloride media." *Electrochim. Acta 53(27),* pp. 7890-7902. 2008.

[11] W. Zheng, Li,Shuang-shou,Tang,B. and D. Zeng, "Microstructure and properties of Mg-Al binary alloys." *China Foundry,* pp. 270-274, 2006.

[12] M. D. Bharadwaj, S. M. Tiwari, Y. Wang and V. Mani, "Microgalvanic corrosion behavior of Mg alloys as a function of aluminum content." pp. 389-391. 1993.

[13] O. Lunder, Lein J. E., Aune T. Kr. and K. Nisancioglu, "The Role of $Mg_{17}Al_{12}$ Phase in the Corrosion of Mg Alloy AZ91." *Corrosion,* vol. 45, pp. 741-748, 1989.

[14] S. Mathieu, C. Rapin, J. Steinmetz and P. Steinmetz. "A corrosion study of the main constituent phases of AZ91 magnesium alloys." *Corros. Sci. 45(12),* pp. 2741-2755. 2003.

[15] G. Song, A. Atrens and M. Dargusch. "Influence of microstructure on the corrosion of diecast AZ91D." *Corros. Sci. 41(2),* pp. 249-273. 1998.

[16] H. J. Martin, M. F. Horstemeyer and P. T. Wang. "Structure–property quantification of corrosion pitting under immersion and salt-spray environments on an extruded AZ61 magnesium alloy." *Corros. Sci. 53(4),* pp. 1348-1361. 2011.

[17] M. Zhao, M. Liu, G. Song and A. Atrens. "Influence of the β-phase morphology on the corrosion of the Mg alloy AZ91." *Corros. Sci. 50(7),* pp. 1939-1953. 2008.

[18] A. Pardo, M. C. Merino, A. E. Coy, R. Arrabal, F. Viejo and E. Matykina. "Corrosion behaviour of magnesium/aluminium alloys in 3.5wt.% NaCl." *Corros. Sci. 50(3),* pp. 823-834. 2008.

[19] G. Song, A. Atrens, X. Wu and B. Zhang. "Corrosion behaviour of AZ21, AZ501 and AZ91 in sodium chloride." *Corros. Sci. 40(10),* pp. 1769-1791. 1998.

[20] L. Wang, T. Shinohara and B. Zhang, "Corrosion Behavior of AZ31 Magnesium Alloy in Dilute Sodium Chloride Solutions." *Corrosion Engineering,* vol. 58, pp. 127-137. 2009.

[21] L. Wang, B. Zhang and T. Shinohara. "Corrosion behavior of AZ91 magnesium alloy in dilute NaCl solutions." *Mater Des 31(2),* pp. 857-863. 2010.

[22] C. B. Baliga and P. Tsakiropoulos. "Development of corrosion resistant magnesium alloys part 2 structure of corrosion products on rapidly solidified Mg–16Al alloys." *Mats. Sci. Tech. 9(6),* pp. 513-519. 1993.

[23] G. Ballerini, U. Bardi, R. Bignucolo and G. Ceraolo. "About some corrosion mechanisms of AZ91D magnesium alloy." *Corros. Sci. 47(9),* pp. 2173-2184. 2005.

[24] C. Blawert, W. Dietzel, E. Ghali and G. Song. "Anodizing treatments for magnesium alloys and their effect on corrosion resistance in various environments." *Adv. Eng. Mater. 8(6),* pp. 511-533. 2006.

[25] Y. CHENG, T. QIN, H. WANG and Z. ZHANG. "Comparison of corrosion behaviors of AZ31, AZ91, AM60 and ZK60 magnesium alloys." *Transactions of Nonferrous Metals Society of China 19(3),* pp. 517-524. 2009.

[26] S. Feliu Jr., A. Pardo, M. C. Merino, A. E. Coy, F. Viejo and R. Arrabal. "Correlation between the surface chemistry and the atmospheric corrosion of AZ31, AZ80 and AZ91D magnesium alloys." *Appl. Surf. Sci. 255(7),* pp. 4102-4108. 2009.

[27] S. Feliu Jr., C. Maffiotte, J. C. Galván and V. Barranco. "Atmospheric corrosion of magnesium alloys AZ31 and AZ61 under continuous condensation conditions." *Corros. Sci. 53(5),* pp. 1865-1872. 2011.

[28] S. Feliu Jr., C. Maffiotte, A. Samaniego, J. C. Galván and V. Barranco. "Effect of the chemistry and structure of the native oxide surface film on the corrosion properties of commercial AZ31 and AZ61 alloys." *Appl. Surf. Sci. 257(20),* pp. 8558-8568. 2011.

[29] S. Feliu Jr., C. Maffiotte, A. Samaniego, J. C. Galván and V. Barranco. "Effect of naturally formed oxide films and other variables in the early stages of Mg-alloy corrosion in NaCl solution." *Electrochim. Acta 56(12),* pp. 4554-4565. 2011.

[30] E. Ghali, W. Dietzel and K. U. KAINER. "General and localized corrosion of magnesium alloys: A critical review." *Journal of Materials Engineering and Performance 13(1),* pp. 7-23. 2004.

[31] K. M. Ismail and S. Virtanen. "Electrochemical behavior of magnesium alloy AZ31 in 0.5 M KOH solution." *Electrochemical and Solid-State Letters 1*0, pp. C9-C11. 2007.

[32] L. J. Liu and M. Schlesinger. "Corrosion of magnesium and its alloys." *Corros. Sci. 51(8),* pp. 1733-1737. 2009.

[33] M. Liu, S. Zanna, H. Ardelean, I. Frateur, P. Schmutz, G. Song, A. Atrens and P. Marcus. "A first quantitative XPS study of the surface films formed, by exposure to water, on mg and on the Mg–Al intermetallics: Al3Mg2 and Mg17Al12." *Corros. Sci. 51(5),* pp. 1115-1127. 2009.

[34] O. Lunder, Lein J. E., Hesjevik S. M., Aune T. Kr. and Nisancioglu K. "Corrosion morphologies on magnesium alloy AZ91." *Materials and Corrosion 45(6),* pp. 331-340. 1994.

[35] G. L. Makar and J. Kruger. "Corrosion studies of rapidly solidified magnesium alloys." *J. Electrochem. Soc. 13*7, pp. 414. 1990.

[36] G. L. Makar and J. Kruger. "Corrosion of magnesium." *Int. Mat. Rev. 38(3),* pp. 138-153. 1993.

[37] J. H. Nordlien, S. Ono, N. Masuko and K. Nisancioglu. "A TEM investigation of naturally formed oxide films on pure magnesium." *Corros. Sci. 39(8),* pp. 1397-1414. 1997.

[38] Q. Qu, J. Ma, L. Wang, L. Li, W. Bai and Z. Ding. "Corrosion behaviour of AZ31B magnesium alloy in NaCl solutions saturated with CO2." *Corros. Sci. 53(4),* pp. 1186-1193. 2011.

[39] M. Santamaria, F. Di Quarto, S. Zanna and P. Marcus. "Initial surface film on magnesium metal: A characterization by X-ray photoelectron spectroscopy (XPS) and photocurrent spectroscopy (PCS)." *Electrochim. Acta 53(3),* pp. 1314-1324. 2007.

[40] G. Song, A. Atrens, D. S. John, X. Wu and J. Nairn. "The anodic dissolution of magnesium in chloride and sulphate solutions." *Corros. Sci. 39(10-11),* pp. 1981-2004. 1997.

[41] G. Song, A. Atrens, D. Stjohn, J. Nairn and Y. Li. "The electrochemical corrosion of pure magnesium in 1 N NaCl." *Corros. Sci. 39(5),* pp. 855-875. 1997.

[42] G. Song, A. L. Bowles and D. H. StJohn. "Corrosion resistance of aged die cast magnesium alloy AZ91D." *Materials Science and Engineering: A 366(1),* pp. 74-86. 2004.

[43] L. Wang, T. Shinohara and B. Zhang. "Influence of chloride, sulfate and bicarbonate anions on the corrosion behavior of AZ31 magnesium alloy." *J. Alloys Compounds 496(1-2),* pp. 500-507. 2010.

[44] L. Wang, T. Shinohara and B. Zhang. "XPS study of the surface chemistry on AZ31 and AZ91 magnesium alloys in dilute NaCl solution." *Appl. Surf. Sci. 256(20),* pp. 5807-5812. 2010.

[45] L. Wang, T. Shinohara, B. Zhang and H. Iwai. "Characterization of surface products on AZ31 magnesium alloy in dilute NaCl solution." *J. Alloys Compounds 485(1-2),* pp. 747-752. 2009.

[46] R. ZENG, J. ZHANG, W. HUANG, W. DIETZEL, K. U. KAINER, C. BLAWERT and W. KE. "Review of studies on corrosion of magnesium alloys." *Transactions of Nonferrous Metals Society of China 16(Supplement 2),* pp. s763-s771. 2006.

[47] E. Aghion, B. Bronfin and D. Eliezer. “The role of the magnesium industry in protecting the environment.” *J. Mater. Process. Technol. 117(3),* pp. 381-385. 2001.

[48] S. H. Zhang, Q. L. Jin, Z. T. Wang, D. -. Li and W. L. Zhou. “Development of plasticity processing of magnesium alloys.” *Mater. Sci. Forum 426,* pp. 545-550. 2003.

[49] X. Huang, K. Suzuki and N. Saito. “Microstructure and mechanical properties of AZ80 magnesium alloy sheet processed by differential speed rolling.” *Materials Science & Engineering A 508(1-2),* pp. 226-233. 2009.

[50] D. Letzig, J. Swiostek, J. Bohlen and K. U. KAINER, "Magnesium wrought alloy properties of the AZ – series." *TMS*, pp. 55-60. 2005.

[51] M. C. Merino, A. Pardo, R. Arrabal, S. Merino, P. Casajús and M. Mohedano. “Influence of chloride ion concentration and temperature on the corrosion of Mg–Al alloys in salt fog.” *Corros. Sci. 52(5),* pp. 1696-1704. 2010.

[52] ASM International, ASM Handbook Volume 09: “Metallography and Microstructures.” pp. 428-430. 1985.

[53] Z. LI, Y. YANG and Z. ZHANG. “Transformation mechanism of lamellar microstructure of AZ80 wrought Mg alloy during warm deformation.” *Transactions of Nonferrous Metals Society of China 18(Supplement 1),* pp. s156-s159. 2008.

[54] D. Eliezer, E. Aghion and F. H. Froes. “Magnesium science, technology and applications.” *Advanced Performance Materials 5(3),* pp. 201-212. 1998.

[55] R. Lindström, J. Svensson and L. Johansson. “The influence of carbon dioxide on the atmospheric corrosion of some magnesium alloys in the presence of NaCl.” *J. Electrochem. Soc. 149,* pp. B103-B107. 2002.

[56] G. Song and A. Atrens. “Understanding magnesium Corrosion—A framework for improved alloy performance.” *Adv. Eng. Mater. 5(12),* pp. 837-858. 2003.

[57] D. Eliezer, P. Uzan and E. Aghion. “Effect of second phases on the corrosion behavior of magnesium alloys.” *Mater. Sci. Forum 419,* pp. 857-866. 2003.

[58] T. Beldjoudi, C. Fiaud and L. Robbiola, "Influence of Homogenization and Artificial Aging Heat Treatments on Corrosion Behavior of Mg-Al Alloys." *Corrosion,* vol. 49, pp. 738-745, 1993.

[59] J. D. Hanawalt, C. E. Nelson and J. A. Peloubet, "Corrosion Studies of Magnesium and its Alloys." *Trans. AIME,* vol. 147, pp. 273. 1942.

[60] K. N. Reichek, K. J. Clark and J. E. Hillis, "Controlling the Salt Water Corrosion Performance of Magnesium AZ91 Alloy." *SAE International,* 1985.

[61] ASM International, ASM Handbook Volume 02: "Properties and Selection: Nonferrous Alloys and Special-Purpose Materials." pp. 480-482. 1990.

[62] H. B. Yao, Y. Li and A. T. S. Wee. "An XPS investigation of the oxidation/corrosion of melt-spun Mg." *Appl. Surf. Sci. 158(1-2),* pp. 112-119. 2000.

[63] V. Fournier, P. Marcus and I. Olefjord. "Oxidation of magnesium." *Surf Interface Anal 34(1),* pp. 494-497. 2002.

[64] O. Fruhwirth, G. W. Herzog, I. Hollerer and A. Rachetti. "Dissolution and hydration kinetics of MgO." *Surface Technology 24(3),* pp. 301-317. 1985.

[65] D. A. Vermilyea. "The dissolution of MgO and $Mg(OH)_2$ in aqueous solutions." *J. Electrochem. Soc. 116,* pp. 1179-1183. 1969.

[66] J. A. Mejias, A. J. Berry, K. Refson and D. G. Fraser. "The kinetics and mechanism of MgO dissolution." *Chemical Physics Letters 314(5-6),* pp. 558-563. 1999.

[67] G. Williams and H. N. McMurray. "Localized corrosion of magnesium in chloride-containing electrolyte studied by a scanning vibrating electrode technique." *J. Electrochem. Soc. 155,* pp. C340-C349. 2008.

[68] Magnesium.com, "Magnesium Pourbaix Diagram." 2011.

[69] Corrosion Doctors, "Aluminum E-pH (Pourbaix) Diagram." 2011.

[70] D. L. Hawke, J. E. Hillis, M. Pekguleryuz and I. Nakatsugawa, "Corrosion Behavior in Magnesium and Magnesium Alloys." *ASM International,* pp. 194-210, 1999.

[71] R. Ambat, N. N. Aung and W. Zhou. "Evaluation of microstructural effects on corrosion behaviour of AZ91D magnesium alloy." *Corros. Sci. 42(8),* pp. 1433-1455. 2000.

[72] X. Hallopeau, T. Beldjoudi, C. Fiaud and L. Robbiola, "Corrosion Resistance and Electrochemical Behaviour of Mg and AZ91 Alloy in Aqueous Electrolyte Solutions Containing XOyn- Inhibiting Ions." *Corrosion Reviews,* vol. 16, pp. 27-42, 1998.

[73] A. Jager, P. Lukac, V. Gartnerova, J. Haloda and M. Dopita. "Influence of annealing on the microstructure of commercial Mg alloy AZ31 after mechanical forming." *Materials Science & Engineering A 432(1-2),* pp. 20-25. 2006.

[74] S. Kamado, T. Ashie, H. Yamada, K. Sanbun and Y. Kojima. “Improvement of tensile properties of wrought magnesium alloys by grain refining.” *Mater. Sci. Forum 350,* pp. 65-72. 2000.

[75] ASM International, ASM Handbook Volume 09: “Metallography and Microstructures.” pp. 426. 1985.

[76] A. Seyeux, M. Liu, P. Schmutz, G. Song, A. Atrens and P. Marcus. “ToF-SIMS depth profile of the surface film on pure magnesium formed by immersion in pure water and the identification of magnesium hydride.” *Corros. Sci. 51(9),* pp. 1883-1886. 2009.

[77] L. F. Amaral, I. R. Oliveira, R. Salomão, E. Frollini and V. C. Pandolfelli. “Temperature and common-ion effect on magnesium oxide (MgO) hydration.” *Ceram. Int. 36(3),* pp. 1047-1054. 2010.

[78] R. M. Hazen, "Effects of temperature and pressure on the cell dimesion and X-ray temperature factors of periclase." *American Minerologist,* vol. 61, pp. 266-271. 1976.

[79] J. B. Parise, K. Leinenweber, D. J. Weidner, K. Tan and R. B. Von Dreele, "Pressure-induced H bonding: Neutron diffraction study of brucite, $Mg(OD)_2$, to 9.3 GPa." *American Minerologist,* vol. 79, pp. 193-196. 1994.

[80] M. E. Straumanis, "The precision determination of lattice constants by the powder and rotation crystal methods and applications." *Journal of Applied Physics,* vol. 20, pp. 726-734. 1949.

[81] H. Kita, "Periodic Variation of Exhange Current Density of Hydrogen Electrode Reaction with Atomic Number and Reaction Mechanism." *J. Electrochem. Soc.,* vol. 113, pp. 1095-1111. 1966.